



eCOMMONS

Loyola University Chicago
Loyola eCommons

Dissertations

Theses and Dissertations

2023

Dynamic Control of the Cardiac Calcium Pump

Sean Robert Cleary

Follow this and additional works at: https://ecommons.luc.edu/luc_diss

 Part of the [Molecular Biology Commons](#)

Recommended Citation

Cleary, Sean Robert, "Dynamic Control of the Cardiac Calcium Pump" (2023). *Dissertations*. 4011.
https://ecommons.luc.edu/luc_diss/4011

This Dissertation is brought to you for free and open access by the Theses and Dissertations at Loyola eCommons. It has been accepted for inclusion in Dissertations by an authorized administrator of Loyola eCommons. For more information, please contact ecommons@luc.edu.



This work is licensed under a [Creative Commons Attribution-Noncommercial-No Derivative Works 3.0 License](#).
Copyright © 2023 Sean Robert Cleary

LOYOLA UNIVERSITY CHICAGO

DYNAMIC CONTROL OF THE CARDIAC CALCIUM PUMP

A DISSERTATION SUBMITTED TO

THE FACULTY OF THE GRADUATE SCHOOL

IN CANDIDACY FOR THE DEGREE OF

DOCTOR OF PHILOSOPHY

PROGRAM IN CELL AND MOLECULAR PHYSIOLOGY

BY

SEAN R. CLEARY

CHICAGO, ILLINOIS

AUGUST 2023

Copyright by Sean R. Cleary, 2023
All rights reserved.

ACKNOWLEDGEMENTS

I would like to begin by thanking my mentor, Dr. Seth Robia. I joined the Robia lab with no background in cardiac physiology and barely any microscopy experience. After nearly 5 years in his lab, I've not only learned to use a wide range of techniques in fluorescent microscopy, spectroscopy, and biochemistry, but also have developed my own research questions in the fields of cardiac and molecular biology and answered them using the tools available to me in lab. Seth's mentorship has allowed me to develop these skills in a supportive environment where I was directed towards projects with a high likelihood of success and was also allowed to develop and pursue my own ideas. Seth has helped me accomplish all of the goals I set out to achieve in my PhD and much more. I'm also very grateful for the mentorship of my dissertation committee members, Drs Jonathan Kirk, Aleksey Zima, Peter Kekenes-Huskey, and L. Michel Espinoza-Fonseca for their helpful insights in understanding my project and encouragement to pursue rigorous and challenging experiments. I also want to acknowledge the rest of the faculty of the Physiology department, who have provided a community where expert advice, support, and resources were always readily shared with me. It is because of all of these mentors that I feel confident as I transition towards a career as an independent scientist.

Next, I need to thank my lab mates and collaborators in the Robia lab and department who have been a constant source of technical and emotional support. Especially, I would like to thank Jaroslava Seflova, who taught me so much about

membrane proteins, fluorescence spectroscopy, and has been the reason so many of my experiments worked. I'd also like to thank Ellen Cho and Marsha Pribadi, who introduced me to making FRET measurements and were instrumental in getting my project started when I joined the lab. I'm also grateful to Xuan Fang and Audrey Kongmeneck, who have been critical mentors to me in learning the skills of coding, understanding molecular kinetics, mathematical modeling, and analyzing molecular dynamics simulations. I'd also like to give special thanks to John Yap, Taylor Phillips, Patryk Karkut, Elisa Bovo, and Daniel Kahn for their support over the past 5 years.

I'd also like to thank my friends and family for supporting me through this process. I'd especially like to thank my partner Abbie Randall for her ceaseless love, support, and guidance that have been invaluable for me during my graduate studies. I'd also like to acknowledge Margaret Catwood for her constant love and support during my graduate studies. I'm also grateful to my parents for getting me this far, and to my brother, Scott Cleary, for his support and solidarity through this process. Special thanks to friends Jeffrey Weiss and Tyler Jankowski for being a consistent source of community for me through my developing science career.

This investigation was supported by the National Institutes of Health (NIH): Ruth L. Kirschstein Predoctoral Individual National Research Service Award (NRSA) F31HL165900-01 from the National Heart, Lung, and Blood Institute (NHLBI) to S.R.C. Maximizing Investigators' Research Awards (MIRA) R35GM124977 from the National Institute of General Medical Sciences (NIGMS) to P. M. K.-H.; MIRA R35GM138183 from NIGMS and K22HL133150 from NHLBI to J. R. B.; R01HL092321 and R01HL143816 from the NHLBI to S. L. R.

For my mother, Diane, who made sure I went to college and made all this possible.

TABLE OF CONTENTS

ACKNOWLEDGEMENTS	iii
LIST OF FIGURES.....	ix
LIST OF TABLES.....	xi
LIST OF ABBREVIATIONS.....	xii
ABSTRACT	xiv
CHAPTER ONE: INTRODUCTION	1
Discovery of SERCA	1
The Role of SERCA in EC Coupling.....	1
SERCA as a Potential Therapeutic Target	3
CHAPTER TWO: REVIEW OF RELATED LITERATURE	5
Molecular Characterization of SERCA	5
SERCA Regulation in Health and Disease.....	9
Phospholamban (PLB)	10
Dwarf open reading frame (DWORF)	13
CHAPTER THREE: MATERIALS AND METHODS	16
Molecular Biology and Cell Culture	16
Human Heart Tissue Procurement	17
Human Tissue Membrane Protein Enrichment.....	17
HEK Cell Microsomal Membrane Preparation	17
Western Blotting and Protein Thermostability Assays	18
FRET Acceptor Sensitization	20
Cell Permeabilization and Manipulated Cytoplasmic Conditions.....	23
Confocal Fluorescence Microscopy to Measure Intermolecular FRET and HEK-293 Cytoplasmic Ca ²⁺	25
Kinetic Modeling and Model Data Availability	26
Time Correlated Single Photon Counting (TCSPC).....	28
Fluorescence Correlation Spectroscopy (FCS)	29
Molecular Dynamics Simulations.....	32
Statistical Analysis.....	32
CHAPTER FOUR: INHIBITORY AND STIMULATORY MICROPEPTIDES PREFERENTIALLY BIND TO DIFFERENT CONFORMATIONS OF THE CARDIAC CALCIUM PUMP	33
Results	33
SERCA Affinity for PLB and DWORF is Dependent on Ca ²⁺ Pump Conformation	33
Ca ²⁺ -Dependent SERCA-Micropeptide Exchange Kinetics.....	39

Modeling the Redistribution of PLB and DWORF Regulatory Complexes.....	43
Dynamic Responses of SERCA-Micropeptide Binding Equilibria to Ca ²⁺ Transients	45
Discussion.....	47
Differential Ca ²⁺ -Dependence of Micropeptide Affinity for SERCA.....	47
Functional Implications of Micropeptide Exchange During the Cardiac Cycle.....	49
Function of the PLB Pentamer Kinetic Trap in Rest and Exercise	50
Summary and Future Directions.....	51
CHAPTER FIVE: A DILATED CARDIOMYOPATHY MUTATION IN PHOSPHOLAMBAN, ARGININE 14 DELETION, INCREASES PHOSPHOLAMBAN PENTAMER STABILITY	52
Introduction	52
Results	54
R14del-PLB Forms More Stable Pentamers than WT-PLB.....	54
R14del-PLB Exchanges Slowly from PLB Pentamers.....	58
Slow Exchange of PLB monomers from R14del PLB Pentamers Disrupts Ca ²⁺ Regulatory Dynamics	62
Discussion.....	64
R14de Mutation Stabilizes PLB Pentamers.....	64
R14del PLB Pentamers Exchange Slowly and Are Less Responsive to Changing Physiological Demands	66
Impaired PLB Binding Dynamics May Contribute to Arrhythmogenesis	67
Summary.....	68
CHAPTER SIX: PHOSPHOLAMBAN INHIBITS THE CARDIAC CALCIUM PUMP THROUGH REVERSING THE ALLOSTERIC ENHANCEMENT OF CALCIUM AFFINITY BY ATP.....	70
Introduction	70
Results	72
PLB Reverses Nucleotide Activation of SERCA Ca ²⁺ Affinity by ATP	72
MD Simulations of SERCA with ATP and PLB.....	75
Discussion.....	78
CHAPTER SEVEN: FUTURE DIRECTIONS & CLINICAL INSIGHTS	82
Overview of SERCA-Targeted Therapies for Heart Failure.....	82
SERCA2a Gene Delivery	83
Direct Activation of SERCA	83
Relief of PLB Inhibition of SERCA.....	85
Limitations of SERCA Activation	87
Potential Preventative Approaches for PLB-associated Cardiomyopathy	88
Final Thoughts.....	89
APPENDIX A: INTRODUCTION TO THE APPENDICES	90
APPENDIX B: SUPPLEMENTARY INFORMATION FOR CHAPTER FOUR	92

APPENDIX C: PLB AND DWORF COMPETE TO BIND A COMMON REGULATORY SITE ON SERCA.....	113
APPENDIX D: SUPPLEMENTARY INFORMATION FOR CHAPTER FIVE	117
APPENDIX E: SUPPLEMENTARY INFORMATION FOR CHAPTER SIX.....	123
APPENDIX F: DIMERIZATION OF SERCA2A.....	132
APPENDIX G: ADDITIONAL DATA	137
REFERENCE LIST.....	142
VITA	156

LIST OF FIGURES

Figure 1. Excitation-Contraction Coupling in Cardiomyocytes.....	2
Figure 2. Molecular Characterization of SERCA	6
Figure 3. A Computational Model Simulates SERCA Cycle Kinetics	8
Figure 4. Phospholamban (PLB) Regulation of the Ca ²⁺ ATPase (SERCA)	11
Figure 5. DWORF Competes with PLB for Regulation of SERCA.....	14
Figure 6. Photobleaching-corrected FRET Efficiency Measures Membrane Protein-Protein Interactions in Live Cells	22
Figure 7. FCS and FCCS Measurements.....	31
Figure 8. Inhibitory and Stimulatory Micropeptides Preferentially Bind Different SERCA Conformations.....	34
Figure 9. SERCA-Micropeptide Interactions are Ca ²⁺ Sensitive.....	37
Figure 10. Dynamic Exchange of PLB and DWORF from SERCA during Intracellular Ca ²⁺ Elevations	38
Figure 11. Kinetics of SERCA-Micropeptide Binding Processes during Ca ²⁺ Release.	40
Figure 12. Kinetics of SERCA-Micropeptide Binding Processes during Ca ²⁺ Uptake... ..	42
Figure 13. A Computational Model Simulates the Dynamics of PLB and DWORF Interactions with SERCA.....	44
Figure 14. R14del Mutation Increases Oligomerization and Thermostability of PLB Pentamers.....	55
Figure 15. R14del-PLB Mutation Stabilizes PLB Pentamers within Live Cell Membranes	57
Figure 16. R14del-PLB Exchanges Slowly from Pentamers compared to WT-PLB	61
Figure 17. A Computational Model Simulates PLB-SERCA Complex Exchange during Changes in Heart Rate for WT and R14del PLB	63

Figure 18. Effects of Phosphorylation and DCM Mutations on PLB Regulatory Interactions.....	69
Figure 19. PLB Reduces the Ca ²⁺ Affinity of SERCA by Reversing Nucleotide Activation	73
Figure 20. Effects of ATP and PLB on Structure of SERCA Ca ²⁺ Transport Sites	76
Figure 21. A Schematic Diagram of the Allosteric Relationships between ATP, PLB, and Ca ²⁺ Binding to SERCA	80

LIST OF TABLES

Table 1. Acceptor-Sensitization FRET Curve Parameters 36

LIST OF ABBREVIATIONS

2CS	Two-color SERCA
AMPPCP	Adenosine-5'- β , γ -methylene-triphosphate
ANOVA	Analysis of variance
ARVC	Arrhythmogenic right ventricular cardiomyopathy
AU	Arbitrary units
BCA	Bicinchoninic acid protein assay
CaM	Calcium-calmodulin
CaMKII	CaM-dependent protein kinase II
DCM	Dilated cardiomyopathy
DWORF	Dwarf open reading frame
EC coupling	Excitation-contraction coupling
ER	Endoplasmic reticulum
FCS	Fluorescence correlation spectroscopy
FCCS	Fluorescence cross-correlation spectroscopy
FRET	Fluorescence/Förster resonance energy transfer
GFP	Green fluorescent protein
HH	Human heart
HF	Heart failure
K _D	Apparent dissociation constant
LTCC	L-type Ca ²⁺ channel

MD	Molecular dynamics
PIE	Pulsed interleaved excitation
PKA	Protein kinase A
PLB	Phospholamban
POPC	1-palmitoyl-2-oleoyl-glycero-3-phosphocholine
RyR	Ryanodine receptor
SE	Standard error
SR	Sarcoplasmic reticulum
SERCA	SR/ER Ca ²⁺ ATPase
TAC	Transaortic Constriction
TG	Thapsigargin
TM	Transmembrane
T-tubules	Transverse tubules
TCSPC	Time-correlated single photon counting
TF	Transfected
UTF	Untransfected
WT	Wildtype

ABSTRACT

The sarco/endoplasmic reticulum Ca^{2+} -ATPase (SERCA) sequesters Ca^{2+} into the endoplasmic reticulum of cells to establish a reservoir for Ca^{2+} signaling. In the heart, the activity of this transporter is tightly controlled via direct interactions with two competing regulatory micropeptides: phospholamban (PLB) and dwarf open reading frame (DWORF). PLB inhibits SERCA, while DWORF activates SERCA. These competing interactions determine cardiac performance by modulating the Ca^{2+} signals that drive the contraction/relaxation cycle. Previous studies indicated these SERCA-micropeptide interactions are Ca^{2+} -sensitive; SERCA binds PLB more avidly at low cytoplasmic $[\text{Ca}^{2+}]$ but binds DWORF better when $[\text{Ca}^{2+}]$ is high. Here, FRET-microscopy demonstrated that this opposing Ca^{2+} -sensitivity drives dynamic shifts in SERCA-micropeptide binding during cellular Ca^{2+} elevations. Evaluating the rates of these equilibrium shifts revealed that PLB monomers freed from SERCA during Ca^{2+} elevations rapidly oligomerize into PLB pentamers. These stable oligomers unbind slowly, delaying the rebinding of inhibitory PLB monomers to SERCA after Ca^{2+} elevations. In contrast, DWORF is exchanged rapidly on and off SERCA with respect to the rise and fall of transient Ca^{2+} signals. Computational modeling revealed that the slow unbinding of PLB pentamers causes PLB monomers to accumulate in these complexes during accelerated cardiac pacing. We propose that this accumulation of PLB pentamers decreases availability of inhibitory PLB monomers to bind SERCA and contributes to an increase in the contractile force of cardiac muscle at faster heart rates. Moreover, we demonstrated

that a mutation of PLB, Arginine 14 deletion, which is associated with lethal dilated cardiomyopathy, further stabilizes PLB pentamers and blunts these dynamics adjustments to Ca^{2+} handling.

It was also determined that the reciprocal Ca^{2+} sensitivity of PLB and DWORF results from their preference for binding different intermediate conformations that SERCA samples during Ca^{2+} transport. Specifically, PLB had the highest affinity for the ATP-bound state of SERCA, which prevails at low $[\text{Ca}^{2+}]$. This result led us to hypothesize that tight binding of PLB to the ATP-bound state of SERCA may relate to its inhibitory effect on SERCA, decreasing the pump's apparent Ca^{2+} affinity. Using a 2-color SERCA biosensor to report changes in SERCA conformation during Ca^{2+} binding by changes in intramolecular FRET, we tested whether PLB reduces SERCA Ca^{2+} affinity in the presence and absence of nucleotide. The results suggest that PLB inhibits SERCA through reversing an allosteric activation of the pump by ATP.

CHAPTER ONE

INTRODUCTION

Discovery of SERCA

In 1948, Kieley and Meyerhof discovered a Mg^{2+} -activated ATPase enzyme within a membrane fraction of muscle (16). Ebashi and colleagues determined this enzyme to be a Ca^{2+} transporter responsible for relaxing muscle cells by sequestering Ca^{2+} away from the cytoplasm into the luminal compartment of a subcellular organelle, the sarcoplasmic reticulum (SR) of muscle cells (17). This Ca^{2+} transporter is now known as the sarco/endoplasmic reticulum (SR/ER) Ca^{2+} ATPase (SERCA), a member of the P-type ATPase family of cation transporters. Generally, P-type ATPases are housekeeping genes that establish and maintain electrochemical gradients across cell membranes that are used to drive basic cellular functions (18). Isoforms of SERCA are expressed in all mammalian cell types and are responsible for using energy from ATP to establish an intracellular Ca^{2+} store in either the SR or ER lumen to serve as a reservoir for cellular Ca^{2+} signaling (19-21).

The Role of SERCA in EC Coupling

Intracellular Ca^{2+} transport is central to cardiac physiology since Ca^{2+} signals released from the SR drive the contraction and relaxation cycle of the heart. Specifically, intracellular Ca^{2+} elevations couple electrical depolarizations of outer, sarcolemma membranes of muscle cells to contraction at the myofilament driven by actin and myosin, a process termed excitation contraction coupling or *EC coupling* (22,

23) (Fig. 1). When cardiac muscle cells are electrically stimulated, cardiac action potentials propagate a wave of depolarization along the sarcolemma. This depolarization activates L-type Ca^{2+} channels (LTCCs) within transverse tubules (T-tubules) of the sarcolemma, causing them to open and influx a small amount of Ca^{2+} into the cytoplasm. Ca^{2+} entry through LTCCs raises the local concentration of Ca^{2+} in a subcellular microdomain where T-tubules are juxtaposed with the SR membrane (24, 25). This Ca^{2+} triggers opening of ryanodine receptor (RyR) channels, which gate the intracellular Ca^{2+} store within the SR. RyR channel opening releases SR Ca^{2+} , causing cytoplasmic Ca^{2+} concentrations to rise dramatically from low nM to near μM [Ca^{2+}] (22, 26). At these high concentrations of Ca^{2+} , Ca^{2+} is bound by thin filament troponin C and induces a conformation change of the troponin complex that allows interaction of actin and myosin at the myofilament (25, 27). Crossbridge cycling of actin and myosin results in contraction of cardiac muscle at the myofilament (17, 22, 28).

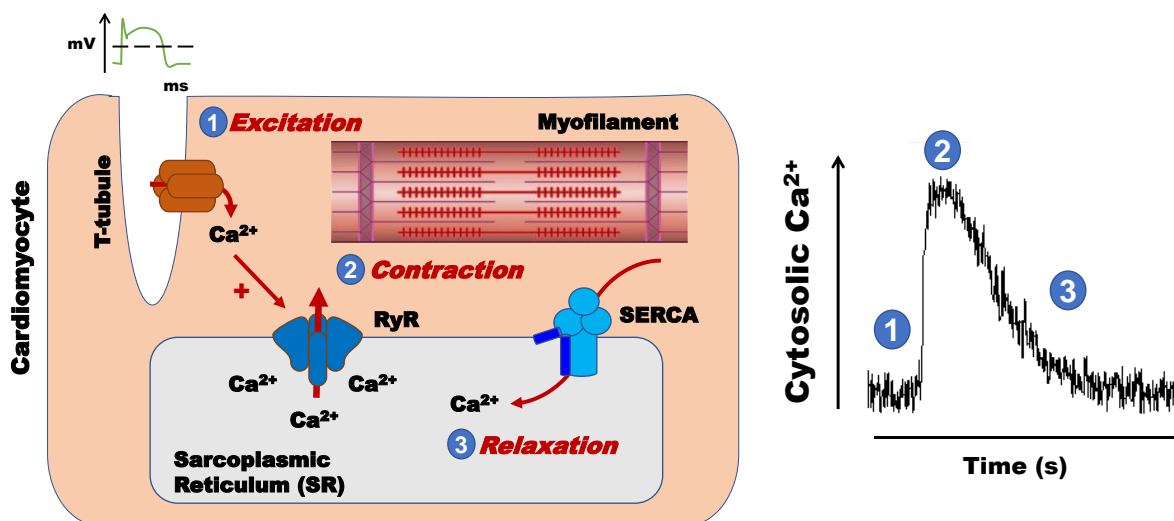


Figure 1. Excitation-Contraction Coupling in Cardiomyocytes. A schematic diagram illustrating how (1) electrical depolarizations of the outer, sarcolemma membrane are coupled to (2) contraction of the myofilament apparatus by intracellular Ca^{2+} signaling. (3) Relaxation of cardiomyocytes is initiated as SERCA transports Ca^{2+} back to SR lumen, lowering Ca^{2+} to basal levels and preparing an intracellular Ca^{2+} store to drive subsequent contractions of the heart.

Ca^{2+} transport by SERCA is the primary driver of the relaxation phase of the cardiac cycle (17). By sequestering Ca^{2+} from the cytoplasm to the SR lumen, SERCA lowers intracellular Ca^{2+} levels until the troponin complex can no longer bind Ca^{2+} , causing a reversal of its Ca^{2+} -dependent conformation change and sarcomere contraction (25, 29). Therefore, the rate at which SERCA re-uptakes Ca^{2+} into the SR lumen determines the relaxation rate of cardiac muscle. Also, SERCA determines the magnitude of SR Ca^{2+} stores that, when released, drive subsequent contractions of the heart. Thus, SERCA function also contributes to the strength of cardiac muscle contraction (21, 22, 26).

SERCA as a Potential Therapeutic Target

Cardiovascular disease is the leading cause of morbidity and mortality worldwide (30). A major contributor to this death toll is heart failure (HF), which is characterized by a reduced capacity of the heart muscle to pump blood to other organs through the vascular system. The 5-year survival rate of HF is approximately 50%. HF affects about 6.2 million adults in the US alone, and this number is projected to rise to over 8 million by 2030 (31, 32). Although HF encompasses a complex family of disorders, one common feature across various forms of heart failure is dysregulation of Ca^{2+} handling within cardiac muscle cells (33). Interestingly, SERCA expression is reduced in the hearts of patients across multiple sub forms of HF (34), contributing to the overall loss of Ca^{2+} signaling capacity in cardiac muscle. This finding has drawn attention to SERCA as a potential therapeutic target (35-38). The rationale being if SERCA function can be restored in the hearts of patients with HF, then disruptions in Ca^{2+} handling could be amended, and cardiac function could be restored. For these reasons, SERCA was

selected as the first gene therapy delivered to patients with HF (39-41). Unfortunately, potentially due to issues with delivery, SERCA gene therapy failed to meet clinical endpoints for efficacy in phase IIb clinical trials (41). This has refocused the field on developing small molecule activators of SERCA, in the hopes that by boosting the activity of the remaining SERCA pumps in failing heart, these molecules can ameliorate symptoms of heart failure in patients (42-45). However, in order to inform rational design of these therapies we need a clear understanding of the molecular mechanisms that regulate SERCA function. The goal of this study is to understand how SERCA regulation is dynamically adjusted to meet physiological demands.

CHAPTER TWO

REVIEW OF RELATED LITERATURE

Molecular Characterization of SERCA

SERCA is a member of the P-type ATPase family of cation transporters that serve housekeeping roles in cells by establishing electrochemical gradients across cell membranes that can be used for cell signaling (18, 21). These ion pumps harness energy from ATP to fuel active transport of their substrates from one cellular compartment to another (18, 46, 47). SERCA localizes to the ER membrane where it transports two Ca^{2+} ions from the cytoplasm into the ER lumen per catalytic cycle in exchange for two protons in order to establish an ER Ca^{2+} reservoir for cell signaling (46, 48). Ca^{2+} signals fueled by this concentration gradient are required for a broad array of functions including muscle cell contractions, neuronal transmission, and cell mobility (49).

Structurally, SERCA consists of a transmembrane (TM) domain composed of 10 membrane spanning α -helices and a cytoplasmic headpiece containing three functional domains: an actuator (A) domain, a nucleotide-binding (N) domain, and a phosphorylation (P) domain (Fig. 2A) (2, 21). SERCA binds Ca^{2+} in two substrate binding sites formed by acidic residues within the TM domain (21). SERCA facilitates Ca^{2+} transport by transitioning between two major conformation states: (1) a high Ca^{2+} affinity “E1” state where these residues face the cytosol and (2) a low Ca^{2+} affinity “E2”

state where the sites face the ER lumen (50-52). The SERCA enzymatic cycle is summarized by a simplified Post-Alber's scheme in Figure 2B (47).

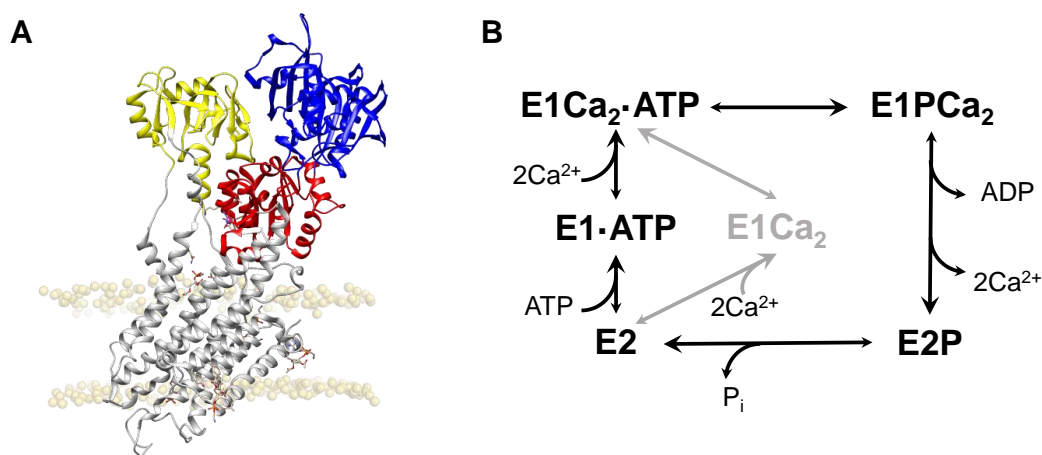


Figure 2. Molecular Characterization of SERCA. **A**, A crystal structure of SERCA (3W5C, grey) (2) labeling the A domain (yellow), N domain (blue), and P domain (red) of the cytoplasmic headpiece. **B**, A simplified Post-Albers scheme of the SERCA enzymatic cycle.

Each catalytic cycle begins when SERCA is in an E1 state, binding two Ca^{2+} ions in its transmembrane binding sites and ATP within the N domain. Once both ATP and Ca^{2+} are bound, SERCA hydrolyzes ATP transferring the gamma phosphate from the nucleotide to aspartate 351 in the P domain of SERCA (50, 53). This reaction forms a phosphoenzyme intermediate (E1P), which undergoes a subsequent isomerization reaction that translocates the Ca^{2+} ions towards the ER lumen (50). In this E2P state, the substrate binding residues populate a geometry with lower affinity for Ca^{2+} and higher affinity for protons. Ca^{2+} ions dissociate from the binding sites in the E2P state and are replaced by protons which diffuse into the luminal gate (54). The binding of protons to the E2P state is coupled to a dephosphorylation reaction of the enzyme to the proton bound E2 state (55). The E2 state of the pump is transiently formed during dephosphorylation as it is isomerized by a subsequent “E2 to E1” transition (50-52),

which translocates protons in the substrate binding pocket from the SR/ER lumen to the cytosol. After protons are released from the binding sites to the cytosol, the reaction cycle begins again in the E1 state of SERCA (21).

Since SERCA enzyme turnover is dependent on the binding of both ATP and Ca^{2+} , the relative affinity of SERCA for these substrates are critical determinants of its activity in cells. The equilibrium ATP binding constant (K_{ATP}) for SERCA1a was estimated by Inesi and colleagues to be roughly 7 μM in the presence of the cofactor Mg^{2+} and roughly 24 μM in the absence of Mg^{2+} (56). Estimates of K_{ATP} were made in the absence of Ca^{2+} in these studies in order to avoid enzyme turnover and hydrolytic cleavage of the nucleotide (56). SERCA affinity for Ca^{2+} in the absence of ATP is roughly 1-2 μM depending on the isoform (49). Although a lower binding constant for Ca^{2+} than ATP would suggest SERCA has higher affinity for Ca^{2+} , ATP is generally thought to bind before Ca^{2+} under physiological conditions in cells (53, 57). This is because, while cellular Ca^{2+} concentrations constitutively oscillate from low nM to low μM , ATP is tightly buffered at millimolar concentrations that would be saturating for SERCA. Even under ischemic conditions, ATP concentrations are only reduced by about 2-fold (57, 58). Therefore, SERCA generally binds ATP before Ca^{2+} under physiological conditions (57, 59). Only during peak systolic conditions in cardiac muscle, where Ca^{2+} concentrations approach 1 μM is Ca^{2+} binding before ATP possible depending on the local concentrations of these substrates near SERCA (59). For this reason, Ca^{2+} binding before ATP is displayed in Figure 2B as an alternative branch (grey) of the main pathway of the SERCA enzymatic cycle (black).

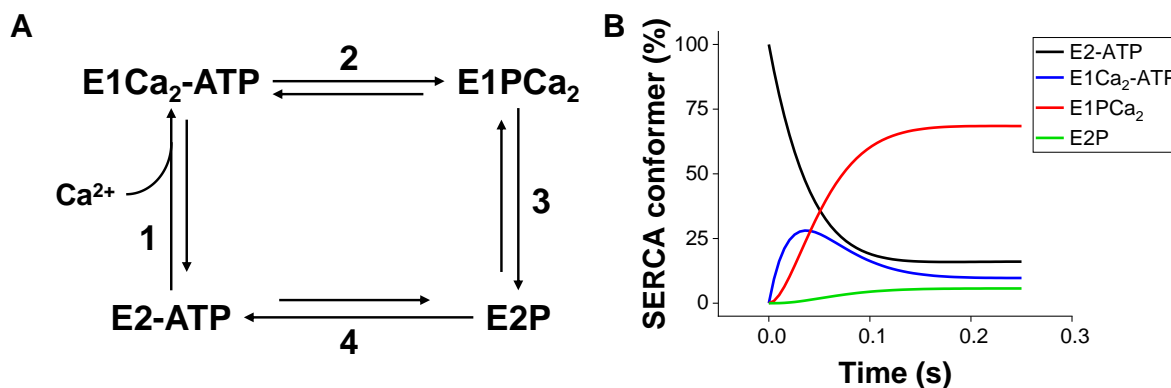


Figure 3. A Computational Model Simulates SERCA Cycle Kinetics. A, A schematic diagram of a 4-state model used to simulate SERCA conformational cycling. **B,** A simulation of how Ca²⁺ pump conformations redistribute when the SERCA catalytic cycle is active during cellular Ca²⁺ elevations. A description of the model and simulated rate constants can be found in Appendix B.

During intracellular Ca²⁺ elevations, SERCA samples all the intermediate states of the Ca²⁺ transport cycle, but these states are not all equally populated. Rather, the conformational poise of SERCA during Ca²⁺ transport is determined by the rates of the partial reactions in the catalytic cycle. To demonstrate how SERCA conformations redistribute during cellular Ca²⁺ elevations, we generated a 4-state computational model that utilizes published rate constants from the literature (49, 55, 60-62) to simulate the conformational cycling of SERCA (Fig. 3A). Here we assume that the binding of ATP and Ca²⁺ to SERCA are in rapid equilibrium during Ca²⁺ elevations relative to the conformational transitions of SERCA (57). The binding of these substrates is followed by a rapid ATP hydrolysis step (E1-ATP → E1PCa₂, $k = 35 \text{ s}^{-1}$) (60). The E1PCa₂ to E2P transition most notably limits the overall turnover rate of the cycle (5 s^{-1}) (60). Therefore, SERCA mainly accumulates in the E1PCa₂ state (~70%) which precedes this step during cycling (Fig. 3B, *blue*). The subsequent E2P dephosphorylation reaction is rapid at room temperature (60 s^{-1}) (55), while the conversion of phosphate-free E2

SERCA to E1 that follows is slower (25 s^{-1}) (60). This results in a mild accumulation of the enzyme in E2-ATP (~15%) during cycling (Fig. 3B, *black*). The forward rate of E2 → E1 is also strongly increased (>10-fold) by modulatory effects of ATP (63, 64) further limiting the accumulation of SERCA in an E2 state during transport. The overall turnover rate of SERCA has been estimated at roughly $3\text{-}5 \text{ s}^{-1}$ (65).

SERCA Regulation in Health and Disease

The gene encoding the cardiac SERCA2a and the more ubiquitous SERCA2b isoform, *ATP2A2*, is highly conserved in the human genome. Pathogenic mutations of *ATP2A2* are rare and result in an autosomal dominant form of Darrier disease, a skin disorder associated with a loss of adhesion between epidermis and keratin layers in patients (62, 66). Therefore, cardiac pathologies associated with SERCA2a do not stem from changes of the amino acid sequence of SERCA2a but rather from changes in the regulation of SERCA2a expression and function in the heart (34, 67).

Because of the critical role of SERCA in driving the cardiac cycle, it is no surprise that decreased SERCA2a expression is deleterious for healthy cardiac function. Indeed, SERCA expression has been found to be decreased by nearly 50% in the hearts of patients with heart failure in comparison to healthy human hearts (34, 68, 69), and this loss of SERCA is thought to a key step in the pathogenesis of heart failure (41, 68, 69). The functional impact of decreased SERCA expression in the heart is decreased relaxation efficiency and decreased contractile function.

Since cardiac function must constantly adjust to meet the rapidly changing physiological demands of the body, SERCA2a activity must also be dynamically regulated to adjust Ca^{2+} transport to match the needs of cardiac output. The primary

mechanism by which SERCA function is regulated is through protein-protein interactions with tissue-specific transmembrane micropeptides (70, 71). These micropeptides all possess a single membrane spanning alpha helix which competes with other micropeptides to bind a common regulatory cleft within SERCA's transmembrane domain formed by TM helices 2, 4, 6, and 9 of SERCA (21, 72).

Phospholamban (PLB)

In cardiac muscle, SERCA is primarily regulated by the inhibitory peptide, phospholamban (PLB) (70, 73). PLB is a 52 amino acid micropeptide consisting of a cytoplasmic α -helix and a transmembrane α -helix which binds to SERCA within the membrane (4) (Fig. 4A). Through its interaction with SERCA, PLB decreases the apparent Ca^{2+} affinity of the pump (Fig. 4B) (15, 70, 73, 74). PLB regulation of SERCA is considered to be critical for human survival since naturally occurring mutations of PLB that nullify its inhibitory function are associated with heart failure and premature death in carriers (67). Specifically, a truncating mutation of PLB that converts the gene sequence encoding leucine 39 of PLB to a premature stop codon (L39stop) was found to prevent proper localization PLB to the SR membrane. This caused PLB inhibition of SERCA to be virtually abolished and led to early death in homozygous carriers (67).

Although PLB reduces the Ca^{2+} sensitivity of SERCA during cycling, increasing the Ca^{2+} concentration required for pump turnover (Fig. 4B), it is not thought to affect the actual Ca^{2+} affinity of SERCA. Interestingly, equilibrium measurements of $^{45}\text{Ca}^{2+}$ binding to SERCA (in the absence of ATP) do not show any effect of PLB on the true Ca^{2+} affinity of SERCA (15, 75, 76). These apparently contradictory results can be reconciled by a kinetic mechanism. It is thought that PLB slows structural transitions

associated with the Ca^{2+} binding step of the SERCA enzymatic cycle. This explanation could account for the observed Ca^{2+} desensitization effect of PLB without reducing the true Ca^{2+} affinity of SERCA under equilibrium conditions (15).

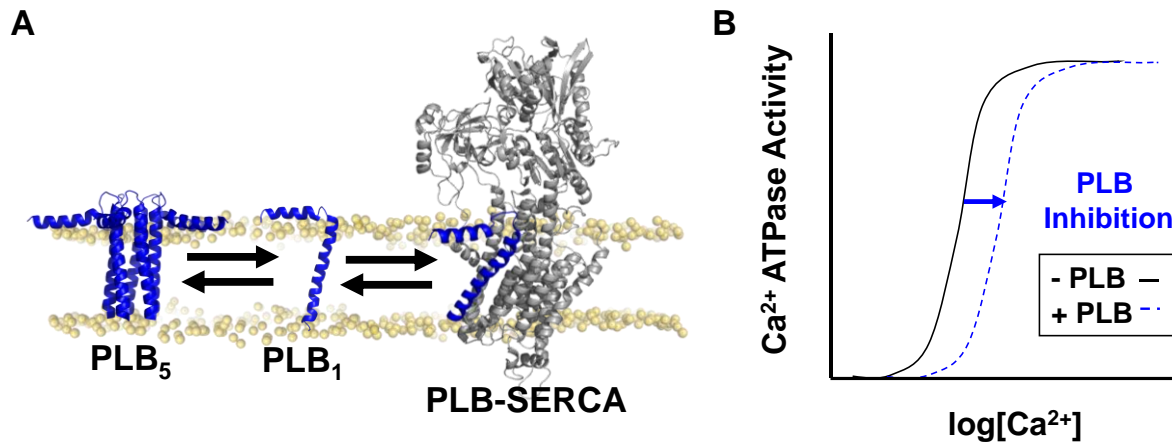


Figure 4. Phospholamban (PLB) Regulation of the Ca^{2+} ATPase (SERCA). **A** Structures: PLB pentamer (PLB₅), PDB: 2KYV (1); monomeric PLB (PLB₁), PDB: 1FJP (4); PLB-SERCA (5). **B**, A schematic diagram of the effect of PLB regulation on the Ca^{2+} -dependent ATPase activity of SERCA observed by past investigators (15).

PLB inhibition can be temporarily relieved when PLB is phosphorylated or at high concentrations of intracellular Ca^{2+} , providing mechanisms to increase SERCA Ca^{2+} transport in response to exercise or other physiological stress. Specifically, when the heart is stimulated by adrenaline binding β -adrenergic receptors, cAMP levels rise activating protein kinase A (PKA). PKA phosphorylates PLB at serine 16 to relieve inhibition (70, 73, 77). At very high Ca^{2+} concentrations (roughly $\geq 10 \mu\text{M}$), PLB inhibition of SERCA is intrinsically relieved independent of phosphorylation (15). Initially, the relief of SERCA inhibition was thought to require dissociation of the PLB-SERCA interaction after PLB phosphorylation or in high Ca^{2+} (78-82). However, subsequent studies showed that PLB-SERCA binding can still occur after PLB phosphorylation or in high Ca^{2+} (83-85), suggesting that PLB acts more like a subunit of a persistent SERCA

regulatory complex. These seemingly alternative models may be reconciled by observations that SERCA binds PLB with modestly reduced affinity in elevated Ca^{2+} (6, 72, 84). PLB must bind more tightly to SERCA conformations which predominate at low Ca^{2+} and bind less avidly to SERCA states that prevail at elevated Ca^{2+} (84). However, the affinity of PLB binding to specific intermediate SERCA conformers has not been measured, so how the energetics of this complex changes through the SERCA enzymatic cycle remains poorly understood.

PLB regulation of SERCA is also modulated during changes in cardiac pacing frequency and contributes to an increase in contractile force that occurs when heart rates accelerate during exercise. This phenomenon is known as *treppe*, the positive force-frequency relationship, or the Bowditch effect (86-90). The Bowditch effect, first characterized by Henry Bowditch in 1871 (86), is largely attributed to a frequency dependent increase in extracellular Ca^{2+} entry through L-type Ca^{2+} channels (91). This Ca^{2+} is subsequently incorporated into SR Ca^{2+} load by SERCA to increase the force of contractions at faster pacing. Although the exact molecular mechanism for relieving PLB inhibition in response to accelerating cardiac pacing frequency remains unknown, it is clear that PLB is a major determinant of the force-frequency relationship since this phenomenon is virtually abolished in PLB-KO mice (88, 89) and is potentiated by increasing PLB to SERCA expression ratio (87).

In addition to the modulation of PLB inhibition by phosphorylation, Ca^{2+} , and accelerated pacing frequency, PLB inhibitory potency is also influenced by its ability to homo-oligomerize with itself. PLB binds and inhibits SERCA in its monomeric form, but when unbound from SERCA, PLB monomers assemble to form PLB pentamers (92)

(Fig. 4B). PLB pentamers represent an inactive reserve pool (93) that buffers the concentration of inhibitory monomers available to bind SERCA. This buffering effect may be enhanced by adrenergic stimulation, since PLB pentamers are further stabilized by PLB phosphorylation (94, 95). The rates at which PLB exchanges between SERCA- and pentamer-bound pools must govern how quickly these complexes can redistribute *in vivo*. We (96) and others (97) have provided evidence that the exchange of PLB monomers from pentamers occurs slowly relative to rapid exchange from the SERCA regulatory complex, but the underlying kinetics of these binding events have not been definitively measured. Therefore, the degree to which these regulatory complexes may dynamically redistribute in the cardiac SR remains unclear.

Dwarf open reading frame (DWORF)

PLB competes for SERCA binding with another membrane micropeptide expressed in the heart, dwarf open reading frame (DWORF) (98), which is shown in red in Figure 5A (7). The RNA transcript for DWORF was originally annotated as long non-coding RNA because its short, 34 codon length did not meet an arbitrary minimum threshold of 200 nucleotide base pairs that had previously been applied to screen for coding genes (98, 99). A more inclusive screening of the mouse genome identified the previously unrecognized open reading frame as an mRNA transcript encoding the 34 amino acid micropeptide DWORF (98). In mice, DWORF expression has been found to be specific to the heart and soleus muscles. Although currently available antibodies are very specific to the mouse DWORF amino acid sequence (Appendix Figure B.1), DWORF mRNA has also been detected in the healthy human heart at similar levels as natriuretic peptide A, so presumably DWORF is also expressed in human cardiac

muscle. Interestingly, DWORF mRNA expression was found to be reduced in the hearts of patients with heart failure (98) similar to previously reported decreases in SERCA expression (69).

In contrast to PLB, DWORF activates Ca^{2+} transport through its regulatory interaction with SERCA (Figure 5B). This stimulatory effect is thought to be mediated both directly by DWORF alone interacting with the pump (6) and indirectly through displacing inhibitory PLB from the SERCA regulatory cleft (98). Our lab has previously shown that while DWORF does not display strong affinity for binding with itself, it has similar SERCA-binding affinity as PLB in harmony with its role as a competitor for PLB in the heart (92). Due to the activating effect of this newly discovered SERCA regulator, much attention has been drawn to DWORF as a potential candidate for gene therapy to treat heart failure. Thus far, DWORF expression has achieved promising results in ameliorating symptoms in animal models of dilated cardiomyopathy (38, 100), ischemia/reperfusion injury (101), and Duchenne muscular dystrophy (102) cardiomyopathy.

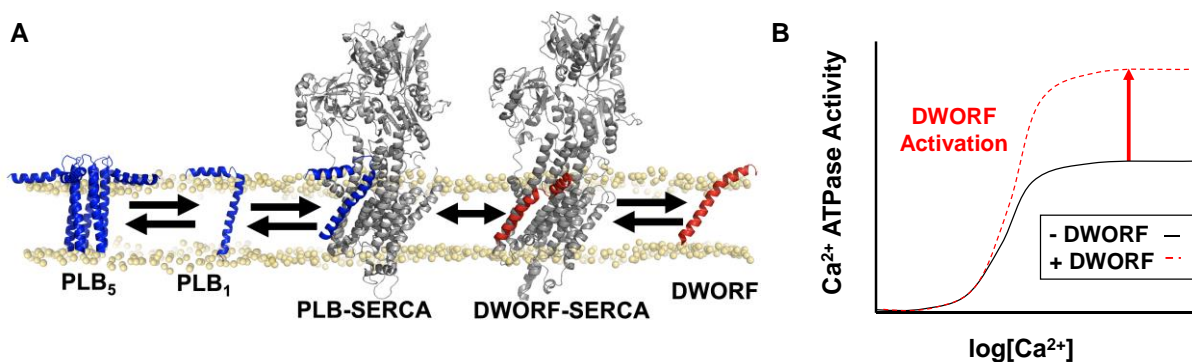


Figure 5. DWORF Competes with PLB for Regulation of SERCA. **A**, Structures: PLB₅, PDB:2KYV (1); PLB₁, PDB:1FJP, (4); PLB-SERCA, DWORF-SERCA (5, 6); DWORF, PDB: 7MPA, (7). **B**, A schematic diagram of the effect of DWORF activation on the Ca^{2+} -dependent ATPase activity of SERCA observed by past investigators (6).

Interestingly, our recent work showed that DWORF–SERCA affinity shows an opposite Ca^{2+} -dependence compared to PLB–SERCA. That is, DWORF affinity for SERCA increases with elevated Ca^{2+} (6). This implies dynamic competition of stimulatory and inhibitory micropeptides: Ca^{2+} elevations favor DWORF binding to SERCA, but PLB becomes more competitive as Ca^{2+} levels fall. In Chapter X, we measured the dynamic binding of DWORF and PLB to SERCA during cellular Ca^{2+} oscillations to understand how the exchange of micropeptides may be important for dynamically responsive regulation. We have previously used fluorescence resonance energy transfer (FRET) to examine shifts in the PLB–SERCA binding equilibrium in paced cardiac myocytes (84). However, motion artifacts and competing, non-FRET interactions with endogenous PLB/SERCA prevented a detailed analysis of exchange and equilibration rates in that study. To circumvent those experimental barriers, we exploited a more well-controlled model system that mimics cardiac calcium handling. We interpreted these observations with a computational model that incorporates experimentally measured rate constants. This reductionist strategy yielded mechanistic insight into how regulatory equilibria shift during the cardiac cycle, and, on a longer timescale, how Ca^{2+} handling may adapt between rest and exercise. The results may inform future efforts to develop therapeutic strategies based on gene delivery of micropeptides (38, 100-102).

CHAPTER THREE

MATERIALS AND METHODS

Molecular Biology and Cell Culture

pEGFP-C1 was used as an expression vector for all SERCA and regulatory micropeptides (PLB, DWORF, etc.). Constructs were labeled with N-terminal fluorescent protein tags (EGFP, mCerulean3, EYFP, etc.) separated by a 5 amino acid linker (aa sequence: SGLRS). Two-color SERCA was developed by inserting another, interdomain tag in the N domain sequence of SERCA. Our lab has previously demonstrated that the fusion of one or two fluorescent proteins onto SERCA did not alter normal Ca^{2+} transport function (44, 65, 103). Furthermore, PLB fused to another tag was able to normally regulate SERCA function (65). Therefore, we believe fluorescent protein labels are benign for the normal function of SERCA and PLB. Mutant constructs were created using the QuikChange II XL mutagenesis kit (Agilent Technologies). HEK-293 cells (Agilent, Santa Clara, CA, USA) were cultured in DMEM cell culture medium with 10% fetal bovine serum. Cells were then transfected using either the MBS mammalian transfection kit (Agilent Technologies, Stratagene) or Lipofectamine 3000 transfection kit (Invitrogen) as per instructions provided with the respective kits. The expression of SERCA and PLB achieved in transfected HEK cells is measurably lower than the expression levels of these proteins in the human heart samples, as determined by western blot (Appendix Figure B.1). Therefore, we do not consider this experimental system to be overexpression.

Human Heart Tissue Procurement

Human left ventricular tissue was provided by Loyola Cardiovascular Research Institute Biorepository. The sample collection was approved by Loyola University Review Board (IRB number 210940821918) and written informed consent was obtained for collection of heart tissue according to the Declaration of Helsinki.

Human Tissue Membrane Protein Enrichment

Frozen heart tissue was placed in 5 mL of a solution containing 100 mM KCl, 2.5 mM K_2HPO_4 , 2.5 mM KH_2PO_4 , 2 mM EDTA, and protease inhibitor cocktail (Santa Cruz Biotechnologies). Samples were mechanically homogenized with an Omni International GLH-01 homogenizer and rotated for 1 hour at 4°C. Homogenates were centrifuged at 10,000 x g for 20 min at 4°C. Supernatants were collected and centrifuged at 48,000 x g for 1 hour at 4°C. The pellet containing membrane fractions was resuspended in 100 μ L of a solution containing 1 M sucrose and 50 mM KCl.

HEK Cell Microsomal Membrane Preparation

Cells were cultured in 15 cm dishes and transfected with 90 μ g of 2-color SERCA plasmid DNA. For samples co-expressing unlabeled PLB with 2-color SERCA, 50 μ g of 2-color SERCA DNA was used with unlabeled PLB DNA at a 1:3 or 1:5 SERCA to PLB ratio. To harvest cells, 48 hours post transfection, cell culture dishes were placed on ice and scraped for approximately 5 minutes with a cell scraper while cells were bathed in 10 mL of cold homogenizing solution (0.5 mM $MgCl_2$, 10 mM Tris-HCl pH 7.5, and EDTA-free protease inhibitor cocktail). Harvested cells were collected, pelleted by centrifugation at 1000 x g for 10 min at 4°C, and resuspended in 5 mL of homogenizing solution. Cells were then homogenized by applying 40 strokes in a Potter-Elvehjem

homogenizer, then 5 mL of cold sucrose solution (100 mM MOPS pH 7.0, 500 mM sucrose, and EDTA-free protease inhibitor cocktail) was added and an additional 20 strokes was applied. Cells were further homogenized by being passed 10 times through a 27-gauge needle. To prepare microsomal membranes, homogenates were pelleted by centrifugation at 1000 x g for 10 min at 4°C, and the low-speed supernatants were transferred to a thick wall polycarbonate ultra-centrifugation tube and centrifuged at approximately 120,000 x g for 30 min at 4°C. The supernatants were discarded, and the high-speed pellets were resuspended in 100 µL of a 1:1 mixture of homogenizing solution and sucrose solution. Finally, these supernatants were homogenized by 20 strokes in a Potter-Elvehjem homogenizer and passed through a 27-gauge needle 10 times.

Western Blotting and Protein Thermostability Assays

Total protein concentrations of samples were determined using a Pierce bicinchoninic acid protein assay kit. Thirty micrograms of sample were diluted in 4x Laemmli sample buffer with β -mercaptoethanol at 1:1 ratio, denatured at 90°C for 5 min, run on a 4 to 15% polyacrylamide gradient gel, and transferred to a polyvinylidene difluoride membrane. The membrane was stained with Revert total protein stain (LI-COR Biosciences) for 5 min to obtain total protein in each lane and then blocked for 1 hour at room temperature in Intercept blocking buffer (LI-COR Biosciences) diluted at a 1:1 ratio in PBS with Tween 20 (PBS-T). Blots were incubated overnight at 4°C with primary antibody diluted 1:1000 in PBS-T: mouse anti-SERCA2 (abcam; ref# ab2817; IID8), mouse anti-PLB (Invitrogen; ref# MA3-922; 2D12), or rabbit anti-DWORF (98) (a gift from Catherine Makarewich, Cincinnati Children's Hospital). The anti-DWORF

antibody was a custom polyclonal antibody derived against the N-terminal region of the mouse DWORF protein sequence (MAEKESTSPHLI) and did not react with human DWORF (Appendix Figure B.1). The blots were then incubated with anti-mouse (IRDye 680RD; LI-COR Biosciences) or anti-rabbit (IRDye 800CW; LI-COR Biosciences) secondary antibody diluted 1:10,000 in PBS-T. Blots were imaged using an Azure c600 gel imaging system and analyzed using the LI-COR Image Studio software.

Western blots evaluating the effect of R14del mutation on PLB pentamer stability were conducted in collaboration with the Gramolini lab at University of Toronto. Briefly, transfected HEK-293 cells were washed twice with ice-cold 1x phosphate-buffered saline (pH7.4; 137 mM NaCl, 2.7 mM KCl, 8 mM Na₂HPO₄, 2 mM KH₂PO₄) and protein lysates were harvested in 8 M urea (BioShop, URE001, Toronto, Canada), supplemented with protease inhibitors (Roche, 04574834001). Protein lysates were sonicated. Insoluble fractions were spanned down at 15,000xg for 15 minutes at room temperature and cell-free lysates were transferred to a new Eppendorf tube. Protein concentration was qualified by Bradford assays (Sigma-Aldrich, B6916-500 mL). 30 µg soluble proteins were resolved on a 15% sodium dodecyl sulphate poly acrylamide gel via electrophoresis (SDS-PAGE) at 90 V, followed by electrophoretic transfer of proteins to a 0.22 µm nitrocellulose membrane (Bio-Rad, Cat#1620112) at 65 V for 60 minutes. A membrane was blocked with 5% non-fat milk in Tris-buffer saline (TBST, 20 mM Tris-HCl; pH7.4, 150 mM NaCl, 0.1% (w/v) Tween 20). 0.1 µg/mL anti-PLB antibody (ThermoFisher, Cat#MA3-922) in TBST was added to the membrane and incubated overnight at 4°C on a rotor. Next morning, the membrane was washed 3 times with TBST. HRP-conjugated anti-mouse antibodies (Promega, Cat#W4021) in TBST was

added to membranes and rocked on a rotator for 1 hour at the room temperature. Membranes were washed 3 times with TBST, incubated with chemiluminescent reagents (ThermoFisher, Cat# 32209) in the dark for 5 minutes. Immunoblot signals were captured by ChemiDoc (Bio-Rad). Densitometry analysis of signal intensity was carried out in Image Lab software (Bio-Rad) as per manufacturer's instruction. For protein thermostability assays, cell-free lysates in 8 M urea were thoroughly mixed with protein loading dye before heated up in a range of temperature (25~70°C, 5°C increments) for 2 minutes in a thermo-cycler. Lysates were then subjected to SDS-PAGE runs. % PLB oligomers was estimated as the following. Percentage PLB oligomers = $\frac{\text{Avg. oligomer density}}{(\text{Avg. monomer density} + \text{Avg. oligomer density})} * 100\%$.

FRET Acceptor Sensitization

HEK-293 cells were transiently transfected with donor and acceptor labeled constructs of binding partners at a 1:5 M plasmid ratio. Twenty-four to 48 hours post transfection, cells were trypsinized and reseeded to chamber slides coated with poly-D-lysine. Cells were imaged using an inverted microscope (Nikon Eclipse Ti2). Field of view images were acquired with a 20X objective, numerical aperture 0.75. A Lumencor Spectra X excitation system was used to excite samples with 50 ms exposure time for mCeruleon donor (excitation: 420/440 nm, detection: 475 nm), YFP acceptor (excitation: 510/525 nm, detection: 540 nm), and FRET (excitation: 420/440 nm, detection: 540 nm) channels (Fig. 6A). Emitted light was passed through a dichroic emission filter cube (CFP/YFP/mCherry Spectra X emission filter set) before detection with a Photometrics Prime 95B 25 mm camera. Seventy-two images were collected for each channel in a 9 x 9 grid with a 1600 μm step size between each image. Typically, for each condition,

two sets of images were collected (yielding ~500 cells minimum per condition) from multiple independent experiments. Whole cell fluorescence intensity was quantified from images using automated analysis with a custom script in FIJI software. Specifically, cells with a minimum mCer intensity of 250 AU and an area of 136 – 679 μm^2 with at least 40% circularity were selected for high throughput cell scoring with rolling background subtraction. Fluorescence intensities from mCer, YFP, and FRET channels (I_{DD} , I_{AA} , and I_{DA} respectively) were used to calculate sensitized emission FRET according to the formula $E_{app} = F_c / (F_c + G \times I_{DD})$, where $F_c = I_{DA} - (a \times I_{AA}) - (d \times I_{DD})$. Here, F_c represents the sensitized emission FRET intensity corrected for crosstalk between channels and E_{app} represents the apparent FRET efficiency corrected for imaging induced photobleaching. The parameters d and a are crosstalk constants calculated as $d = I_{DA}/I_{DD}$ for a control sample transfected only with the mCer donor (Fig. 6B) and $a = I_{DA}/I_{AA}$ for a control sample transfected only with the YFP acceptor (Fig. 6C). G is the ratio of sensitized acceptor emission to a corresponding amount of donor recovery in the I_{DD} channel after acceptor photobleaching (I_{DD}^{post}), defined by the equation $G = F_c / (I_{DD}^{post} - I_{DD})$ (104, 105). Figure 6D shows that G is constant in cells expressing a CFP-5aa linker-Venus (C5V) construct over a range of Venus protein expression. For the experiments in this study using mCer and YFP FRET pairs, these values were determined to be $a = 0.1853$, $d = 0.4051$, and $G = 2.78$. For experiments using GFP and TagRFP as donor and acceptor respectively, $a = 0.06091$, $d = 0.08105$, and $G = 0.5928$. Experiments with mCer donor and TagRFP acceptor pairs used $a = 0.05$, $d = 0.1$, and $G = 0.7$.

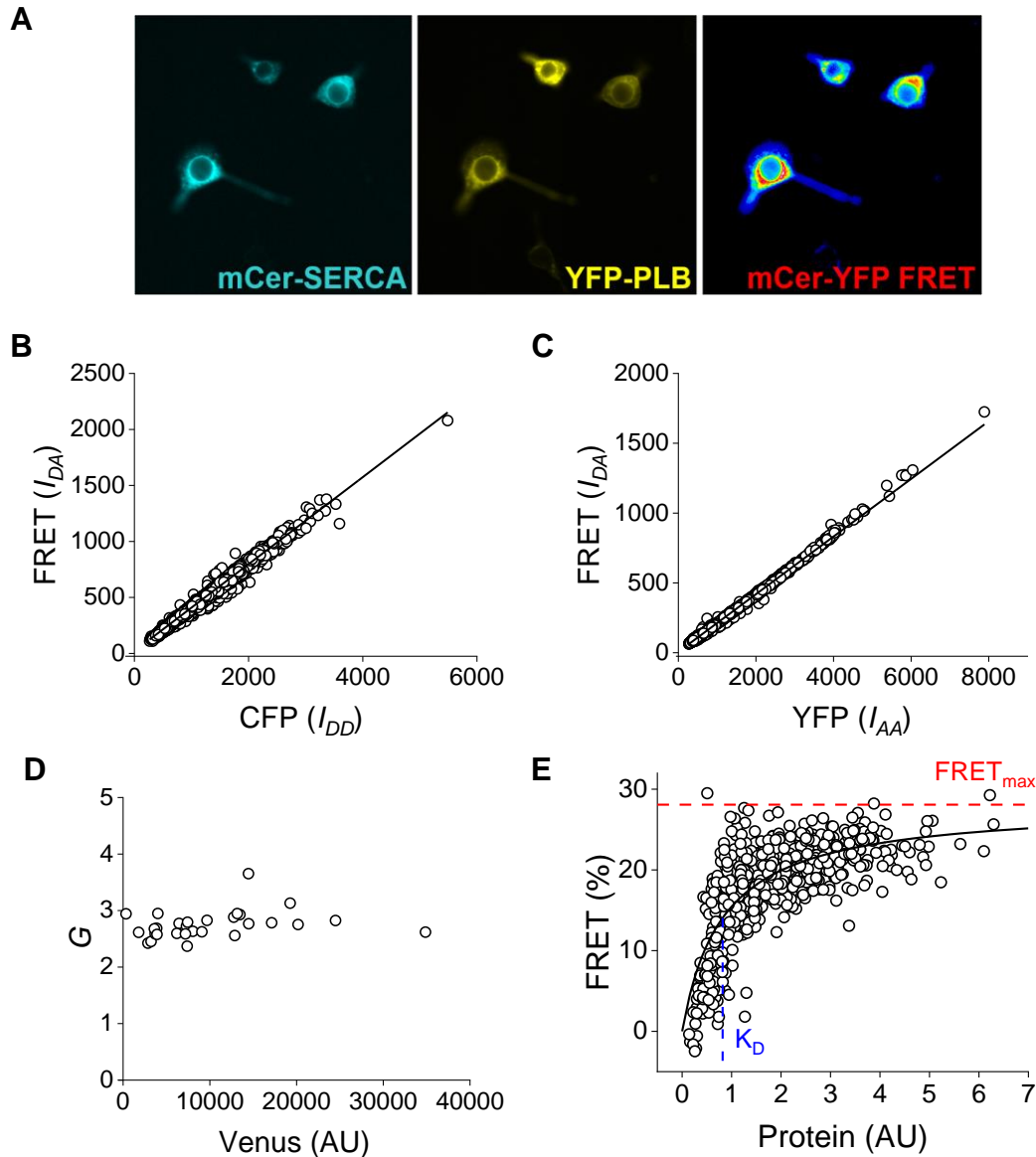


Figure 6. Photobleaching-corrected FRET Efficiency Measures Membrane Protein-Protein Interactions in Live Cells. **A**, mCer-SERCA, YFP-PLB, and “FRET” images obtained by automated fluorescence microscopy. **B**, Increasing CFP expression results in a constant increase in the amount of bleedthrough in the FRET channel, giving the crosstalk constant d . **C**, Increasing YFP expression results in a constant increase in the amount of bleedthrough in the FRET channel, giving the crosstalk constant a . **D**, The G parameter, determined in a sample expressing a control C5V construct, is constant in cells across a range of protein expression. **E**, A FRET-based binding curve measuring the concentration dependent binding between mCer-SERCA2a and YFP-SERCA2a. A hyperbolic fit reveals the FRET_{max} (red) and relative K_D (blue) for the interaction of SERCA dimers.

Apparent FRET efficiencies for each cell were then plotted as a function of acceptor fluorescence intensity, which was used as an index of relative protein expression (106). This plot yielded a FRET-based binding curve, illustrating the relative concentration dependence of E_{app} (Fig. 6E). FRET efficiency was low in cells with low protein expression, increasing to a maximum in the cells with the highest protein expression. The data were fit with a hyperbolic function of the form $FRET = FRET_{max} \times Protein / (K_D + Protein)$, where $FRET_{max}$ is the maximal FRET efficiency at high protein concentration (representing the intrinsic FRET efficiency of the bound complex), $Protein$ is inferred from the relative YFP fluorescence intensity in each cell, and K_D is the relative dissociation constant (the protein concentration that yields half-aximal FRET efficiency). The K_D is inversely related to the relative affinity of the protein-protein interaction.

Cell Permeabilization and Manipulated Cytoplasmic Conditions

For cell permeabilization experiments, cells were seeded to a chamber slide coated with poly-D-lysine and allowed to adhere overnight before imaging. To selectively permeabilize the plasma membrane, cells were washed with PBS and then permeabilized for 1 min with 0.05 mg/mL saponin. After permeabilization, saponin solution was slowly removed from the chamber slide and then gently washed with a low Ca^{2+} , high K^+ solution (100 mM KCl, 5 mM $MgCl_2$, 2 mM EGTA, and 10 mM imidazole, pH 7.0) to remove remaining detergent. The wash solution was then replaced with the final experimental condition. For experiments comparing SERCA-micropeptide binding in low and high intracellular Ca^{2+} conditions, solutions were prepared containing potassium aspartate 120 mM, KCl 15 mM, KH_2PO_4 5 mM, $MgCl_2$ 0.75 mM, dextran 2%,

ATP 5 mM, Hepes 20 mM, and EGTA 2 mM, pH 7.2. The elevated $[Ca^{2+}]_i$ buffer was prepared with $CaCl_2$ 1.7 mM for a free $[Ca^{2+}]_i = 2 \mu M$ (107).

To control the conformational poise of SERCA with stabilizing ligands, cells were imaged in bath solutions prepared by adding saturating concentrations of the appropriate ligands to a low Ca^{2+} base solution, which includes 100 mM KCl, 5 mM $MgCl_2$, 2 mM EGTA, and 10 mM imidazole, pH 7.0. The base solution was used to characterize SERCA in a ligand-free state, E_{apo} . The following ligands were used to prepare specific solutions corresponding to biochemical states of SERCA: 100 μM thapsigargin (TG) for $E_2(TG)$; 3 mM ATP for E_1-ATP ; 2.1 mM $CaCl_2$ for $E_1(Ca_2)$ with free $[Ca^{2+}]_i = 100 \mu M$ (107); 2.1 mM $CaCl_2$ and 500 μM nonhydrolyzable ATP analog (AMPPCP) for $E_1(Ca_2-AMPPCP)$; 2.1 mM $CaCl_2$, 500 μM ADP, 50 μM $AlCl_3$, and 3 mM KF for $E_1(Ca_2-ADP-AlF_4^-)$; 0.1 mM orthovanadate for $E_2(V_i)$; and 50 μM $AlCl_3$ and 3 mM KF for $E_2(AlF_4^-)$. Concentrations of AMPPCP nucleotide analog and ADP nucleotide were reduced from previously published conditions (3 mM) used to stabilize SERCA in microsomal fractions (103) to prevent altering fluorescent protein emission intensity in live cells (Appendix Fig. B.2).

For experiments measuring PLB-binding preference for SERCA enzymatic states E_2-ATP and E_1-ATP , which are in equilibrium under low Ca^{2+} , high ATP conditions (e.g., cardiac diastole), a buffer containing 100 mM KCl, 5 mM $MgCl_2$, 2 mM EGTA, 10 mM imidazole, and 3 mM ATP was prepared. The pH was then adjusted to the following concentrations: pH = 6.0, 6.5, 7.0, 7.5, and 8.0. For these experiments, a TagRFP-PLB acceptor construct ($pK_a = 3.8$) was used in place of the YFP-PLB acceptor because YFP fluorescence is sensitive to pH changes in this range ($pK_a = 6.9$) (108). The crosstalk

coefficients for photo-bleaching correction of FRET efficiency (105) were adjusted from those used for FRET measurements between mCer and YFP to give a hyperbolic relationship for the tagRFP acceptor.

Confocal Fluorescence Microscopy to Measure Intermolecular FRET and HEK-293 Cytoplasmic Ca²⁺

HEK-293 cells exhibiting spontaneous Ca²⁺ oscillations were generated by transient transfection with GFP-tagged RyR2 and either Cer or unlabeled SERCA2a and co-transfected with SERCA, PLB (WT or mutant), or DWORF FRET pairs tagged with Cer and YFP fluorophores. Transfected cells were cultured for 24 h and seeded into poly-D-lysine-coated glass bottom chamber slides in DMEM plus 10% fetal bovine serum. Experiments were conducted with a Leica SP5 laser scanning confocal microscope equipped with a 63x water objective. To observe transient changes in cytoplasmic calcium, cells were incubated with 10 μM X-Rhod-1/AM (X-Rhod) for 20 min in PBS (+Ca²⁺/+Mg²⁺) and then subsequently washed twice with dye-free PBS. X-Rhod was excited with the 543 nm line of a He-Ne laser, and emitted fluorescence was measured at wavelength 580 nm. FRET pair fluorophores Cer and YFP were excited with the 430 and 514 nm lines of an argon laser, respectively, and emitted fluorescence was measured at wavelengths 485 ± 15 and 537 ± 15 nm, respectively. Images were acquired in line scan with averaging of four every 134 ms for ~2 min.

A select set of concurrent experiments were conducted with a Zeiss LSM 880 confocal microscope using a 40x oil immersion objective. X-Rhod was excited with the 594 nm line of a He-Ne laser, and emitted fluorescence was measured at wavelength 580 nm. FRET pair fluorophores Cer and YFP were excited with the 458 nm line of an

argon laser, and emitted fluorescence was measured at wavelengths 485 ± 15 and 537 ± 15 nm, respectively. Images were acquired in line scan every 24 ms for ~2 min. This faster acquisition rate was used to resolve time-dependent changes in FRET signals during the fast upstroke of cellular Ca^{2+} elevations. FRET ratio was determined by dividing the acceptor fluorescence by the donor fluorescence and plotted as a function of time with X-Rhod to indicate concurrent changes in $[\text{Ca}^{2+}]$. FRET ratio data was smoothed using a Savitzky–Golay binomial filter with a 4.08 s averaging window. Changes in FRET ratio and X-Rhod fluorescence associated with Ca^{2+} uptake were fit to the single-exponential decay function, $y = A1^{-x/\tau} + y_0$ in Origin software, to estimate the time constant or τ of the change, where $A1$ is the amplitude of change and y_0 is the initial detected fluorescence. Changes in FRET ratio and X-Rhod fluorescence associated with Ca^{2+} release were fit using the single-exponential decay function, $y = A1^{-(x-x_1)/\tau} + y_1$, where x_1 is the time in seconds of Ca^{2+} release, and y_1 is the baseline fluorescence prior to x_1 , defined by the linear function $y = A1 + y_1$. Differences in the characteristic time constants (τ) for each process were analyzed using a one-way ANOVA with Dunn’s post hoc test (significance = $p < 0.05$).

Kinetic Modeling and Model Data Availability

Kinetic models and simulations were designed and performed in collaboration with the Kekenos-Huskey lab at Loyola. Briefly, we implemented systems of ordinary differential equations according to the schematic provided in Appendix B (Fig. B.10) (109). This kinetic diagram describes the populations of PLB and DWORF binding to SERCA states under diastolic and systolic conditions. Model parameters were informed or constrained by experimental observations where appropriate, such as the PLB

dissociation rates reported in this study. Mean rates were determined by averaging over several transients from multiple cells. Kinetic parameters for PLB–SERCA binding dynamics were fit from 15 independent FRET transients, while kinetic parameters for DWORF–SERCA interactions were fit from 9 independent FRET measurements. All other parameters were assigned initial values that were subject to fitting against time-varying FRET data. The relative affinity of PLB for SERCA (here described by the rate fraction of k_{on}/k_{off}) was constrained to be two-fold higher for Ca-free versus Ca-bound ensembles, as determined experimentally from FRET-binding curves. Likewise, the relative affinity of DWORF for SERCA (k_{on}/k_{off}) was constrained to increase by 25% between Ca-free and Ca-bound ensembles, consistent with FRET measurements. The ordinary differential equation system was numerically solved using the `scipy` (v1.5.0) `SOLVE_IVP` function, using experimentally measured intracellular Ca^{2+} transients as an input to the model. The resulting numerically estimated PLB–SERCA population was compared against the experimentally reported FRET data by assuming that the PLB–SERCA population was proportional to the FRET efficiency. Mean-squared error between the predicted PLB–SERCA population and the FRET data was computed to assess the fit. Fitting was optimized using a genetic algorithm we developed previously (110) that reduces the mean-squared error by randomizing model parameters and selects those that reduce error. Forward simulations of the SERCA/PLB/DWORF equilibria for the cardiac pacing experiments used simulated Ca^{2+} transients with amplitudes and frequencies in place of those measured in HEK cells for fitting purposes. A parameter sensitivity analysis as well as more details about the model are provided in

Appendix B. All code written in support of this model are publicly available at

<https://github.com/huskeypm/pkh-lab-analyses>.

An additional system of ordinary differential equations was used to describe how SERCA conformation redistributes between 4 states (E2-ATP, E1Ca₂-ATP, E1PCa₂, and E2P) as Ca²⁺ rises from diastolic to systolic concentrations (Fig. 3 and Appendix Table B.8). Rate constants from stopped-flow measurements from the literature (49, 55, 60-62) were used to inform the kinetic parameters of the model (Appendix Table B.9). At the start of the simulation, SERCA was assumed to be 100% in the E1Ca₂-ATP state to reflect the low Ca²⁺ ATP bound state, E1-ATP (59). The ordinary differential equation system was numerically solved using the scipy function SOLV_IVP as described in the previous paragraph. Forward simulations of the SERCA catalytic cycle were compared to the specific activity of SERCA which has been estimated at an overall turnover rate of roughly 3-5 s⁻¹ (65). More details about the model and simulated parameters can be found in Appendix B.

Time-Correlated Single Photon Counting (TCSPC)

To measure intramolecular FRET between donor (mCyRFP1) and acceptor (mMaroon) fluorescent proteins tagged to the N and A domains of the SERCA headpiece respectively, fluorescence lifetime measurements were obtained from microsomal membrane fractions expressing MO509 (mMaroon on the A domain and mCyRFP1 at residue 509) 2-color SERCA with or without unlabeled PLB co-expressed. Membranes were diluted at a 1:10 ratio in a solution containing 100 mM KCl, 5 mM MgCl₂, 10 mM imidazole, 2 mM EGTA, and varying concentrations of CaCl₂. For the nucleotide bound condition, 500 μM AMPPCP was added to solutions. The mCyRFP1

donor was excited with a supercontinuum laser (FIANUM) filtered through a 482/18 nm bandpass filter. Emitted fluorescence was detected through a 1.2 N.A. water immersion objective and transmitted through a 593/40 nm bandpass filter to a PMA Hybrid series detector (PicoQuant). Light from the detector was quantified with a HydraHarp 400 single photon counting module at 16 ps resolution. TCSPC histograms were obtained over 60 s acquisition period for each condition. TCSPC histograms were fit with the multiexponential function of the form $I(t) = \sum_i \alpha_i e^{-t/\tau_i}$, where I is intensity, t is time, α is the fractional amount of the fluorophore in each environment, and τ is the time constant for the lifetime decay (111). In control experiments with singly-labeled mCyRFP1-SERCA alone, the donor alone gave a single-exponential decay with a τ_D of 3.52 ns (Appendix Fig. E.1). Histograms for 2-color SERCA samples were well described by a 2-exponential decay function which was used to derive the average lifetime for the two 2-color SERCA populations (τ_{DA}). FRET efficiencies were calculated for each sample according to the relationship $FRET = 100 \times ((1 - \tau_{DA}) / \tau_D)$ (112) and plotted as a function of Ca^{2+} concentration. The data were well described by a Hill function of the form $y = START + ((END - START) * x^n) / (K^n + x^n)$, where $START$ is the minimal FRET efficiency at low Ca^{2+} , END is the maximum FRET efficiency at high Ca^{2+} , n is the Hill coefficient, and K is the Ca^{2+} binding constant (K_{Ca}). Data from 7 independent experiments from 6 microsomal preparations were global fit to obtain a single best Hill coefficient with independent K_{Ca} values for each experimental condition.

Fluorescence Correlation Spectroscopy (FCS)

Microsomal membrane preparations of HEK-293 cells expressing RG509 (TagRFP on the A domain and EGFP on the N domain) 2-color SERCA were diluted

roughly 1:10 in a low Ca^{2+} base solution containing 100 mM KCl, 5 mM MgCl_2 , 2 mM EGTA, and 10 mM imidazole, pH 7.0., containing 0.5% C_{12}E_8 detergent to solubilize SERCA. For various experimental conditions, stabilizing ligands were added to this base solution at saturating concentrations similar to those used in cell permeabilization experiments (e.g. 500 μM ATP, 100 μM TG, etc.). The detergent treated microsomes were supernatants were spun down in a bench-top microcentrifuge at 16,000 x g for 5 min at 4C to remove excess debris. After microcentrifugation, the supernatants were moved to a fresh tube and diluted in a ligand-containing solution in an 8-well chamber slide for data collection. Effective concentrations for acquiring single-molecule data varied depending on the sample and were determined based on test measurements. Both donor and acceptor were excited using a supercontinuum laser (FIANUM) which was split by a dichroic mirror into two separate light paths for pulsed interleaved excitation (PIE) of the donor and acceptor channels (113). The GFP excitation line was passed through a 482/18 bandpass filter and the tagRFP line was passed through a 563/9 bandpass filter. Emitted fluorescence was detected through a 1.2 N.A. water immersion objective and transmitted to a PDM series detector (PicoQuant). Light from the detector was quantified with a HydraHarp 400 single photon counting module at 16 ps resolution. Donor and acceptor fluorescence signals were acquired over a 20 minute acquisition period for each independent experiment and condition (Fig. 7A). The autocorrelation function of the fluorescence fluctuations of the donor (G_{DD}) and acceptor (G_{AA}) signals were generated in SymphoTime software (113, 114). This data reveals information about the relative rate of diffusion of fluorescent molecules in solution. The autocorrelation curves in Figure 7B show how the diffusion time ($\tau_{\text{diffusion}}$) of a rhodamine

dye accelerates in methanol and slows in 40% glycerol relative to water. A cross-correlation function was also generated for the donor and acceptor signals (G_{DDxAA}) (113). The ratio of the G_{DDxAA} and G_{DD} signals was taken to generate an FCS-FRET curve which is independent of the diffusion contributions and reveals information about the dynamics of 2-color SERCA headpiece motions (113, 115).

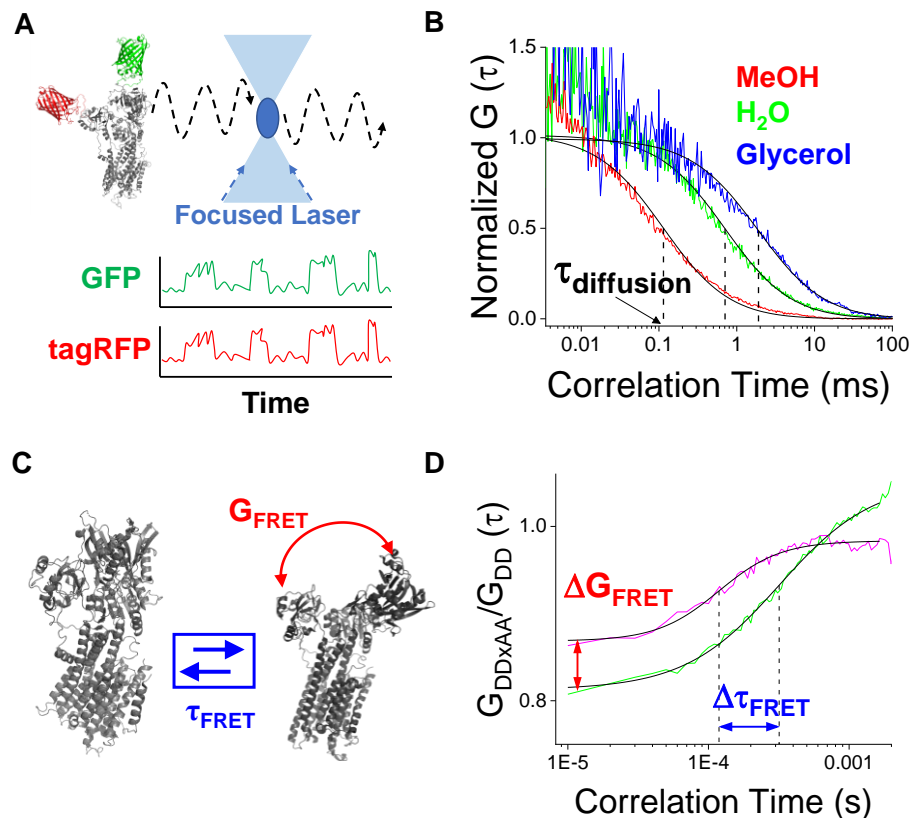


Figure 7. FCS and FCCS Measurements. **A**, Schematic diagram showing measurements of 2-color SERCA diffusing through a confocal volume. **B**, Autocorrelation curves reveal how the diffusion time (τ) of Rhodamine B becomes faster in MeOH and slower in 40% glycerol relative to water. **C**, Schematic diagram showing dynamic parameters of SERCA headpiece motions, τ_{FRET} and G_{FRET} , measured by FCCS. **D**, FCCS data derived from a simulation of 2-color SERCA in SimFCS. The data show how the parameters, τ_{FRET} and G_{FRET} , change when 2-color SERCA is under conditions with larger, slower molecular motions (*green*) compared to smaller, faster molecular motions (*pink*).

Specifically, a sigmoidal fit of the data reveals the G_{FRET} , which is indicative of the relative amplitude of the headpiece motions, and the τ_{FRET} , which relates to the relative

rate of the motions (Fig. 7C). These data were compared to FCS-FRET results from simulations conducted in SimFCS software (Fig. 7D) (Laboratory for Fluorescence Dynamics, UC Irvine).

Molecular Dynamics Simulations

Molecular dynamics (MD) simulations of SERCA in complex with ATP and PLB were done in collaboration with the Espinoza-Fonseca lab at University of Michigan. Briefly, the model of SERCA alone was based on the crystal structure of SERCA in a Mg²⁺-bound E1 state (PDB: 3W5B) (2) and an atomic-level model of the full-length PLB bound to SERCA that was previously developed by the Espinoza-Fonseca lab (116) was used for simulations with PLB. The complexes were inserted into a pre-equilibrated bilayer of 1-palmitoyl-2-oleoyl-sn-glycero-3-phosphocholine (POPC). For simulations of SERCA with ATP-bound, ATP was docked into its binding site and equilibrated. Once equilibrated, these models were used as a starting point for 3 independent trajectories each approximately 1 μ s in length for each complex for a total of 11.6 μ s.

Statistical Analysis

Data are presented as the mean \pm standard error (SE) unless otherwise stated. All statistical tests were performed using OriginPro 2021 (OriginLabs). For comparisons between two groups, a two-tailed student's t-test was performed. For comparisons between three or more groups, a one- or two-way ANOVA was performed depending on the number of independent variables that were manipulated. Differences between groups analyzed by ANOVA were determined by either Tukey's (parametric) or Dunn-Sidak's (nonparametric) post-hoc test depending on if sampling and variance were

determined to be equal among groups. A probability (p) value of <0.05 was considered significant. Specific values are provided in figure panels, figure legends, and text.

CHAPTER FOUR

INHIBITORY AND STIMULATORY MICROPEPTIDES PREFERENTIALLY BIND TO DIFFERENT CONFORMATIONS OF THE CARDIAC CALCIUM PUMP

Results

SERCA Affinity for PLB and DWORF is Dependent on Ca²⁺ Pump Conformation

Our lab has previously demonstrated that PLB-SERCA binding affinity is reduced in response to a sustained elevation of intracellular Ca²⁺, whereas the DWORF-SERCA interaction is more stable with elevated [Ca²⁺] (5, 84). This reciprocal Ca²⁺-dependence prompted the hypothesis that PLB and DWORF may preferentially bind to different intermediate conformations of the SERCA enzymatic cycle. The SERCA enzymatic cycle (47) is represented in Fig. 8A. At basal Ca²⁺ (low nM), SERCA predominantly resides in the ATP bound state, E1-ATP (59) (Fig. 8A, *blue box*), waiting for Ca²⁺ to bind. During intracellular Ca²⁺ elevations, SERCA samples all the intermediate states of the Ca²⁺ transport cycle, but these states are not all equally populated during systole. Rather, there is relative accumulation in the transition from the E1PCa to E2P state, a rate-limiting step of the enzymatic cycle (49, 62) (*See Chapter 2, Fig. 3*). The E1PCa state is outlined with a red box in Fig. 8A.

To determine the relative affinity of both micropeptides for these and other key SERCA enzymatic states, we transfected HEK-293 cells with Cerulean (Cer)-labeled SERCA2a (FRET donor) and yellow fluorescent protein (YFP)-labeled PLB (FRET acceptor) and quantified the interaction of these proteins using acceptor sensitization

FRET microscopy. Protein expression levels in membrane fractions prepared from HEK cells were comparable to protein concentrations in membranes prepared from human heart tissues (Appendix Fig. B.1). To control the conformational poise of SERCA, cells were permeabilized with 0.05 mg/mL saponin in bath solutions appropriate for stabilization of the transporter in various conformations (See Chapter 3 and Appendix Fig. B.2). The affinity of the PLB-SERCA interaction was quantified by measuring FRET with automated fluorescence microscopy, as previously described (117, 118).

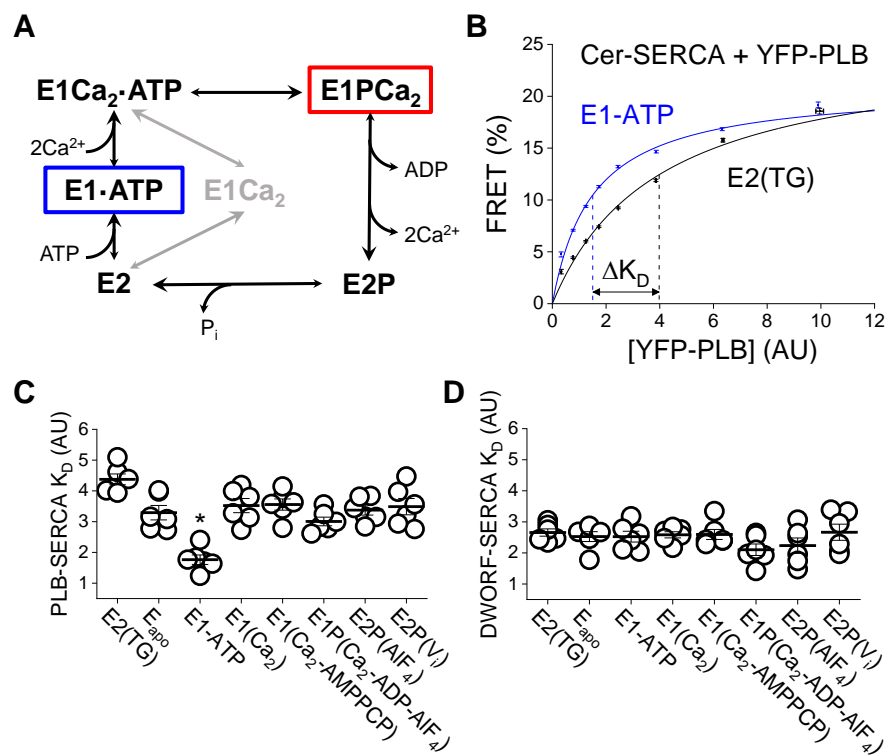


Figure 8. Inhibitory and Stimulatory Micropeptides Preferentially Bind Different SERCA Conformations. **A**, A simplified Post-Albers scheme of the SERCA enzymatic cycle, highlighting states that predominate at low (*blue*) and high (*red*) intracellular [Ca²⁺]. **B**, FRET-based binding curves displaying a shifted dissociation constant (K_D) of PLB-SERCA binding between the ATP-bound (*blue*) and TG-bound (*black*) states of SERCA. **C-D**, Apparent K_D s of PLB or DWORF binding to different SERCA enzymatic states of the catalytic cycle as in panel A with lines representing mean \pm SEM ($n = 6$). Ligands used to stabilize each state are shown in parentheses. Differences in micropeptide K_D s between SERCA states were analyzed by one-way ANOVA with Tukey's post hoc ($*p < 0.05$).

FRET was low in cells with low fluorescence (low protein expression), increasing to a maximum in the brightest cells (high protein expression), yielding a FRET based “binding curve” (Fig. 8B). A hyperbolic fit to the data yielded the maximal FRET efficiency at high protein concentration or FRET_{max} (representing the intrinsic FRET of the bound PLB-SERCA complex) and the apparent dissociation constant (K_D), the protein concentration that yields half-maximal FRET efficiency. The K_D value is inversely related to the affinity of the PLB-SERCA complex. Fig. 8B shows the conditions that yielded the greatest difference in relative K_D for the PLB regulatory complex. PLB bound to the E1-ATP state of SERCA is obtained with a solution containing 3 mM ATP and low Ca^{2+} , and represents the prevailing conformation in resting (diastolic) conditions. Addition of thapsigargin (TG) resulted in a significant right-shift of the binding curve ($p = 8 \times 10^{-3}$) (*Appendix B*, Table B.1), indicating a decrease in PLB-SERCA affinity. Reduced affinity of PLB for TG-inhibited SERCA is consistent with previous observations from our lab (119) and others (82).

The summary of fitting of binding curves obtained from 6 independent transfections for each of 8 conditions is shown in Fig. 8C-D and Table 1 (*Appendix B*, Fig. B.3 and B.4). We observed especially avid binding of PLB to the E1-ATP state, which may indicate stabilization of that conformation of SERCA. This is the state that most SERCA pumps are in during the diastolic phase of the cardiac cycle when cytoplasmic Ca^{2+} is low, the muscle is relaxed, and the heart is filling with blood. The affinity of PLB for this state was not altered over a range of pH from 6-8 (*Appendix B*, Fig. B.5), indicating no preference for “E2” or “E1” transmembrane domain conformations stabilized in acidic or alkaline pH respectively (6, 120).

Table 1. Acceptor-Sensitization FRET Curve Parameters. Data are reported as mean \pm SEM ($n = 6$). Differences were determined by one-way ANOVA with Dunn's post hoc ($*p < 0.05$, See Appendix B, Table B.1 for complete statistical analysis).

Enzymatic State	Stabilizing Ligand(s)	PLB-SERCA		DWORF-SERCA	
		K_D (AU)	FRET _{max} (%)	K_D (AU)	FRET _{max} (%)
E2	TG	4.4 \pm 0.2	26 \pm 0.8	2.7 \pm 0.1	28 \pm 0.5
E_{apo}		3.3 \pm 0.2	25 \pm 0.9	2.5 \pm 0.2	29 \pm 1.1
E1-ATP	ATP	1.8 \pm 0.2*	22 \pm 0.3	2.5 \pm 0.2	29 \pm 1.4
E1	Ca ²⁺	3.5 \pm 0.2	26 \pm 0.9	2.6 \pm 0.1	29 \pm 0.7
E1	Ca ²⁺ -AMPPCP	3.6 \pm 0.2	26 \pm 0.8	2.6 \pm 0.2	29 \pm 1.6
E1P	Ca ²⁺ -ADP-AIF ₄	3.0 \pm 0.1	22 \pm 0.9	2.1 \pm 0.2	25 \pm 0.8
E2P	AIF ₄	3.4 \pm 0.2	24 \pm 0.9	2.2 \pm 0.3	27 \pm 1.0
E2P	V _i	3.5 \pm 0.3	26 \pm 0.8	2.7 \pm 0.3	31 \pm 2.1

In contrast to PLB, DWORF showed a much flatter affinity profile across SERCA enzymatic states (Fig. 8D). We noted slightly lower K_D values for E1PCa and E2P states. The population of SERCA pumps increasingly accumulates in these states during the systolic phase of the cardiac cycle when cytoplasmic Ca²⁺ is elevated and the heart is contracting to eject blood. DWORF may have a preference for those conformations, though the difference was not statistically significant by one-way ANOVA (Table 1). We did resolve statistically significant differences in PLB-SERCA and DWORF-SERCA affinities in a simpler comparison of affinities in ATP-containing solutions: low Ca²⁺ “relaxing solution” vs. a high Ca²⁺ solution that induced enzymatic cycling of SERCA (see Chapter 3). In these physiological buffers mimicking diastole vs. systole, respectively, we observed reciprocal Ca²⁺-dependent binding affinity for PLB-SERCA vs. DWORF-SERCA (Fig. 9), consistent with our previous study (5).

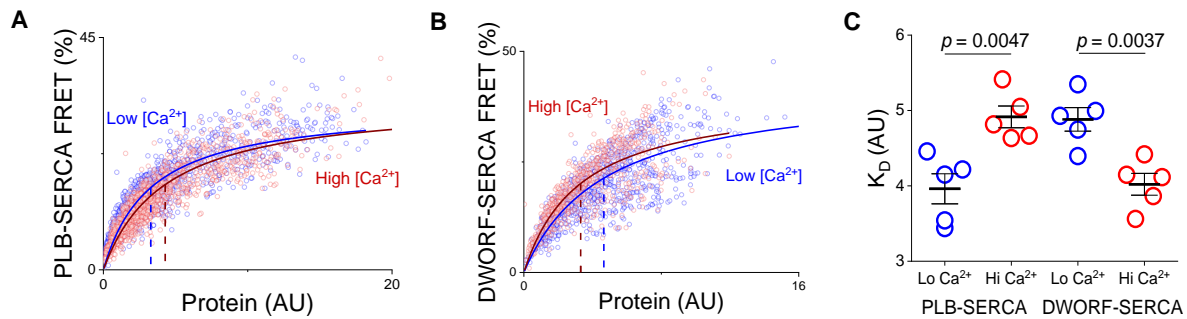


Figure 9. SERCA-Micropeptide Interactions are Ca^{2+} Sensitive. **A,** Representative PLB-SERCA binding curves obtained in low (*blue*, ~ 1 nM free Ca^{2+}) and high (*red*, ~ 2 μ M free Ca^{2+}) cytoplasm conditions. **B**, Representative DWORF-SERCA binding curves obtained in low (*blue*, ~ 1 nM free Ca^{2+}) and high (*red*, ~ 2 μ M free Ca^{2+}) cytoplasm conditions. **C**, Apparent K_D s of PLB and DWORF for SERCA in ATP-containing solutions with low (*blue*) and high (*red*) concentrations of intracellular Ca^{2+} with lines representing mean \pm SEM ($n = 5$). Differences in K_D evaluated by Student's t test.

Taken together, these data indicate that PLB and DWORF prefer to bind different SERCA conformations corresponding to different enzymatic intermediate states of the transport cycle. This change in binding affinity suggests a potential for these regulators to dynamically exchange from SERCA during intracellular Ca^{2+} elevations (Fig. 10A). To evaluate the responsiveness of PLB-SERCA binding equilibria to transient intracellular Ca^{2+} elevations, we exploited a cardiomimetic model system described previously (121). Briefly, HEK-293 cells expressing exogenous RyR and SERCA2a display spontaneous ER Ca^{2+} release and re-uptake events. These Ca^{2+} transients were detected by confocal microscopy as an increase in the relative fluorescence of the cytoplasmic Ca^{2+} indicator dye, X-Rhod-1 (Fig. 10B,C, *black*). The PLB-SERCA binding equilibria was monitored by FRET ratio (YFP/mCer) measurements between mCer-SERCA and YFP-PLB fluorescent constructs. In some cells, these intracellular Ca^{2+} elevations coincided with small decreases in PLB-SERCA FRET (Fig. 10B, *blue*), consistent with the small decrease in PLB-SERCA binding affinity at high Ca^{2+} observed in equilibrium

experiments (Fig. 9A). Indeed, we were previously unable to detect a change in PLB-SERCA FRET in response to single Ca^{2+} transients in electrically paced cardiac myocytes, only observing a modest decrease in PLB-SERCA FRET in response to a series of rapidly paced Ca^{2+} elevations (84). However, in HEK cells the Ca^{2+} elevations were prolonged (increasing time for quantification), expression of endogenous PLB/SERCA was very low (reducing competing, non-FRET interactions), and the cells are noncontractile (eliminating motion artifacts). These advantages enabled detection of small equilibrium shifts in PLB-SERCA binding in this model system.

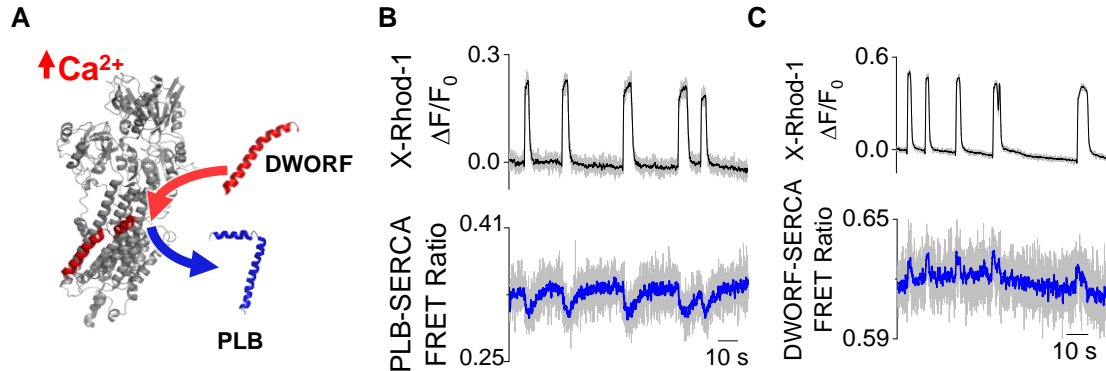


Figure 10. Dynamic Exchange of PLB and DWORF from SERCA during Intracellular Ca^{2+} Elevations. **A**, A schematic diagram of shifts in PLB and DWORF binding with SERCA in response to cytoplasmic Ca^{2+} elevations. **B**, Confocal microscopy quantification of intracellular Ca^{2+} measured by X-Rhod-1 fluorescence (gray raw data, with black smoothed trendline) with simultaneous measurement of changes in PLB-SERCA FRET (YFP/Cer ratio) (gray raw data, with blue smoothed trendline). **C**, Confocal microscopy quantification of intracellular Ca^{2+} measured by X-Rhod-1 fluorescence (gray raw data, with black smoothed trendline) with simultaneous measurement of changes in DWORF-SERCA FRET (YFP/Cer ratio) (gray raw data, with blue smoothed trendline).

Next, we monitored the DWORF-SERCA FRET binding equilibria responding to cellular Ca^{2+} elevations. Although these changes were even smaller than those observed for PLB-SERCA binding, we were able to detect modest increases in DWORF-SERCA

FRET during Ca^{2+} transients (Fig. 10C, *blue*) consistent with enhanced DWORF-SERCA binding affinity at elevated cytoplasmic Ca^{2+} (Fig. 9B).

Taken together, these data indicate that PLB and DWORF binding equilibria with SERCA are dynamically responsive to Ca^{2+} signals on a timescale comparable to that of the human heartbeat. This suggests that regulatory control of SERCA may shift on a beat-to-beat basis such that PLB regulatory binding decreases (relieving inhibition) and DWORF binding increases (providing increased activation of SERCA) during each systolic increase in intracellular Ca^{2+} . Physiologically, this would provide a mechanism to increase SERCA activity as cytoplasmic Ca^{2+} rises and Ca^{2+} transport by SERCA becomes most needed.

Ca^{2+} -Dependent SERCA-Micropeptide Exchange Kinetics

To examine how the kinetics of cellular Ca^{2+} signaling determines SERCA-micropeptide binding dynamics, we quantified the rates of the changing FRET and $[\text{Ca}^{2+}]$ signals. Specifically, exponential decay fitting of these changes revealed characteristic time constants (τ) for each process. Analysis of the Ca^{2+} release process (Fig. 11A) showed that DWORF-SERCA binding occurred with a time course that was similar to the rate of rise of Ca^{2+} ($\tau = 0.22 \pm 0.03$ s and 0.21 ± 0.03 s, respectively) (Fig. 11B). PLB-SERCA unbinding was slower ($\tau = 0.74 \pm 0.14$ s), lagging ~ 0.5 s behind Ca^{2+} release ($p = 4 \times 10^{-8}$). In addition, we evaluated how changes in PLB-SERCA binding impacted the PLB monomer/pentamer equilibrium by measuring intrapentameric FRET between mCer-PLB and YFP-PLB. Interestingly, PLB-PLB FRET increased dynamically during Ca^{2+} elevations (Fig. 11D). The inverse changes in PLB-SERCA FRET (Fig. 10B) and PLB-PLB FRET (Fig. 11D) suggest that as PLB monomers are displaced from

SERCA, they are rapidly incorporated into PLB pentamers. The time course of PLB-PLB binding lagged slightly behind Ca^{2+} release ($\tau = 0.59 \pm 0.04$ s, $p = 2 \times 10^{-4}$) (Fig. 11E). This delay was similar to that observed for PLB-SERCA unbinding (Fig. 11F), suggesting PLB-SERCA unbinding may be rate limiting for subsequent PLB oligomerization during Ca^{2+} elevations. The kinetics of SERCA–micropeptide binding dynamics during Ca^{2+} release are summarized in Appendix B Fig. B.6 and Tables B.2–B.4.

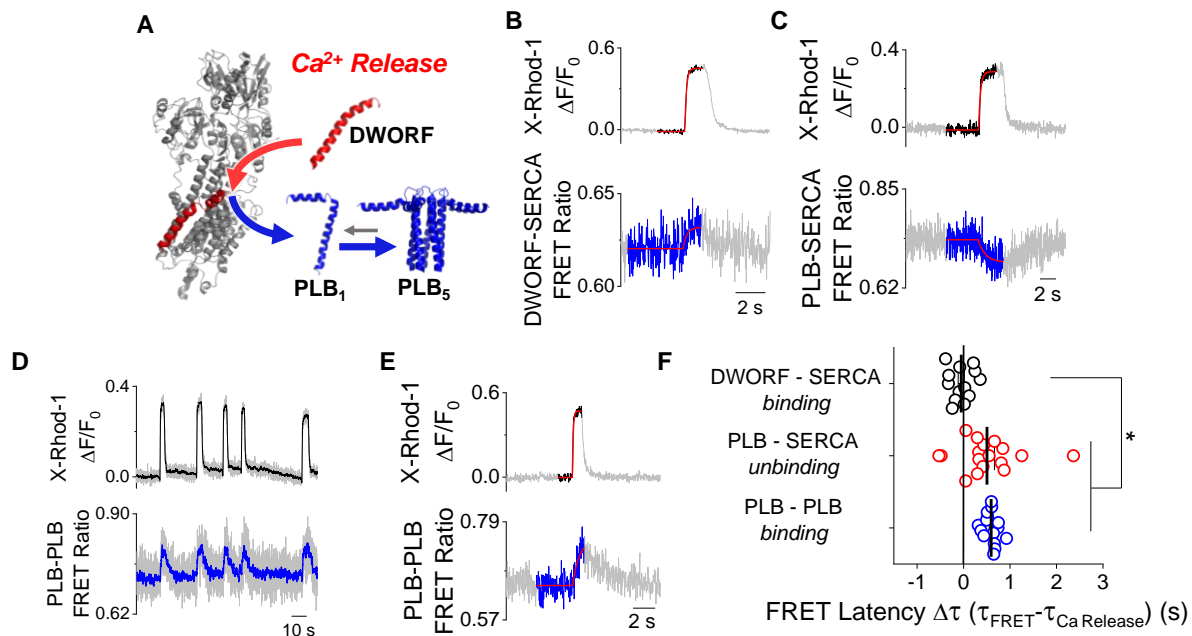


Figure 11. Kinetics of SERCA-Micropeptide Binding Processes during Ca^{2+} Release. **A**, A schematic diagram of shifts in PLB and DWORF binding equilibria during Ca^{2+} release. **B**, Representative single exponential decay fit of the kinetics of DWORF–SERCA binding during Ca^{2+} release. **C**, Kinetics of PLB–SERCA unbinding during Ca^{2+} release. **D**, Confocal microscopy quantification of intracellular Ca^{2+} measured by X-Rhod-1 fluorescence (gray raw data, with black smoothed trendline) with simultaneous measurement of changes in PLB–PLB FRET (YFP/Cer ratio) (gray raw data, with blue smoothed trendline). **E**, Kinetics of PLB–PLB binding during Ca^{2+} release. **F**, The latency of FRET ratio changes compared to Ca^{2+} release with lines representing mean \pm SEM. Differences determined by one-way ANOVA with Dunn’s post hoc test (* $p < 0.05$, see Appendix B, Table B.3 for complete statistical analysis).

Next, we examined changes in SERCA-micropeptide binding as Ca^{2+} declined back to baseline during Ca^{2+} uptake (Fig. 12A). DWORF dissociated rapidly from SERCA, as measured by the decrease in the DWORF-SERCA FRET ratio back to baseline (Fig. 12B). This unbinding process occurred with a τ of 1.2 ± 0.4 s, similar to the time course of Ca^{2+} uptake. However, PLB-SERCA reassociation displayed a significant lag time compared to the relaxation of the Ca^{2+} transient, with FRET continuing to increase back toward a maximum for several seconds after Ca^{2+} had already stabilized to a basal level (Fig. 12C). The τ of PLB-SERCA rebinding was 4.9 ± 0.6 s, which was significantly slower than the time course of Ca^{2+} uptake ($\tau = 1.6 \pm 0.2$ s, $p = 2 \times 10^{-8}$).

To understand the unexpectedly slow rate of PLB-SERCA rebinding, we considered whether the rate of PLB-SERCA recovery could be limited by slow dissociation of PLB monomers from PLB pentamers. Indeed, our lab had previously shown that the exchange time of PLB from pentamers was significantly slower than the rate of exchange from its regulatory complex with SERCA (96). Consistent with this hypothesis, PLB-PLB FRET relaxation (unbinding of PLB monomers from pentamers) displayed a slow time course ($\tau = 5.2 \pm 0.8$ s) (Fig. 12D) that closely matched the slow PLB-SERCA reassociation ($\tau = 4.9 \pm 0.6$ s) (Fig. 12E). Our hypothesis was further supported by the observation that destabilization of the PLB pentamer by mutagenesis (PLB-AFA) (122) accelerated the PLB-SERCA rebinding time ($\tau = 2.5 \pm 0.5$ s, $p = 8 \times 10^{-3}$), such that the FRET changes no longer lagged behind the Ca^{2+} transient decay (Fig. 12E and Appendix Fig. B.7).

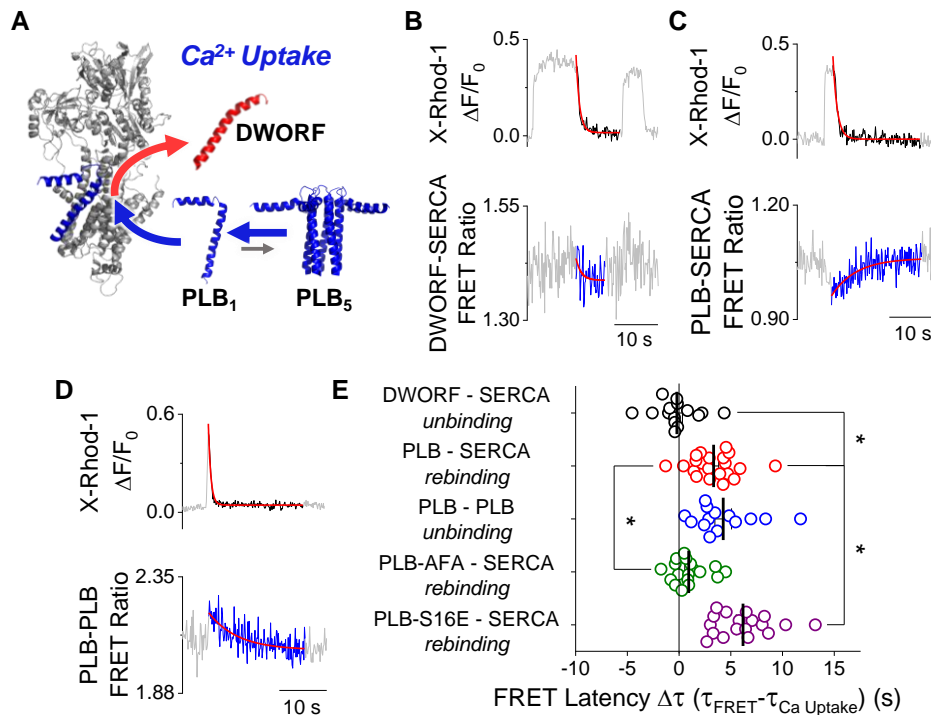


Figure 12. Kinetics of SERCA-Micropeptide Binding Processes during Ca^{2+} Uptake. **A**, A schematic diagram of shifts PLB and DWORF binding equilibria during Ca^{2+} uptake. **B**, Representative single exponential decay fit of the kinetics of DWORF-SERCA unbinding during Ca^{2+} uptake. **C**, Kinetics of PLB-SERCA rebinding during Ca^{2+} uptake. **D**, Kinetics of PLB-PLB binding during Ca^{2+} release. **E**, The latency of FRET ratio changes compared to Ca^{2+} uptake with lines representing mean \pm SEM. Differences determined by one-way ANOVA with Dunn's post hoc test ($*p < 0.05$, see Appendix B, Table B.7 for complete statistical analysis).

We also examined how pentamer dissociation kinetics could be physiologically tuned to control the PLB-SERCA reassociation rate. Equilibrium measurements of PLB oligomerization have previously shown that PLB pentamers are stabilized by PKA phosphorylation of serine 16 of PLB (94, 95, 123), which occurs as an outcome of adrenergic signaling during physiological stress. Here, we found that stabilization of pentameric interactions using a phosphomimetic S16E mutation further slowed the rate of PLB-SERCA reassociation ($\tau = 8.6 \pm 0.7$ s, $p = 2 \times 10^{-6}$) (Fig. 12E and Appendix Fig. B.8). The kinetics of SERCA-micropeptide binding dynamics during Ca^{2+} uptake are

summarized in Appendix Fig. B.9 and Table B.5–B.7. Overall, the results support the hypothesis that PLB pentamers delay reassociation of the dynamic fraction of PLB with SERCA after Ca^{2+} elevations, and this mechanism is physiologically tuned under the control of adrenergic signaling.

Modeling the Redistribution of PLB and DWORF Regulatory Complexes

To interpret our FRET-based measurements of SERCA–micropeptide binding dynamics, we developed a computational model to integrate the measured rates of the dynamic interactions of PLB and DWORF with SERCA in the context of the human cardiac cycle. Using this model, we simulated the dynamic redistribution of these regulatory complexes between systole and diastole, or on a longer timescale, between rest and exercise. The model describes the kinetics of these regulatory interactions with a set of numerically solved ordinary differential equations (see Supplemental Methods). A genetic algorithm was used to fit mean rate constants for the forward and reverse reactions in the model from experimentally measured FRET data as previously described (40). For simplicity, we considered the population of SERCA pumps to be distributed between two ensembles of pump enzymatic states, representing the “diastolic” condition (Ca-free) and the “systolic” condition (Ca-bound), as diagrammed in Figure 13A. The relative population of these two ensemble states is dependent on the relative concentration of Ca^{2+} , as quantified by confocal microscopy experiments. Monomeric PLB (PLB_1) can bind either the Ca-free or Ca-bound ensemble of SERCA (84) but with higher affinity for the Ca-free population (Fig. 8C and 9A). The relative affinity of PLB for SERCA was constrained to be twofold higher for Ca-free versus Ca-bound ensembles, as determined experimentally from FRET-binding curves (Fig. 8C).

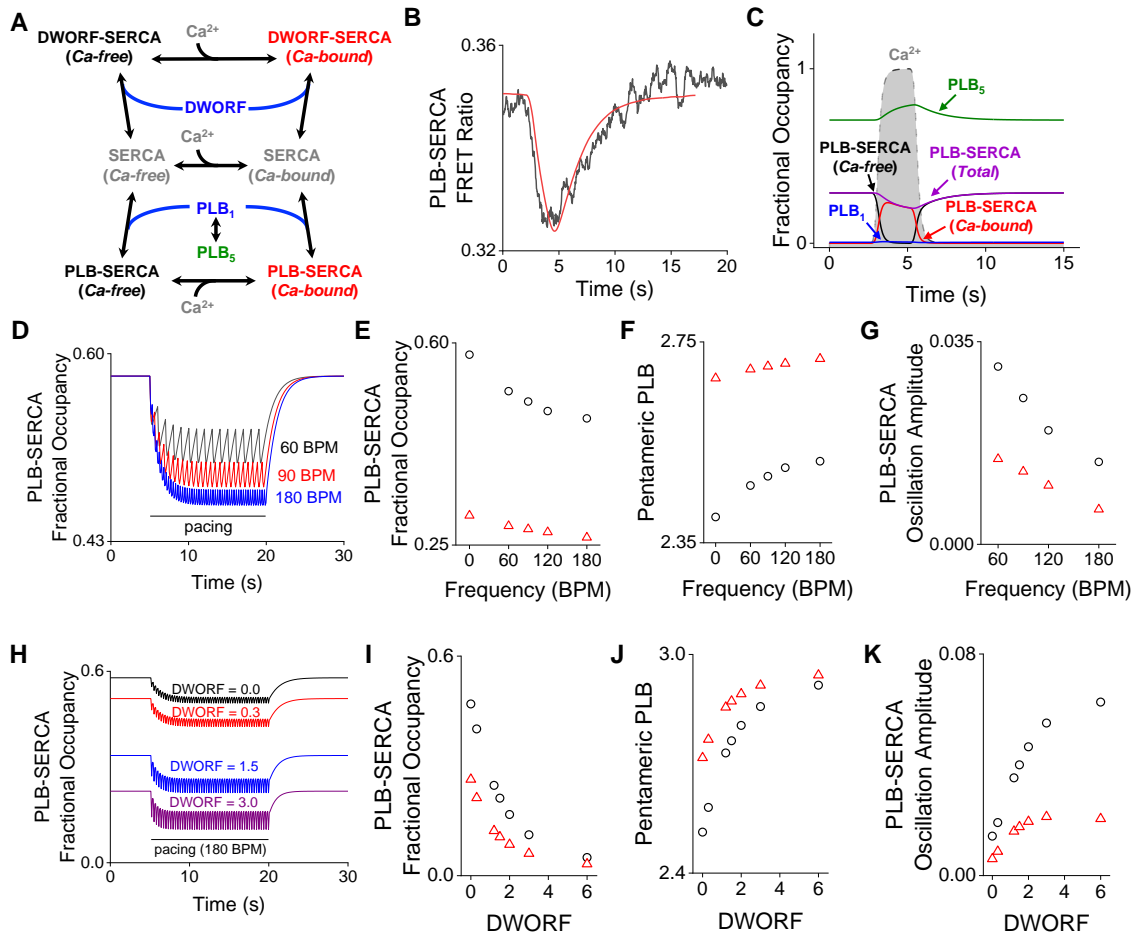


Figure 13. A Computational Model Simulates the Dynamics of PLB and DWORF Interactions with SERCA. **A**, A simplified diagram of modeled regulatory interactions. **B**, A fit of the model to a representative FRET change measured by confocal microscopy. **C**, A simulation of changes in the populations of regulatory species during a Ca²⁺ elevation, where relative amounts of SERCA and PLB are equal. **D**, A simulation of the effect of cardiac pacing on PLB-SERCA at three heart rates (beats per min, BPM) **E**, Increasing pacing frequency modestly decreased PLB-SERCA binding. **F**, Increasing pacing frequency increased PLB oligomerization. **G**, PLB-SERCA oscillation amplitude decreased with faster pacing. For D-G, the ratio of SERCA:PLB was 1:3. Black circles represent the results of the model of the normal, nonfailing heart. Red triangles represent adjustment of the model to simulate heart failure. **H**, A simulation of the effect of increasing DWORF expression relative to SERCA on PLB-SERCA binding. **I**, Increasing DWORF resulted in a decrease in the equilibrium level of PLB-SERCA. **J**, Increasing DWORF increased PLB oligomerization. **K**, Increasing DWORF relative to SERCA resulted in larger oscillations in PLB-SERCA binding. For H-K, the ratio of SERCA:PLB was 1:3 and pacing rate was 180 BPM. Black circles represent the results of the model of the normal, nonfailing heart. Red triangles represent adjustment of the model to simulate heart failure.

Monomeric PLB (PLB₁) is also in equilibrium with the pentameric population (PLB₅). The relative affinity of DWORF for SERCA was constrained to increase by 25% between Ca-free and Ca-bound ensembles, consistent with FRET measurements (Fig. 8D) (5). The computed kinetic parameters are provided in Appendix B (Fig. B.10).

Dynamic Responses of SERCA-Micropeptide Binding Equilibria to Ca²⁺

Transients

The computational model provided good descriptions of data from physical experiments showing time-dependent changes in PLB–SERCA FRET and cytoplasmic Ca²⁺ (measured simultaneously). Figure 13B provides a best-fit model prediction of the FRET compared to a representative experimental measurement. The model captured the rapid reduction of FRET with the rise of the Ca²⁺ transient. The decrease in PLB–SERCA is followed by a slower restoration of the FRET as Ca²⁺ returns to baseline. The similarity of the predicted and experimentally measured FRET data suggests that the model appropriately represents key aspects of PLB–SERCA binding dynamics. Using these fit parameter values, we simulated the time-dependent changes in PLB–SERCA and PLB–PLB binding dynamics that we observed in HEK cells. Importantly, we observed that a majority of the PLB–SERCA regulatory complexes remained intact (Fig. 13C, *purple*) during a Ca²⁺ elevation (Fig. 13C, *gray shaded region*), consistent with the “subunit model” (124). Thus, PLB can remain bound to SERCA when SERCA is bound to Ca²⁺; this Ca²⁺-bound PLB–SERCA fraction is highlighted in Figure 13C (*red*). However, a fraction of the population of PLB–SERCA dissociated during a Ca²⁺ transient (Fig. 13C, *purple*). This fraction comprised ~30% of PLB–SERCA complexes under these simulation conditions. This shift impacted the PLB monomer/pentamer

equilibrium (Fig. 13C, *blue/green*). Expectedly, there was very little observed change in the small population of PLB monomers, as the dynamic fraction was quickly incorporated into pentamers. These reciprocal shifts are the cause of the transient decrease in SERCA–PLB FRET and increase in PLB–PLB FRET observed by confocal microscopy (Fig. 12C,D).

Next, we simulated the shorter, faster Ca^{2+} transients observed in the heart, pacing at a range of frequencies from 60 to 180 beats per minute to investigate regulatory dynamics under conditions of rest, moderate exercise, and intense exercise. For these physiological simulations, the ratio of SERCA:PLB was increasing pacing frequency progressively decreased PLB–SERCA binding (Fig. 13D,E, *black circles*) and increased accumulation of PLB in pentamers (Fig. 13F, *black circles*). The systole–diastole difference in PLB–SERCA binding was small. This oscillation became even smaller with increasing pacing frequency (Fig. 13D,G, *black circles*), as the shifts in binding equilibria began to lag behind the rapid Ca^{2+} changes. These results suggest that the exchange dynamics of PLB may impact adaptive SERCA regulation between resting and exercising heart rates.

To assess how PLB–SERCA binding dynamics may be altered in disease, we modified the model conditions to reflect changes observed in heart failure. Specifically, the SERCA population was reduced by 40% (34) and diastolic Ca^{2+} was increased by 50% (40). The heart failure condition is shown in Figure 13 as red triangles. As expected, the heart failure condition decreased the population of PLB bound to SERCA at equilibrium (Fig. 13E), decreased PLB–SERCA oscillation amplitude (Fig. 13G), and blunted the responsiveness of these parameters to increasing heart rates (Fig. 13, E–

G). This suggests frequency-dependent changes in PLB inhibition may be reduced in heart failure.

Introduction of DWORF–SERCA interactions to the model yielded the expected effect of competition between DWORF and PLB for SERCA binding (Fig. 13A).

Increasing the amount of DWORF relative to PLB decreased PLB–SERCA binding (Fig. 13H,I, *black circles*) and increased PLB oligomerization (Fig. 13J, *black circles*).

DWORF competes potently with PLB even at low stoichiometry because oligomerization of PLB reduces the effective concentration of the active monomeric species.

Interestingly, the Ca^{2+} -dependent increase in DWORF affinity for SERCA exaggerated the oscillations in PLB–SERCA binding during pacing (Fig. 13K, *black circles*). That is, during Ca^{2+} elevations DWORF (which binds SERCA better at high Ca^{2+}) increasingly displaced PLB (which binds SERCA better at low Ca^{2+}).

Under conditions representing heart failure (decreased SERCA expression, increased diastolic Ca^{2+}) (Fig. 13I–K, *red triangles*), there was decreased formation of the PLB–SERCA complex (Fig. 31E), and therefore, the effect of DWORF competition was blunted (Fig. 13I). Moreover, since changes in PLB–SERCA binding between systole and diastole were smaller in heart failure, the ability of DWORF to exaggerate this change through Ca^{2+} -dependent competition was also decreased (Fig. 13K). These results suggest that the impact of DWORF on PLB–SERCA binding dynamics may be reduced in heart failure.

Discussion

Differential Ca^{2+} -Dependence of Micropeptide Affinity for SERCA

The principal finding of the present study is that PLB and DWORF preferentially

bind to different conformations of SERCA (Fig. 8C, D), and this is the underlying cause of the reciprocal Ca^{2+} -dependent affinities of these micropeptides (Fig. 9) (5). The FRET-based binding assay showed that PLB has the highest affinity for the E1-ATP state (Fig. 8C), which is the predominant state at resting Ca^{2+} (Fig. 8A, *blue box*). In contrast, DWORF shows a much flatter SERCA-binding profile, with more avid binding to E1P and E2P states (Fig. 8D). Much of the SERCA population accumulates in these states when cytoplasmic Ca^{2+} is elevated. This accumulation occurs because of rate-limiting, slow steps in the SERCA enzymatic cycle (49, 62), which cause rapidly cycling pumps to build up in “traffic jams”, particularly in the transition from E1P to E2P (Fig. 8A, *red box*). Figure 10 shows how differential binding of micropeptides leads to exchange of a dynamic fraction of PLB and DWORF from the binding site on SERCA during intracellular Ca^{2+} elevations. In high Ca^{2+} (Fig. 11A), DWORF increasingly outcompetes PLB, displacing a fraction of monomeric PLB (“PLB₁”), which is increasingly incorporated into PLB pentamers (“PLB₅”). Conversely, in low Ca^{2+} (Fig. 12A), DWORF binding is decreased, and PLB monomers increasingly bind to SERCA because the pump accumulates in the E1-ATP state that PLB prefers. This recovery process is rate-limited by the slow dissociation of monomeric PLB from pentamers (Fig. 12D).

We propose that differential Ca^{2+} -dependence is the key determinant of whether a micropeptide is inhibitory or stimulatory for SERCA function. In particular, micropeptide-SERCA binding affinity may be taken as an index of the relative energetics of the regulatory complex, much as melting temperature may be quantified as a proxy for the stability of a protein-protein complex (125). Thus, avid PLB binding to the E1-ATP structure is expected to stabilize that complex and favor the population of

that state of SERCA. The functional consequence of stabilizing this state is to slow the subsequent Ca^{2+} -binding step in the enzymatic cycle. This may account for the principal inhibitory effects of PLB: reducing the apparent Ca^{2+} affinity of the pump and slowing pump turnover (11). Moreover, we propose that while PLB binding to E1-ATP deepens a depression in the energy landscape, DWORF reduces the height of a peak, lowering an energy barrier by stabilizing E1P/E2P states. Increasing pump flux through this rate limiting step enhances enzyme turnover when Ca^{2+} is high (5).

In addition, the dynamics of PLB and DWORF binding and unbinding from SERCA described here have important functional implications. Reciprocal binding may be important for reacting to transient Ca^{2+} changes during the cardiac cycle or, on a longer timescale, responding to adrenergic signaling and changes in pacing frequency during exercise. The present data provide insight into Ca^{2+} transport regulation on both timescales, as discussed below.

Functional Implications of Micropeptide Exchange During the Cardiac Cycle

The change in PLB-SERCA binding with Ca^{2+} is only ~2 fold, so PLB-SERCA complexes do not completely dissociate during systole (Fig. 13D) (5, 119). However, cardiac Ca^{2+} elevations simultaneously reduce PLB binding affinity and favor DWORF binding, so a fraction of the population of these micropeptides must exchange from SERCA during each Ca^{2+} transient. Our computational model showed that the expected functional impact of this exchange is to exaggerate the intrinsic response of SERCA to changing Ca^{2+} . That is, during diastole (cardiac relaxation) SERCA activity is already low because Ca^{2+} is low. SERCA is further inhibited in diastole by an increase in the fraction of pumps that bind PLB (Fig. 10B). Then, during systole (cardiac contraction),

Ca²⁺ is high, supporting high SERCA activity. This high SERCA activity is further enhanced by increased DWORF binding (Fig. 10C), which increasingly displaces PLB and directly stimulates SERCA maximal activity (5, 38, 100, 101, 126-128). Together, low Ca²⁺ inhibition and high Ca²⁺ stimulation should enhance the apparent cooperativity of the Ca²⁺ response, which would benefit cardiac function by conserving ATP consumption until Ca²⁺ transport is most efficient and most needed. Thus, competitive binding of SERCA by DWORF decreases both the basal level of PLB-SERCA binding as previously proposed (128) and also increases the amplitude of the oscillations in the population of the PLB-SERCA complex (Fig. 13I-K). The dose-dependence of these effects revealed in the computational model may provide guidance for future DWORF-based gene therapy approaches (38, 100, 101).

The Function of the PLB Pentamer Kinetic Trap in Rest and Exercise

The observations presented here also have implications for the enhancement of cardiac function during exercise. PLB dissociation from pentamers is slow ($\tau \sim 5$ s) (Fig. 12D), a noteworthy finding since this is significantly slower than the cardiac cycle. Even at a resting heart rate, a one second interval between beats would not be sufficient time for the equilibrium to fully relax between systole and diastole. Therefore, Ca²⁺ signals must also integrate over a longer timescale, such as between rest and exercise. This is visualized in our computational model, which showed increasing accumulation of PLB in pentamers at faster heart rates at the expense of the population of PLB-SERCA (Fig. 13D-F). Such “kinetic trapping” of PLB in pentamers at faster heart rates is further increased by phosphorylation of PLB by PKA or CaMKII, which stabilizes the pentamer complex (94, 118, 123). These kinases are activated in exercise through adrenergic

signaling and prolonged Ca^{2+} elevation, respectively. The functional consequence of decreased SERCA inhibition by PLB is increased SR Ca^{2+} load and enhanced cardiac contractility. Thus, one may speculate that frequency-dependent accumulation of PLB in pentamers contributes to the Bowditch effect, a positive force-frequency relationship in which a faster heart rate causes more forceful contractions of the heart. The mechanism we propose may explain previous studies that showed the Bowditch effect was absent in PLB KO mice (87-89, 129). Moreover, simulations showed that under pathological conditions SERCA regulation is decreased and the frequency-dependence of that regulation is diminished (Fig. 13E-G, *red triangles*). This may explain why the Bowditch effect is blunted in patients with heart failure (130).

Summary and Future Directions

Dynamic changes in the competition of regulatory micropeptides on seconds and minutes timescales represents an important aspect of the responsiveness of SERCA regulation to Ca^{2+} transients. The present data clarify the role of the PLB pentamer as a phosphorylation-tunable kinetic trap that limits the rate of SERCA-rebinding by a dynamic fraction of PLB. Future studies will test the functional predictions derived from the present results: DWORF enhances the rate of the E1P to E2P transition of the SERCA enzymatic cycle; DWORF increases the size of the fraction of PLB that binds/unbinds SERCA with each Ca^{2+} elevation, exaggerating the SERCA inhibition/stimulation cycle; DWORF and PLB act in concert to increase the cooperativity of Ca^{2+} transport. Overall, the data suggest that dynamic competition of PLB and DWORF is an important determinant of cardiac function. More generally, the results may provide insight into the interplay of other tissue-specific micropeptide regulators of ion transporters.

CHAPTER FIVE

A DILATED CARDIOMYOPATHY MUTATION IN PHOSPHOLAMBAN, ARGININE 14 DELETION, INCREASES PHOSPHOLAMBAN PENTAMER STABILITY

Introduction

Dilated cardiomyopathy (DCM) is the most common disorder leading to heart failure, characterized by thinning of the ventricular wall and reduced pumping capacity of the heart (131, 132). As much as 50% of DCM is thought to be caused by genetically inherited mutations (131, 132). Although DCM mutations predominantly occur in proteins of the sarcomere, cytoskeleton, and nuclear membrane (131, 133, 134), a number of mutations have been identified in phospholamban (PLB), a transmembrane micropeptide that regulates intracellular Ca^{2+} transport by the sarcoplasmic reticulum (SR) Ca^{2+} ATPase (SERCA) (67, 135-138). SERCA sequesters cytosolic Ca^{2+} into the SR lumen to relax cardiac muscle between beats and prepares an intracellular Ca^{2+} store that is released into the cytoplasm to coordinate subsequent contractions of the heart (25). Dysregulation of SERCA Ca^{2+} transport is thought to cause maladaptive remodeling of intracellular Ca^{2+} signaling pathways that eventually lead to heart failure in patients (139, 140).

PLB is an SR-localized transmembrane peptide consisting of 52 amino acids that form 2 α -helical domains: a transmembrane helix that spans a single pass through the SR membrane and a cytoplasmic domain (1). PLB inhibits SERCA function through a direct protein-protein interaction between the transmembrane domain of PLB and a

regulatory cleft within SERCA's transmembrane domain (21, 72). The bioavailability of free PLB monomers that can regulate SERCA is dynamically controlled by PLB homo-oligomeric assembly into PLB pentamers (94-96, 141). Naturally occurring pathogenic mutations in the cytoplasmic domain of PLB have been shown to alter the stability of PLB pentamers, causing chronic dysregulation of SERCA leading to DCM (122, 142, 143). In particular, we previously showed an autosomal-dominant mutation of arginine 9 to a cysteine (R9C) causes disulfide bonds to form under conditions of oxidative stress (122). This crosslinking stabilizes PLB in pentamers, chronically reducing the population of active monomeric PLB available to regulate SERCA (122). Conversely, another autosomal dominant DCM mutation, which causes an in-frame deletion of arginine 14 (R14del), has been proposed to have the opposite effect. R14del-mutant PLB monomers were reported to destabilize PLB pentamers into smaller oligomer species when heterologously expressed with WT-PLB, with consequent super-inhibition of SERCA (135). However, several subsequent studies showed that the R14del mutation decreases the inhibitory potency of PLB (143-146), so the pathogenic mechanism of this mutation remains unclear.

Aside from a steady-state effect on the PLB monomer-pentamer equilibrium, DCM-associated mutations may also impact the heart's dynamic responsiveness to physiological stress such as exercise. Phosphorylation of PLB by PKA during adrenergic stimulation of the heart canonically relieves PLB inhibition, in part through stabilization of PLB pentamers (94, 95, 141), providing a mechanism to temporarily increase SERCA Ca^{2+} transport during exercise or other physiological stress. However, both R9C and R14del display reduced responsiveness to phosphorylation (122, 135,

142, 147, 148). In addition, we showed that temporal buffering of the concentration of PLB monomers by the pentamer controls the responsiveness of PLB regulation to changing heart rates (141). Specifically, we showed that a fraction of PLB unbinds from SERCA in response to cellular Ca^{2+} elevations during cardiac systole (contraction), and this dynamic fraction of PLB is rapidly incorporated into PLB pentamers. This process reverses itself during diastole (cardiac relaxation) as Ca^{2+} levels fall, but we (96, 141) and others (97) showed that the rate of PLB pentamer dissociation is slow. This limits the rate of return of PLB monomers to SERCA during diastole. Because of this "kinetic trapping" mechanism, PLB increasingly accumulates in pentamers as the heart rate increases, which helps to relieve inhibition of SERCA during exercise. This mechanism may contribute to the Bowditch effect, the positive relationship between cardiac force and pacing frequency (141). Since both R9C and R14del mutations have been proposed to alter the stability of PLB pentamers, it seems likely that both the equilibrium regulation of SERCA and the ability of PLB regulation to adjust to changing physiological demands may be impacted by these mutations. Here, we used a combination of biochemical and biophysical measurements to study the impact of R9C and R14del on PLB binding equilibria. The results suggest both mutations may dysregulate SERCA function through similar pathogenic mechanisms.

Results

R14del-PLB forms More Stable Pentamers than WT-PLB

We previously reported that a naturally-occurring mutation of PLB linked to DCM, R9C, stabilizes PLB pentamer interactions through oxidative cross-linking of mutant cysteines (22). It, however, remains unknown if the R14del mutation, which is also

associated with DCM, alters PLB oligomerization. To test this hypothesis, we first monitored the oligomerization status of WT-PLB, WT-PLB : R14del-PLB (1:1), and R14del-PLB complexes by immunoblots. **Fig. 1A** showed the expected mix of monomers and oligomers of WT-PLB in homogenates. Unexpectedly, we observed increased oligomerization for R14del-PLB compared to WT-PLB.

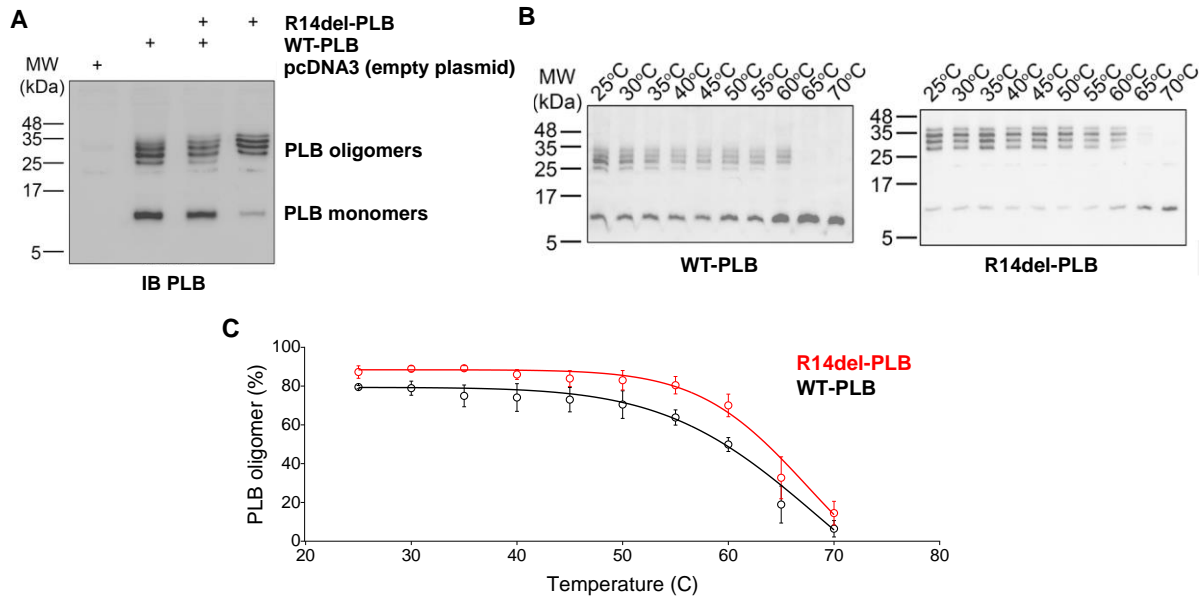


Figure 14. R14del Mutation Increases Oligomerization and Thermostability of PLB Pentamers. **A**, An immunoblot showing incremental R14del-PLB expression led to increased PLB oligomers (25 kDa and above) and reduced PLB monomers (7 kDa). **B**, PLB thermostability assays showing that PLB pentamers (WT-PLB, left panel; R14del-PLB, right panel) gradually dissociated into monomers in responses to increasing temperature (25-70 °C, 5 °C increments). **C**, PLB oligomers vs. temperature plot demonstrating R14del-PLB oligomers (*red*) were more stable than WT-PLB oligomers (*black*) between 25 and 70 °C ($n = 3$).

Mixed hetero-oligomers of R14del- and WT-PLB also showed increased high molecular weight bands compared to WT-PLB homo-oligomers. Next, we tested the thermal stability of the oligomeric species subjecting WT- and R14del-PLB oligomers to increased temperature. Immunoblotting revealed increased stability of R14del-PLB compared to WT-PLB across the tested range of temperature (**Fig. 1B**). Quantification of the oligomer

bands revealed $87.2 \pm 3.2\%$ oligomers for R14del-PLB versus $79.5 \pm 0.8\%$ for WT-PLB at 25 °C, and the R14del-PLB melting curve was right-shifted compared to WT-PLB (**Fig. 1C**). These findings suggested that R14del-PLB is more oligomeric than WT-PLB.

To compare the binding affinity of R14del and WT pentamer interactions within live cell membranes, we quantified fluorescence resonance energy transfer (FRET) between donor (mCerulean)- and acceptor (YFP)-labeled PLB expressed in HEK-293 cells. Specifically, using high throughput cell scoring of the fluorescence intensity of YFP-PLB (as an index of protein expression) and quantitative FRET efficiency in transfected cells, we measured the concentration-dependence of PLB pentamer binding for the WT and R14del PLB. Both WT and R14del pentamer FRET increased with increasing protein concentration until the interaction saturated at a maximum FRET value ($FRET_{max}$) (Fig. 15A). The data were well described by a hyperbolic fit of the form $FRET = (FRET_{max} \times [YFP-PLB]) / (K_D + [YFP-PLB])$, where $FRET_{max}$ is the intrinsic FRET of the bound pentamer at high protein concentration and the K_D is the apparent dissociation constant, which is inversely related to the affinity of the PLB pentamer. The $FRET_{max}$ for PLB pentamers was consistently decreased for the R14del-R14del interaction compared to WT (Fig. 15A), suggesting a small change in the structure of the pentamer. Interestingly, the K_D of the R14del-R14del interaction was significantly lower than that of WT-WT ($p = 1.479 \times 10^{-8}$), indicating that the R14del pentamer binds with higher affinity than WT pentamers. This observation was consistent with SDS-PAGE and thermal denaturation measurements (Fig. 14). We also quantified the affinity of another DCM mutation, R9C, which we previously showed increases pentamer binding affinity (122). Consistent with that previous study, we found R9C mutation increases the $FRET_{max}$

while significantly reducing the K_D the PLB-PLB interaction ($p = 0.012$) (Fig. 15 B,C). Respectively, the data indicate a change in the R9C pentamer structure and an increase in oligomerization affinity.

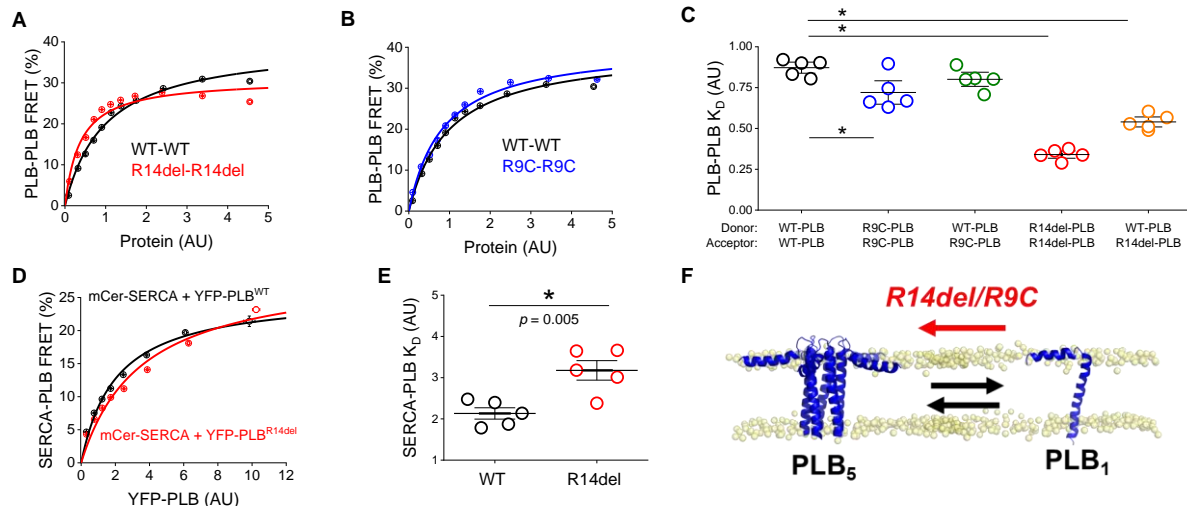


Figure 15. R14del-PLB Mutation Stabilizes PLB Pentamers within Live Cell Membranes. **A**, FRET-based binding curves reveal a left shift in the concentration dependence of the PLB-PLB interaction with R14del mutation. **B**, FRET-based binding curves reveal a left shift in the concentration dependence of the PLB-PLB interaction with R9C mutation. **C**, Apparent K_D s of PLB pentamer interactions with WT- and R14del-PLB. Differences determined by 1-way ANOVA with Tukey's post-hoc ($* = p < 0.05$, $n=5$). **D**, FRET-based binding curves reveal a right shift in the concentration dependence of the PLB-SERCA interaction with R14del mutation. **E**, Apparent K_D s of PLB pentamer interactions with WT- and R14del-PLB. Differences determined by student's t-test ($* = p < 0.05$, $n=5$). **F**, A schematic diagram showing that both R14del and R9C mutations both impact the monomer/pentamer equilibrium by shifting the equilibrium towards the PLB pentamer. PDBs: PLB₅ - 2KYV; PLB₁ - 1FJP.

We noted that the K_D of for R14del-R14del binding was significantly lower than that of R9C-R9C binding ($p = 1.296 \times 10^{-7}$) (Appendix Table D.1), suggesting R14del pentamers are even more stable than R9C pentamers. Since patients that carry R14del and R9C mutations are heterozygous, expressing both WT and mutant copies of the PLB gene, we also quantified FRET between WT-PLB labeled with a fluorescent donor and mutant PLB labeled with a fluorescent acceptor. Interestingly, the WT-R14del K_D

was significantly lower than that of the WT-WT interaction ($p = 0.04$) (Fig. 15C), indicating that R14del-PLB also binds WT-PLB with higher affinity. The value of the WT-R9C K_D was lower than that of WT-WT, which would be consistent with our previous study (122), but this difference was not statistically significant. Overall, the results suggest that both DCM mutations of PLB oligomerize more avidly and this is a dominant effect, increasing sequestration of WT-PLB protomers together with mutant protomers into avidly bound, mixed pentamers.

We also quantified differences in the PLB-SERCA interaction with R14del mutation by measuring FRET between donor labeled SERCA and acceptor labeled PLB (Fig. 15D). The $FRET_{max}$ of SERCA binding with WT-PLB was significantly lower than the interaction of the Ca^{2+} pump with R14del-PLB ($p = 0.01$) (Fig. D.1), suggesting a shorter distance between the fluorescent tags fused to the N-termini of R14del-PLB and SERCA. The K_D of SERCA-PLB binding was significantly higher with R14del-PLB than WT ($p = 0.005$) (Fig. 15E), indicating decreased binding to SERCA. This is probably not due to a true change in the affinity of the R14del-PLB protomer for SERCA, rather we attribute it to decreased bioavailability of the mutant due to increased sequestration into pentamers. Overall, the data indicate that both R9C and R14del mutations cause PLB to form more stable pentamers at the expense of binding to SERCA (Fig. 15F).

R14del-PLB Exchanges Slowly from PLB Pentamers

We have previously shown that PLB-SERCA complexes are dynamically responsive to cellular Ca^{2+} signals, such that a dynamic fraction of PLB monomers unbind SERCA and rapidly incorporate into PLB pentamers during intracellular Ca^{2+} elevations. In our previous study, we found the rates at which PLB exchanges from

pentamers are important for determining the availability of free PLB monomers to regulate SERCA during changing heart rates (141). Here, we performed similar measurements to test how stabilization of the pentamer by R9C and R14del mutations may affect the dynamics of human PLB exchange during Ca^{2+} signaling. Briefly, to recapitulate aspects of muscle cell Ca^{2+} signaling in our experimental system, we transfected HEK-293 cells with RyR2 and SERCA2a. These transfected proteins mediate spontaneous ER Ca^{2+} uptake and release events that mimic the dynamic Ca^{2+} signals in cardiac muscle (103, 121, 141). Cellular Ca^{2+} elevations were detected by confocal microscopy as an increase in fluorescence of the cytosolic Ca^{2+} indicator dye, X-Rhod-1 (Fig. 16 A,B, *black*). To monitor dynamic shifts in PLB oligomerization in response to cellular Ca^{2+} elevations, we measured changes in FRET ratio (acceptor/donor) between donor- and acceptor-labeled PLB over time in response to Ca^{2+} . Consistent with our previous study, a dynamic fraction of PLB was freed from SERCA and rapidly assembled into pentamers during intracellular Ca^{2+} elevations (Fig. 17B, *blue*).

The rate of PLB oligomerization into pentamers during Ca^{2+} release was rapid, closely matching the rate of the increasing Ca^{2+} signal (Fig. 16B). When Ca^{2+} levels decreased to baseline, the unbinding of WT-PLB pentamers lagged behind Ca^{2+} reuptake. Fitting the declining Ca^{2+} and FRET signals to a single exponential function revealed characteristic time constants (τ) for each process. Consistent with our previous study, the τ of WT PLB-PLB unbinding was 2.6 ± 0.4 s, lagging significantly behind Ca^{2+} uptake ($\tau = 1.0 \pm 0.1$ s, $p = 0.01$) (Fig. 16C). Interestingly, the rate of pentamer unbinding with R14del was significantly slower than WT ($\tau = 4.4 \pm 0.7$ s, $p = 0.01$) (Fig.

16D,E), suggesting that the increased PLB-PLB interaction stability with R14del mutation causes PLB pentamers to dissociate at a much slower rate. We were not able to detect FRET changes consistent with association/dissociation of the R9C-PLB pentamers (Fig. 17E, ND). We attribute this to a limited capacity for exchange of PLB from covalently crosslinked pentamers.

To assess the impact of slower pentamer unbinding on the rates of PLB exchange with SERCA, we measured FRET between donor labeled SERCA and acceptor labeled PLB, comparing the dynamics of WT and mutant PLB acceptors. Consistent with our previous study, we observed dynamic decreases in PLB-SERCA FRET in response to Ca^{2+} elevations (Fig. 16A). These equilibrium shifts were observable for WT and both mutant PLB variants. Since we previously showed the rate of return of pentamer dissociation is rate-limiting for the return of PLB to SERCA after Ca^{2+} elevations, we compared the rate of PLB-SERCA rebinding for WT-, R9C-, and R14del-PLB. WT-PLB returned to SERCA with a τ of 3.5 ± 0.2 s, which was significantly slower than the rate of Ca^{2+} uptake ($\tau = 0.5 \pm 0.03$ s, $p = 7.73\text{E-}8$, Fig. 16F). R9C-PLB rebinding to SERCA was slower ($\tau = 4.8 \pm 0.9$ s), though the difference was not significantly different from WT ($p = 0.28$). These FRET changes are likely due to a population of non-crosslinked R9C-PLB that is still able interact dynamically with SERCA with responsiveness to cytoplasmic Ca^{2+} changes. Interestingly, the rebinding of R14del-PLB to SERCA after Ca^{2+} elevations was significantly slower than WT-PLB ($\tau = 5.7 \pm 0.8$ s, $p = 0.003$) (Fig. 16G, H), suggesting that slow unbinding of R14del pentamers causes a considerable delay in the physiological exchange of PLB from its regulatory complex with SERCA during Ca^{2+} signaling.

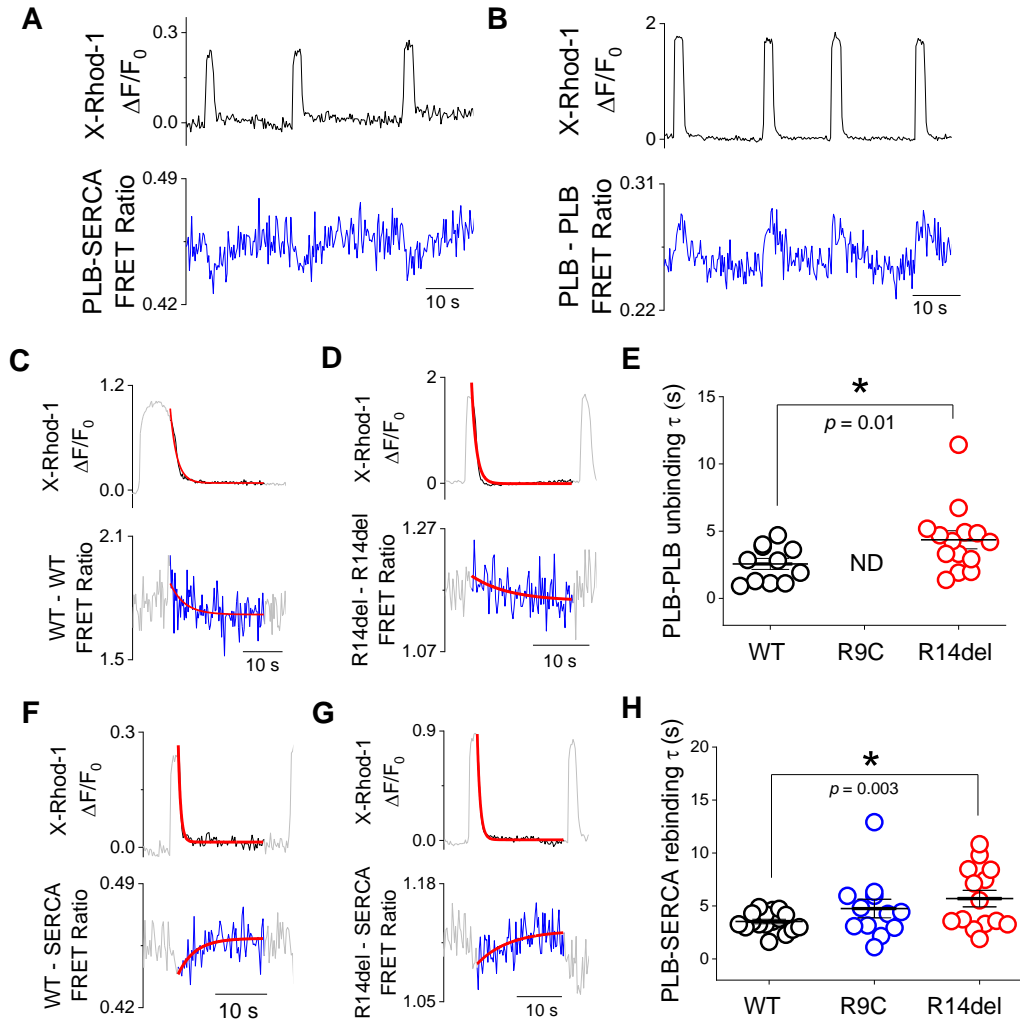


Figure 16. R14del-PLB Exchanges Slowly from Pentamers compared to WT-PLB. **A**, Quantification of X-Rhod-1 fluorescence (*black*) with simultaneous measurement of changes in PLB-SERCA FRET (YFP/Cer ratio) (*blue*). **B**, Quantification of X-Rhod-1 fluorescence (*black*) with simultaneous measurement of changes in PLB-PLB FRET (YFP/Cer ratio) (*blue*). **C**, Representative exponential decay fit of human PLB_{WT}-PLB_{WT} unbinding during Ca²⁺ uptake. **D**, Representative exponential decay fit of human PLB_{R14del}-PLB_{R14del} unbinding during Ca²⁺ uptake. **E**, PLB-PLB unbinding times of WT and mutant pentamers quantified by single-exponential decay fitting. Data are presented as mean \pm SE. Differences determined by one-way ANOVA with Dunn's post-hoc test (* = $p < 0.05$). ND = not detected. **F**, Representative exponential decay fit of PLB_{WT}-SERCA rebinding during Ca²⁺ uptake. **G**, Representative exponential decay fit of PLB_{R14del}-SERCA rebinding during Ca²⁺ uptake. **H**, Rebinding times of WT, R9C, and R14del to SERCA quantified by single-exponential decay fitting. Data are presented as mean \pm SE. Differences determined by one-way ANOVA with Dunn's post-hoc test (* = $p < 0.05$). See Appendix Fig. D.2,3 and Tables D.2-5 for more detailed analysis.

Slow Exchange of PLB Monomers from R14del PLB Pentamers Disrupts Ca²⁺ Regulatory Dynamics

To understand the functional consequence of slower exchange of PLB pentamers containing DCM mutation, we modeled the responsiveness of SERCA regulation to changing Ca²⁺ over a physiological range of pacing frequencies (141). We considered that the enhanced stability of the PLB pentamer via a decrease in PLB-PLB K_D (Fig. 15A,C) could result from either an increase in the rate of pentamer oligomerization (k_{on}) or a decrease in the rate of pentamer dissociation (k_{off}), according to the relationship ($K_D = k_{off}/k_{on}$). Moreover, we observed that the exchange rate for the R14del mutation is slower (Fig. 16), and PLB pentamer exchange is the sum of the on- and off-rates, according to the relationship ($k_{exchange} = k_{on} + k_{off}$). Thus, we conclude that K_D is decreased as a result of a decrease in k_{off} , rather than an increase in k_{on} .

Therefore, we simulated the effect of R14del mutation on PLB binding dynamics by slowing the unbinding rate of PLB pentamers by 2-fold to account for the observed 2-fold change in K_D . Figure 17A shows a simulation of WT- and R14del-PLB interaction with SERCA adjusting from a resting cardiac pacing frequency (60 bpm) to intense exercise (180 bpm) and then back to rest (60 bpm). At 60 bpm, the decreased dissociation rate of R14del pentamers reduced SERCA bound to PLB at resting heart rate (Fig. 17B) and increased the relative amount of PLB sequestered in pentamers (Fig. 17C). Thus, the computational model predicts that R14del causes SERCA to be dysregulated even at resting heart rates. Then, during exercise, SERCA becomes even more dysregulated as a larger fraction of PLB is sequestered into pentamers. Single-exponential decay fitting these changes in PLB-SERCA binding between rest and

exercise demonstrated that the WT regulatory complex adjusts in and out of the exercising condition with a τ of ~ 1 s. However, with the pentamer off rate slowed 2-fold by R14del mutation, these adjustment times occur with a τ of ~ 2 s (Fig. 17D,E), suggesting that adjustments in PLB regulation between rest and exercise occur more slowly with R14del. Additionally, dynamic oscillations in PLB-SERCA binding during Ca^{2+} elevations were also decreased (Fig. 17F), indicating that the beat-to-beat changes in SERCA regulation were blunted by R14del mutation of PLB.

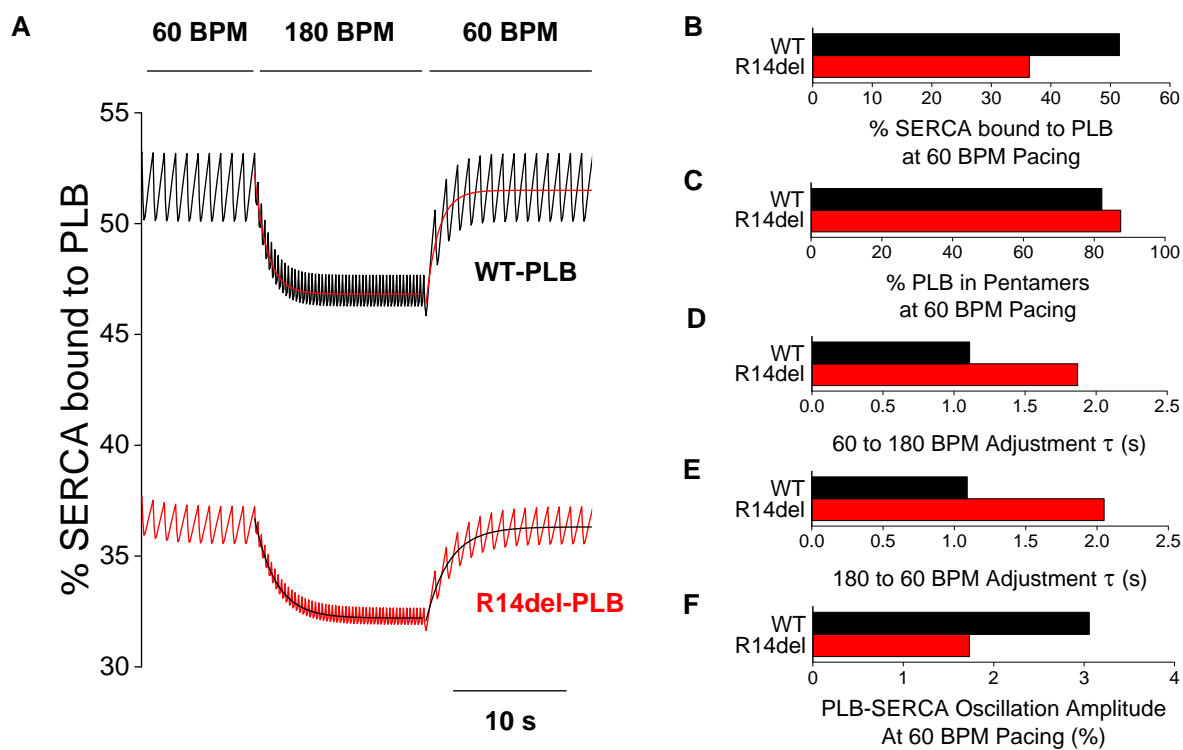


Figure 17. A Computational Model Simulates PLB-SERCA Complex Exchange during Changes in Heart Rate for WT and R14del PLB. A) A simulation of PLB-SERCA binding exchange during Ca^{2+} signaling adjusted from 60 bpm to 180 bpm to 60 bpm pacing rate for WT- (*black*) and R14del-PLB (*red*). Single-exponential decay fits reveal characteristic time constants (τ) for adjustment of PLB-SERCA binding equilibria between 60 and 180 bpm pacing frequencies. **B)** Quantification of the percent SERCA bound to PLB at 60 bpm. **C)** Quantification of the percent PLB in pentamers at 60 bpm **D)** Quantification of the adjustment τ of PLB-SERCA from 60 to 180 bpm. **E)** Quantification of the adjustment τ of PLB-SERCA from 180 to 60 bpm. **F)** Quantification of the oscillation amplitude of PLB-SERCA complexes unbinding and rebinding in response to Ca^{2+} elevations during 60 bpm pacing.

Discussion

R14del Mutation Stabilizes PLB Pentamers

The naturally occurring R14del mutation of PLB was originally discovered in a large family in which carriers experienced lethal hereditary dilated cardiomyopathy by middle age. The seminal first study of this mutation showed that coexpression of R14del-PLB resulted in multiple PLB pentamer bands with different mobilities on Western blot. This was initially taken to indicate destabilization of the PLB pentamer by co-expression of R14del-PLB (135). That conclusion contrasts with the model proposed here, that R14del-PLB *increases the stability of* the PLB pentamer. We also observe multiple bands for PLB pentamers by Western blot (Fig. 14A), but these bands are present for both WT-PLB and R14del-PLB oligomers. This pattern of mobility may arise from differential phosphorylation of PLB protomers in the pentamer (94, 151). Moreover, R14del mutation resulted in an apparent increase in the ratio of pentamers to monomers (Fig. 15A), an increased pentamer melting temperature (Fig. 14B), and a higher affinity for homo-oligomerization in live cells (Fig. 15A-C), consistent with the interpretation that the R14del mutation increases PLB pentamer stability. This model is also compatible with previous studies that reported R14del-PLB to be more pentameric than WT in reconstituted membranes (144).

The expected functional consequence of increased PLB pentamer stability is a decrease in the population of PLB monomers available to inhibit SERCA. This prediction comports with the present observation of decreased binding of R14del-PLB to SERCA (Fig. 15D,E). Although early reports suggested a gain-of-function for R14del-PLB, resulting in superinhibition of SERCA (135), several subsequent biochemical

studies found that R14del-PLB expressed alone (142-144, 149) or in combination with WT (143-145) led to reduced SERCA inhibition compared to WT-PLB. The results of the present study may provide a possible mechanism for the observed loss-of-function character of the R14del mutation, and the dominant negative effect of R14del when coexpressed with WT-PLB (Fig. 14A and 15C), since we observed increased oligomerization of R14del-PLB alone and increased oligomerization of R14del-PLB with WT-PLB (Fig. 15C). By sequestering both mutant and WT-PLB away from SERCA, R14del-PLB has a dominant negative effect that suppresses PLB inhibition of Ca^{2+} transport in heterozygous carriers. This characteristic of the R14del mutation is reminiscent of another DCM mutation of PLB, R9C, which also co-oligomerizes with WT-PLB in stable hetero-pentamers (122). We speculate that oligomerization of micropeptides starts with formation of dimers, then additional protomers are recruited onto that template to form the rest of the higher order oligomers (92). Thus, mutations that increase the stability of the initial dimer have a larger than expected effect in assembling mixed mutant/WT oligomers.

In contrast to consistent observations in biochemical studies of R14del-PLB, the functional consequence of R14del-PLB expression *in vivo* has been less clear. Some physiological studies of R14del-PLB-expressing mice reported weak Ca^{2+} handling and decreased cardiac contractility (152-154) (suggesting R14del-PLB is superinhibitory). In contrast, other studies showed increased SERCA activity, with larger Ca^{2+} transients, enhanced cardiac contractility, and faster relaxation (146, 155) (suggesting R14del-PLB is less inhibitory than WT-PLB). A similar disparity exists in biochemical and physiological studies of the R9C mutation of PLB, which showed a loss-of-inhibition

character *in vitro* (122, 136, 140, 142, 143, 156) but caused diminished calcium handling *in vivo* (136, 156). One explanation for these disparate reports is that there may be a difference between acute effects detected in *in vitro* experiments versus chronic downstream consequences at later stages *in vivo*. Acute studies may illuminate the fundamental pathological mechanism while long term expression may be more representative of the human disease state after full evolution of pathological mechanisms, compensatory physiological adaptation, and cardiac remodeling (139, 140).

R14del PLB Pentamers Exchange Slowly and Are Less Responsive to Changing Physiological Demands

The rate of Ca^{2+} transport by SERCA is a key determinant of the strength of cardiac contraction (inotropy) and the speed of cardiac relaxation (lusitropy). Dynamic adjustment of Ca^{2+} handling enables the heart to increase cardiac output to meet the stress of exercise and then decrease physiological performance after returning to rest. Some of this dynamic modulation of SERCA function is achieved through adrenergic signaling, as discussed below, but there are also important intrinsic mechanisms that contribute to the response. In particular, an increase in heart rate results in an increase in contraction strength. This phenomenon is known as *treppe*, positive staircase, or the Bowditch effect (87, 88, 90, 129, 141). Loss of this positive force-frequency relationship is a hallmark of heart failure in patients (90, 130). We have previously proposed that the dynamic exchange of PLB between SERCA-bound and pentamer-bound pools contributes to the Bowditch effect. Specifically, we found that a fraction of the population of PLB bound to SERCA is liberated during Ca^{2+} elevations and joins the pentameric

pool of PLB, then it unbinds from pentamers and rebinds SERCA when Ca^{2+} concentration returns to baseline (84, 141). Because of the high temporal stability of PLB pentamers (96, 141) (Fig. 16), more frequent Ca^{2+} elevations (at higher heart rates) causes accumulation of PLB in the pentameric form, resulting in less inhibition of SERCA relative to slow heart rates. Thus, the sequestration of PLB in non-inhibitory pentamers is dependent on cardiac pacing frequency (heart rate) (141). Here we find that R14del-PLB pentamers are even more stable than WT-PLB pentamers, causing protomers to unbind more slowly after cellular Ca^{2+} elevations (Fig. 16). A computational model suggested that this caused the PLB-SERCA regulatory complex to respond sluggishly to changing heart rates (Fig. 17D-E) and it also blunted changes in PLB-SERCA binding on a beat-to-beat basis (Fig. 17F). The reduced responsiveness of R14del pentamers to these physiological cues may explain the decreased responsiveness of Ca^{2+} handling to changes in pacing frequency observed in cardiomyocytes with heterozygously expressing R14del-PLB (145, 146). This pathological mechanism may also be operative for the R9C mutation, but we were unable to detect any exchange of R9C-PLB pentamers during cellular Ca^{2+} signals, probably because oxidative cross-linking of R9C-PLB (122) prevents exchange of protomers. Thus, R9C-PLB is even less responsive than the R14del mutant and may contribute to the more severe phenotype of R9C. The average survival for carriers of R9C is estimated at 25 years (136) versus the estimated 38 years for carriers of R14del (138).

Impaired PLB Binding Dynamics May Contribute to Arrhythmogenesis

In addition to DCM, R14del-PLB is also associated with another pathological condition, arrhythmogenic right ventricular cardiomyopathy (ARVC). Human carriers of

R14del mutation experience arrhythmias that often begin before the onset of heart failure and can lead to sudden cardiac death (157, 158). Although ARVC is more commonly associated with mutations in proteins of the intercalated disc (159, 160), it has been proposed that R14del-PLB and these genetic perturbations of intracellular integrity may lead to the development of arrhythmia through a common pathogenic mechanism. Specifically, disruptions of the desmosome in ARVC have been found to result in a maladaptive changes in Ca^{2+} handling by increasing PLB phosphorylation (160, 161). While phosphorylation normally causes a temporary increase in SERCA activity during physiological stress that is readily reversible during rest, chronic hyperphosphorylation of PLB after desmosome disruption may lead to SR Ca^{2+} overload and premature ventricular contractions (161). Indeed, increased PLB phosphorylation has been reported across various models of arrhythmogenic cardiomyopathy (44-46). Interestingly, like R14del mutation, PLB phosphorylation also increases the oligomerization (16, 17) and temporal stability of pentamers (19). Thus, we speculate that enhanced pentamer stability and impaired PLB binding dynamics, caused by either hyperphosphorylation of PLB or R14del mutation, may serve as common arrhythmogenic mechanisms in ARVC.

Summary

Figure 18 illustrates the principal finding of this study, that the R14del mutation of PLB causes hyper- stabilization of PLB pentamers and blunts the dynamics of regulation of cardiac calcium handling by PLB. This is similar to the reversible stabilization of pentamers induced when PLB is phosphorylated or the covalent crosslinking of PLB oligomers observed with the R9C mutation of PLB. Decreasing the

off-rate of PLB monomers from pentamers depletes the overall levels of SERCA regulated by PLB. In addition, excessive stabilization of the oligomer also slows the release of PLB protomers into the active monomeric pool as cytosolic calcium levels fall during diastole. This results in sluggish transitions between the different regulatory stances for exercise versus rest, and it damps the beat-to-beat changes in regulation of SERCA by PLB. We propose that this poor responsiveness to physiological stress stimulates cardiac remodeling and eventual failure of the heart in dilated cardiomyopathy.

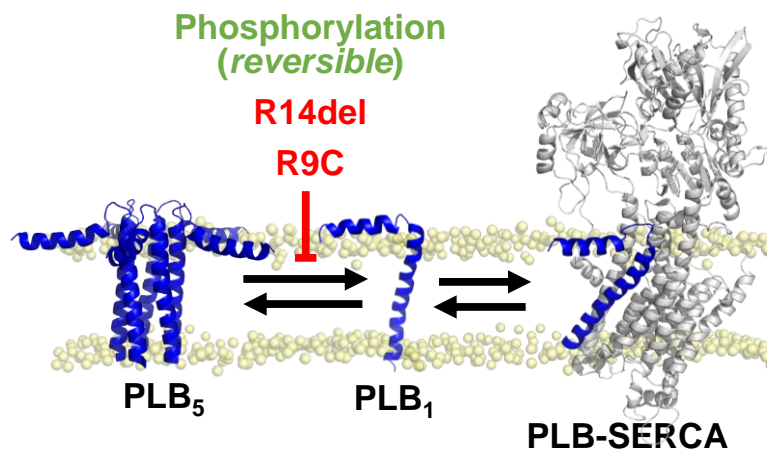


Figure 18. Effects of Phosphorylation and DCM Mutations on PLB Regulatory Interactions. A schematic diagram displaying how PLB phosphorylation and DCM mutations of PLB, R14del and R9C, impact the equilibrium binding of monomeric PLB (PLB₁) with pentamers (PLB₅) and SERCA (PLB-SERCA) by decreasing the rate of PLB monomers unbinding from pentamers.

CHAPTER SIX

PHOSPHOLAMBAN INHIBITS THE CARDIAC CALCIUM PUMP THROUGH REVERSING THE ALLOSTERIC ENHANCEMENT OF CALCIUM AFFINITY BY ATP

Introduction

The sarcoplasmic reticulum Ca^{2+} -ATPase (SERCA) sequesters intracellular Ca^{2+} into the lumen of the endoplasmic reticulum (ER) to establish a reservoir for cell signaling. This is a critically important process in all cell types, and it is energized by ATP hydrolysis and autophosphorylation of the Ca^{2+} pump. Ca^{2+} transport plays a particularly central role in cardiac physiology. The release of Ca^{2+} from the sarcoplasmic reticulum (SR) initiates shortening of the cardiac muscle cell during systole (cardiac contraction). Then, SERCA transport removes Ca^{2+} from the cytosol during diastole (cardiac relaxation) and re-establishes the Ca^{2+} stores in preparation for the next cardiac cycle (21, 34). The primary regulator of SERCA function in the heart is phospholamban (PLB), a transmembrane micropeptide that physically interacts with SERCA and inhibits Ca^{2+} transport (70, 124). PLB regulation of SERCA is known to be critical for human survival since naturally occurring mutations of PLB that nullify its inhibitory function are associated with heart failure and premature death in carriers (67). PLB reduces the Ca^{2+} sensitivity of SERCA during cycling, increasing the Ca^{2+} concentration required for pump turnover (11, 73). However, equilibrium measurements of Ca^{2+} binding (in the absence of ATP) have not shown any effect of PLB on the affinity of SERCA for Ca^{2+} (6, 11, 76). These apparently contradictory results have been

reconciled by invoking a kinetic mechanism, that PLB slows the Ca^{2+} binding step of the SERCA enzymatic cycle. This could account for the observed Ca^{2+} desensitization effect of PLB without reducing the true Ca^{2+} affinity of SERCA under equilibrium conditions (11).

Alternatively, we speculated that experiments measuring Ca^{2+} binding in the absence of ATP may overlook important allosteric effects of bound nucleotide. In addition to the role of ATP as a source of energy to fuel Ca^{2+} transport, ATP binding to SERCA increases the transporter's affinity for Ca^{2+} . This effect of ATP, referred to as “nucleotide activation”, increases both the rate of Ca^{2+} binding (63, 64, 162) and the Ca^{2+} affinity of the pump measured using $^{45}\text{Ca}^{2+}$ (120, 163). Since the effects of nucleotide activation are the opposite of PLB inhibition, we hypothesize that PLB may inhibit SERCA through a mechanism of reversing of nucleotide activation, reducing the true affinity of SERCA for Ca^{2+} . Since previous experiments measuring the impact of PLB on Ca^{2+} -binding were always performed in the absence of ATP (to prevent enzymatic cycling) (6, 11, 76), to our knowledge this possibility has not been investigated. To test this mechanistic hypothesis, we investigated the interplay of ATP binding, Ca^{2+} binding, and PLB binding using a biosensor that reports SERCA conformation through changes in intramolecular fluorescence resonance energy transfer (FRET) (65). This biosensor-based assay offers significantly improved sensitivity compared to conventional $^{45}\text{Ca}^{2+}$ -binding measurements. The results support a new paradigm for the mechanism of regulation of SERCA by PLB.

Results

PLB Reverses Nucleotide Activation of SERCA Ca²⁺ Affinity by ATP

We previously developed a biosensor called “2-color SERCA” consisting of two fluorescent proteins fused to the A- and N- domains of the cytoplasmic headpiece of SERCA to report its overall conformation by intramolecular FRET (65, 76, 103). 2-color SERCA FRET increases in response to increasing Ca²⁺ concentration due to closure of the labeled headpiece domains as the transporter binds Ca²⁺ (65) (Fig. 19A). Here, we used this 2-color SERCA FRET measurement as an index for relative Ca²⁺ binding to SERCA to study the activating and inhibitory effects of ATP and PLB, respectively, on SERCA Ca²⁺ affinity.

Time-correlated single photon counting (TCSPC) was used to measure changes in the average FRET efficiency of 2-color SERCA expressed in microsomal vesicles, in solutions containing varying concentrations of free [Ca²⁺] (Fig. 19B, *black*) (Appendix Fig. E.1, *See methods*). A fit of the data with a Hill function yielded a minimal FRET efficiency for 2-color SERCA at low [Ca²⁺] of 13.5 ± 0.5 % which increased with increasing [Ca²⁺] to a maximum of 17.9 ± 0.4 %. The fit revealed a Ca²⁺ binding constant (K_{Ca}) of 1.7 ± 0.1 μ M for SERCA alone. This value is consistent with previous measurements of 2-color SERCA Ca²⁺ affinity (65, 76, 103). Addition of the non-hydrolyzable ATP analog, AMPPCP (500 μ M) shifted the Ca²⁺ binding curve to the left, indicating an increase in Ca²⁺ affinity (K_{Ca} of 333 ± 32 nM, *t*-test $p = 6.2E-9$) (Fig. 19B, *red*). We noted that FRET at low [Ca²⁺] was significantly increased when nucleotide was present to 15.4 ± 0.4 % (*t*-test $p = 0.008$, Appendix Fig. E.2), consistent with a more compact SERCA headpiece after nucleotide binding (53, 103).

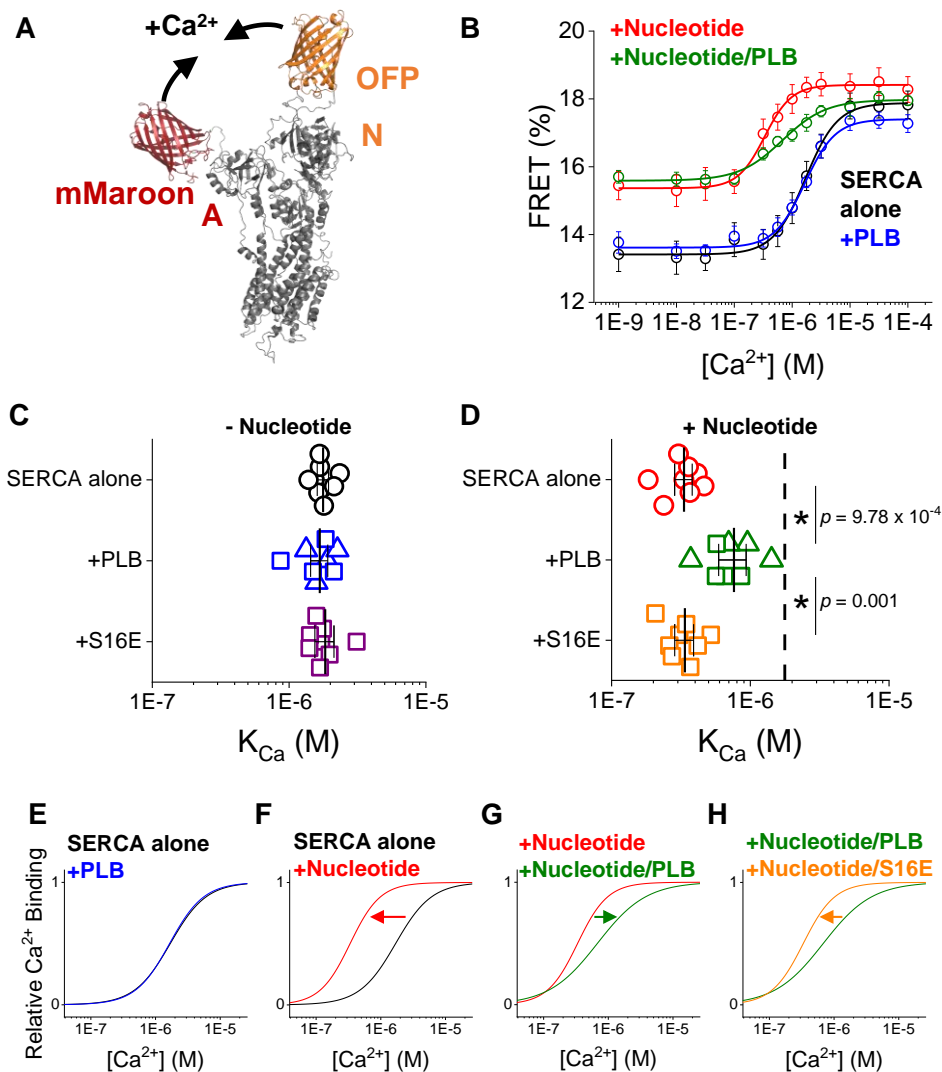


Figure 19. PLB Reduces the Ca^{2+} Affinity of SERCA by Reversing Nucleotide Activation. **A**, 2-color SERCA biosensor labeled on the A and N domains detects headpiece closure during Ca^{2+} binding by intramolecular FRET. **B**, FRET changes during Ca^{2+} binding measured with SERCA alone (*black*), with AMPPCP (*red*), with PLB co-expressed (*blue*), and with both AMPPCP and PLB (*green*). **C**, Apparent K_{Ca} of SERCA alone (*black*) with co-expression of WT- (*blue*) or S16E-PLB (*purple*) in the absence of nucleotide. SERCA to PLB transfection ratio indicated by Δ (1:3) or \square (1:5). Differences determined by one-way ANOVA with Tukey's post-hoc (* = $p < 0.05$, $n = 8$). See Appendix Table E.1,2. **D**, Apparent K_{Ca} of SERCA alone (*red*) with co-expression of WT- (*green*) or S16E-PLB (*orange*) in the presence of nucleotide. SERCA to PLB transfection ratio indicated by Δ (1:3) or \square (1:5). Reference line indicates the average K_{Ca} of SERCA alone with no nucleotide. Differences determined by one-way ANOVA with Tukey's post-hoc (* = $p < 0.05$, $n = 8$). See Appendix Table E.3,4. **E-H**, Fitted curves from Ca^{2+} binding measurements (as in **B**) normalized to a common minimum and maximum show that PLB inhibition of the relative Ca^{2+} affinity of SERCA is dependent on nucleotide activation and relieved by S16E mutation.

The increase in SERCA Ca^{2+} affinity with AMPPCP is consistent with previous studies that show that nucleotide binding allosterically increases SERCA's affinity to subsequently bind Ca^{2+} (nucleotide activation) (64, 120, 163).

We investigated the impact of PLB on Ca^{2+} binding to SERCA in the presence and absence of nucleotide using microsomal vesicles co-expressing 2-color SERCA with unlabeled PLB. Since inhibition of SERCA is relieved by PKA phosphorylation of PLB at serine 16 (70, 95, 164, 165), we also tested the effect of co-expressing PLB with a phosphomimetic mutation, S16E (Appendix Fig. E.3). In the absence of nucleotide, we did not observe any effect on SERCA Ca^{2+} affinity from coexpression of WT- or S16E-PLB (Fig. 19C and Appendix Table E.1,2). Interestingly, when nucleotide was present, PLB significantly increased the K_{Ca} of SERCA to 782 ± 142 nM ($p = 9.78\text{E-}4$) compared to SERCA alone (Fig. 20D). This effect of PLB on Ca^{2+} affinity was reversed by S16E mutation, with a significant decrease in the K_{Ca} (337 ± 35 nM, $p = 0.001$) compared to WT-PLB (Fig. 19D and Appendix Table E.3,4). Taken together, these results suggest that PLB has no effect on Ca^{2+} affinity in the absence of nucleotide (Fig. 19E) in agreement with past results (6, 11, 76). However, when nucleotide is bound to SERCA, the pump binds Ca^{2+} with much higher affinity (63, 64, 120, 163), indicated by an appreciable left shift of the concentration dependence of relative Ca^{2+} binding (Fig. 19F). Under these biochemical conditions, PLB mediates its primary function of inhibiting SERCA Ca^{2+} affinity by reversing this allosteric activation of the pump by ATP, shifting the curve partially back to the right (Fig. 19G). PLB inhibition is relieved when PLB is phosphorylated by PKA, and we were able to simulate this relief of inhibition using a phosphomimetic S16E mutation which shifted the curve back to the left (Fig.

20H). Although we made Ca^{2+} binding measurements with samples co-expressing WT-PLB at both a 3:1 and 5:1 PLB to SERCA ratios, we did not detect a significant difference in Ca^{2+} affinity between these samples. Only the cooperativity of Ca^{2+} binding in the presence of nucleotide was significantly increased in samples with a higher PLB to SERCA expression ratio of 5:1 compared to 3:1 (Appendix Fig. E.4) (166).

MD simulations of SERCA with ATP and PLB

To investigate how nucleotide activation and PLB inhibition impact the structure of SERCA, we performed molecular dynamics (MD) simulations of SERCA with and without ATP bound within the N domain and also in the presence and absence of PLB bound within its regulatory cleft. For simulations with PLB in complex SERCA, the complexes were stable on the microsecond timescale covered by the trajectories. In simulations of the PLB+ATP condition, we noticed ATP unbinding from its active site in later frames of the trajectories. Since ATP also causes closure of the 2-color SERCA headpiece at low Ca^{2+} (**Fig. 1B**), we also used this change in intramolecular FRET to measure ATP binding to 2-color SERCA and evaluate how the concentration-dependent binding of ATP is affected by PLB co-expression. We were not able to detect any significant effect of PLB expression (5:1 PLB to SERCA ratio) on ATP binding affinity (Appendix Fig. E.5). Therefore, we attribute ATP unbinding in trajectories where PLB was also present to be an artifact of the simulations.

First we evaluated how ATP and PLB impact the structural dynamics of the Ca^{2+} transport sites of SERCA by analyzing the root mean square fluctuation (RMSF) values for the acidic residues responsible for coordinating Ca^{2+} ions in the binding sites: E309, E771, D800, and E908 (8, 167). We noted that the Ca^{2+} gating residue, E309, was more

dynamic on this microsecond timescale compared to the other residues, as indicated by higher RMSF values across all trajectories (Fig. 20A).

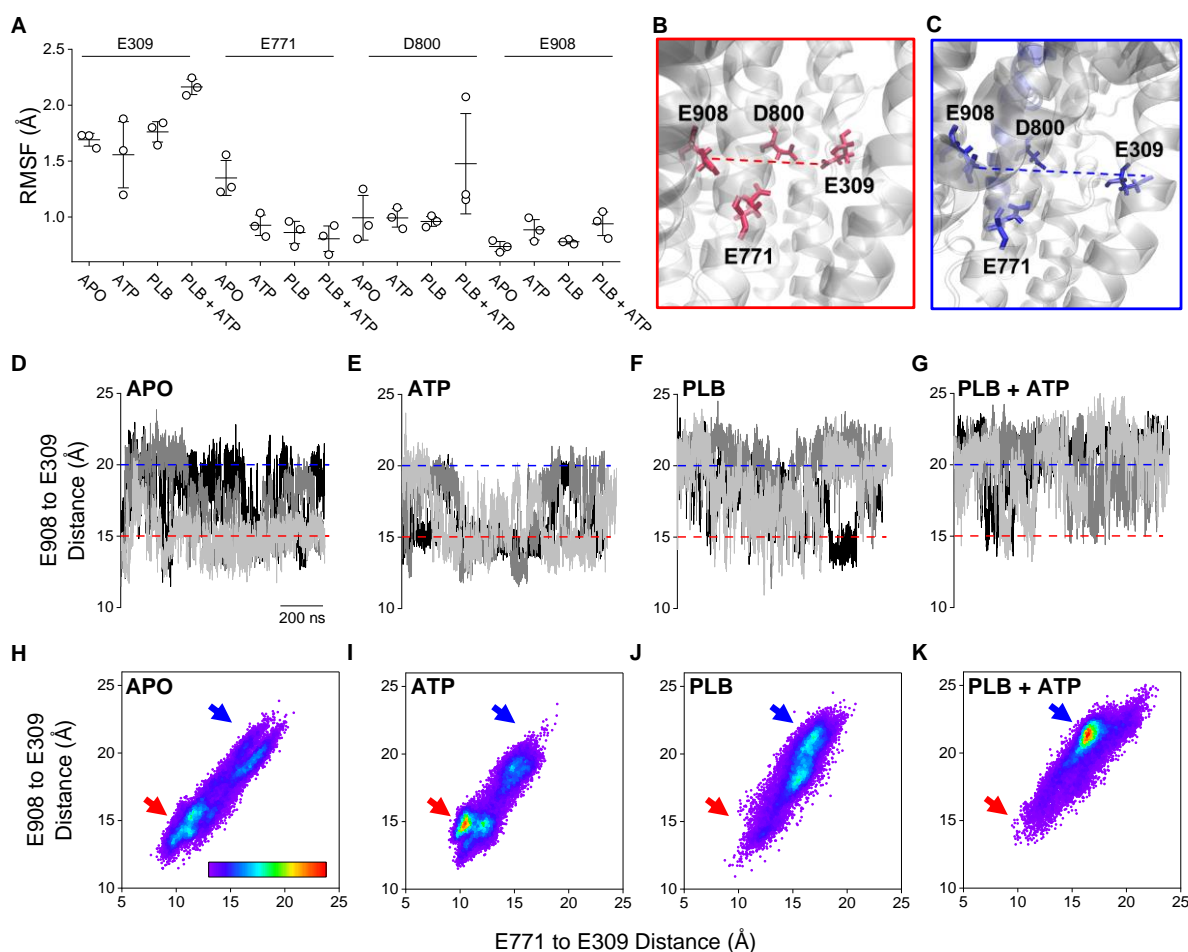


Figure 20. Effects of ATP and PLB on Structure of SERCA Ca²⁺ Transport Sites. **A**, RMSF values for the acidic residues that coordinate Ca²⁺ ions in Ca²⁺ transport sites of SERCA. **B**, Ca²⁺ binding residues shown in a conformation where E309 faces the binding pocket and completes the binding sites **C**, Ca²⁺ binding residues shown in a conformation where E309 is oriented away from the binding pocket, deforming the binding sites. **D-G**, Time-dependent changes in the distance between E908 and E309 for replicates 1 (*black*), 2 (*grey*), and 3 (*light grey*) for each of the simulated conditions. Red and blue dashed lines indicate the distances represented in panels B and C respectively. **H-K**, 2D density maps showing how the distribution of distances occupied by E309 from residues E908 and E771 is affected by the presence of ATP and PLB. Color scale bar represents the density of points ranging from 0 (white) to 21% (red) occupancy. Red and blue arrows indicate the E309 positions represented in panels B and C respectively. Histograms of the relative occupancy of distances along each dimension are available in Appendix E.6.

Inspection of the Ca^{2+} binding sites revealed that these residues conform to 2 major geometries during the simulations: (1) a closed conformation where E309 faces the binding pocket and completes the binding sites (Fig. 20B) and (2) a more open conformation where E309 is oriented away from the other residues, deforming the Ca^{2+} transport sites (Fig. 20C) (8, 168). In contrast to E309, E908 displayed the most stability of these residues across trajectories indicated by the lowest RMSF values (Fig. 20A). Since E908 is located across from E309 in the Ca^{2+} binding pocket (Fig. 20B,C), we monitored the time-dependent change in distance between these residues as an index of the 2 major geometric conformations, with the closed conformation corresponding to a short distance from E908 to E309 ($\sim 15 \text{ \AA}$) (Fig. 20B, *red dotted line*) and the open conformation characterized by a long distance ($\sim 20 \text{ \AA}$) (Fig. 20C, *blue dotted line*). Figure 20D-G show the repeated structural transitions between these two conformations over time. We noted that ATP induced a significant ordering of the binding site, with greater sampling of the shorter E908-E309 distance compared to the APO condition (Fig. 20D,E). This stabilization of a closed, Ca^{2+} -competent conformation is compatible with the observed ATP-dependent increase in Ca^{2+} affinity (Fig. 19B). Interestingly, PLB reversed this nucleotide activation, and the PLB+ATP condition was characterized by greater sampling of the longer E908-E309 distance (Fig. 20G). Triangulation of the dynamic E309 residue with E908 and E771 provided additional insight into the apparent disorder-order transition induced by ATP binding. A 2-dimensional density map of the E309-E908 and E309-E771 distances sampled during the simulation shows a wide distribution of distances for the APO condition, with two broad, poorly-defined peaks representing the closed (Fig. 20H, *red arrow*) and open conformations (Fig. 20H, *blue*

arrow). After addition of ATP, there was a marked disorder-to-order transition, resulting in a sharply focused peak at short distances (Fig. 20I, *red arrow*), signifying a shift to a more well-defined, closed conformation. This highly ordered nucleotide-activated conformation of SERCA was abolished by addition of PLB (Fig. 20J,K). The 2-D density map shows that addition of PLB shifted the population to an open conformation with a sharp focus at long distances (Fig. 20K). Even in the absence of ATP, the presence of PLB resulted in a shift to longer distances compared to APO (Fig. 20F, J). Since the APO and PLB-bound conditions show the same low Ca^{2+} affinity in the absence of nucleotide (Fig. 19E), we conclude that high affinity Ca^{2+} binding requires both (1) population of the closed conformation of the binding site (Fig. 20E, *red arrow*) and (2) ordering of the Ca^{2+} -binding residues into a sharp focus. This sharp focus results from allosteric activation of SERCA by ATP binding.

Discussion

In previous studies, we (116, 169, 170) and others (11, 79, 82, 171) have investigated SERCA regulation by PLB under the premise that PLB reduced the kinetics of Ca^{2+} binding to SERCA, altering the pump's "apparent" Ca^{2+} affinity without changing the actual affinity of the Ca^{2+} binding sites. This perspective was based on Ca^{2+} -binding experiments performed in the absence of ATP (6, 11, 76), a condition routinely used to stop SERCA enzymatic cycling for equilibrium measurements. In the present study, we prevented enzymatic cycling of the pump using a non-hydrolyzable analog of ATP, which enabled quantification of Ca^{2+} -binding to the nucleotide-bound SERCA under equilibrium conditions. These experiments also exploited a fluorescent biosensor, "2-color SERCA", that reports the Ca^{2+} -dependent conformation change in the SERCA headpiece with a

change in FRET (65). This assay offers an advantage of 2-3 orders of magnitude improved sensitivity compared to conventional quantification of $^{45}\text{Ca}^{2+}$ binding to cardiac SR (11). The results recapitulate several key observations from previous studies. We found that the presence of nucleotide greatly increased the Ca^{2+} sensitivity of SERCA, in agreement with past results (63, 64, 120, 162, 163). This phenomenon referred to as “nucleotide activation” (Fig. 19F). We also reproduced the observation that there is no effect of PLB on equilibrium Ca^{2+} binding to SERCA in the absence of nucleotide (Fig. 19E) (6, 11, 76). However, PLB *does* decrease SERCA’s equilibrium Ca^{2+} binding in the presence of non-hydrolyzable nucleotide (Fig. 19G). Others have previously speculated that nucleotide might be needed to detect the inhibitory effect of PLB (82, 172), but to our knowledge, this is the first observation that PLB decreases the true affinity of the Ca^{2+} binding sites of non-cycling SERCA. The data suggests that the mechanism of action of PLB involves modulating the allosteric connection between the ATP- and Ca^{2+} -binding sites.

MD simulations provided insight into this allosteric mechanism. Of particular interest were the dynamic motions we observed in glutamine 309 (Fig. 20A). This residue has well-established roles in both gating the entry of Ca^{2+} ions into the binding cavity (8, 168) and allosterically coupling the structure of the TM and headpiece domains of SERCA (173, 174). In the APO condition, we observed this residue moving in and out of the Ca^{2+} binding pocket (Fig. 20H), consistent with crystal structures that have shown E309 in either position. E309 faces the binding pocket in Ca^{2+} bound states of SERCA (10, 12) but faces away when thapsigargin is bound and inhibits Ca^{2+} binding (8). ATP and PLB both impacted the Ca^{2+} binding sites by affecting equilibrium position of this residue. In

simulations with ATP bound, our results showed E309 more frequently occupied a well-defined position in the binding pocket (Fig 20B,I), suggesting that ATP binding to SERCA allosterically primes the transporter for Ca^{2+} binding. This is in agreement with past biochemical studies that found E309 contributes to the enhancement of Ca^{2+} binding and occlusion by adenosine nucleotides (168). Interestingly, simulations with PLB bound in complex with SERCA showed the opposite trend, with the PLB+ATP condition exhibiting a strong preference for occupying the more open state of E309 where the Ca^{2+} binding site is less formed (Fig. 20C,K). This suggests that the PLB interaction with SERCA disrupts the allosteric communication between the ATP and Ca^{2+} binding sites and stabilizes the pump in a less competent conformation for binding Ca^{2+} .

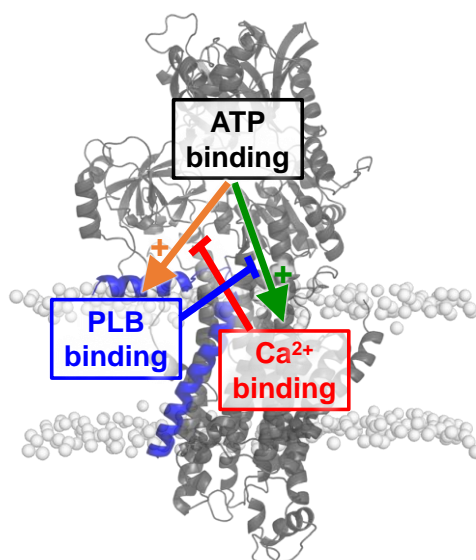


Figure 21. A Schematic Diagram of the Allosteric Relationships between ATP, PLB, and Ca^{2+} Binding to SERCA.

In our previous study (169), we showed that the PLB-SERCA regulatory complex is most stable when the Ca^{2+} pump is in its ATP-bound conformation (78, 82, 175). Interestingly, this ATP-dependent increase in PLB-SERCA affinity was reversed upon Ca^{2+} binding (169). This interplay between PLB-SERCA affinity with the binding of ATP

and Ca^{2+} suggests that the allosteric networks that PLB uses to inhibit SERCA also feedback and affect the energetics of its regulatory binding to the pump. Figure 21 illustrates the allosteric relationships between SERCA binding sites for ATP, Ca^{2+} , and PLB. When ATP binds to its active site in the N-domain allosterically activates the Ca^{2+} binding sites in the transmembrane domain, increasing SERCA Ca^{2+} affinity (Fig. 21, *green*). ATP binding also causes PLB to interact more avidly with its transmembrane regulatory cleft (Fig. 21, *orange*). Here, we demonstrated that through this tighter interaction with ATP-bound SERCA (169), PLB mediates its inhibition through reversing nucleotide activation of SERCA Ca^{2+} binding (Fig. 21, *blue*). The affinity of PLB binding relaxes after Ca^{2+} is bound and SERCA transitions through subsequent steps of its catalytic cycle (Fig. 21, *red*) (169). The results presented here provide important insights into both the mechanism of PLB inhibition and the allosteric networks with which it interacts to regulate SERCA. These insights may inform the rationale design of therapies that modulate PLB and SERCA function through these allosteric networks.

CHAPTER SEVEN

FUTURE DIRECTIONS & CLINICAL INSIGHTS

Overview of SERCA-Targeted Therapies for Heart Failure

By sequestering Ca^{2+} to the sarcoplasmic reticulum, the cardiac Ca^{2+} pump SERCA2a plays a central role in the healthy function of both contraction and relaxation of heart muscle cells. Although heart failure encompasses a complex family of disorders with a plethora of potential causative factors, several common findings point to impaired Ca^{2+} handling as a key pathway affected in its disease progression. Across various forms of heart failure, SERCA expression is decreased, Ca^{2+} handling is dysregulated, and either contraction, relaxation, or both are impaired (31, 33, 34, 131, 132, 175). These contribute to an overall loss of cardiac output in patients. These common findings in end-stage heart failure have drawn attention to SERCA as an appealing therapeutic target (44, 176). Since SERCA function contributes to both phases of the cardiac cycle, correcting deficient Ca^{2+} transport by SERCA in patients may simultaneously restore the function of both contraction and relaxation in failing hearts. Physicians and researchers have proposed multiple strategies to increase SERCA function in patients including increasing SERCA expression, directly activating Ca^{2+} transport function of existing SERCA pumps, or relieving SERCA inhibition by PLB. The insights provided by this dissertation may help to inform many of these therapeutic strategies to target SERCA in the failing heart.

SERCA2a Gene Delivery

To amend the reduced expression of SERCA in patients with heart failure, SERCA2a gene delivery was long sought after as the prevailing strategy to ameliorate reduced Ca^{2+} transport function in patients. After great success in both small and large animal models of heart failure (36, 177, 178), AAV1/SERCA2a was selected as the first cardiac gene-therapy ever attempted in patients (39, 40). Unfortunately, AAV1/SERCA2a gene therapy failed to improve clinical outcomes for patients in phase 2b trials. Although the clinicians and authors of the trial speculated that inadequate delivery of the vector may be a cause for this negative result (41), the failure of SERCA2a gene delivery has refocused the field away from SERCA gene expression and onto developing small molecules (21, 44, 179) and alternative gene therapies (38, 100-102, 180) to activate the function of the remaining SERCA pumps in the failing heart. Since these alternative strategies influence the SERCA regulatory network in the heart rather than its expression, it is all the more important that we understand the endogenous regulatory mechanisms for dynamically controlling SERCA function. Our results provide mechanistic insights that will inform the rationale design of these new therapeutic agents to work with these regulatory mechanisms.

Direct Activation of SERCA

An appealing alternative to SERCA gene delivery is direct activation of the remaining Ca^{2+} pumps in the failing heart using alternative gene therapies or small molecules. While high throughput screens of small molecule libraries have been successful in identifying compounds that activate SERCA (42, 44, 45, 179, 181-183), these *in vitro* activators have not yet translated to a clinically effective therapy *in vivo*.

These compounds activate SERCA either by increasing the maximal rate of Ca^{2+} transport (42, 181) or by increasing its Ca^{2+} affinity (lowering K_{Ca}) (182, 183). In the present study we investigated intrinsic physiological mechanisms which activate SERCA through affecting both of these parameters. Understanding how these molecular mechanisms cause SERCA activation may help to identify SERCA activators more efficiently and accelerate their translatability to effective clinical therapies.

Because of their smaller size (<100 amino acids), SERCA-activating micropeptides like DWORF or inhibition-null PLB mutants may pose a lower metabolic burden for expression in the heart than SERCA2a (997 amino acids) and could therefore serve as promising alternatives for cardiac gene therapy (37, 38, 100-102). Gene delivery of DWORF has been shown to effectively remedy several animal models of heart failure (38, 100-102). However, the intrinsic mechanism by which DWORF activates SERCA is not well understood. Our results suggest that DWORF binds more avidly to SERCA during rate-limiting transitions of its enzymatic cycle (Fig. 8, Table 1). We speculate that DWORF may increase V_{max} by stabilizing a high energy intermediate of the pump required for the transition from E1P to E2P. In doing so, DWORF may reduce an energy barrier and increase pump flux through this rate limiting step, enhancing the overall turnover rate of the pump. This mechanistic hypothesis for DWORF activation of V_{max} could be directly tested by measuring the effect of DWORF on the rate of this transition measured by stopped-flow (49) or X-ray solution scattering (184). It is also possible that other SERCA activators that increase V_{max} may share a common mechanism for stimulating SERCA. Future studies will reveal if small molecule SERCA activators such as CDN1163 (42, 181) display conformational selection for E1P

and E2P states of SERCA and increase the kinetics of the rate-limiting transition between these conformations.

Our results also provide mechanistic insights for increasing SERCA Ca^{2+} affinity. Specifically, we found evidence to support that ATP binding to its active site in the N domain allosterically increases the affinity of SERCA Ca^{2+} binding sites in the transmembrane domain through “nucleotide activation” (Fig. 19) (59, 63, 64). Molecular dynamics simulations of SERCA in complex with ATP and/or PLB provided insights into the structural basis for this allosteric activation (Fig. 20). Our collaborators at the University of Southern Denmark, Konark Bisht and Himanshu Khandelia, are currently using GSA tools (185) to map out the allosteric pathway that relays this “nucleotide activation” signal from the ATP binding site to the sites of Ca^{2+} binding and the micropeptide binding cleft. The finding that PLB inhibits SERCA through modulating nucleotide activation (Fig. 19) suggests that this allosteric network has potential to be influenced by other peptides and small molecules. It’s possible that structural mapping of this allosteric pathway may lead to identifying sites that can be used to either decrease or enhance SERCA Ca^{2+} affinity. Future studies may identify small molecules that activate SERCA Ca^{2+} affinity through docking to cryptic sites along the allosteric network mapped out from our MD trajectories.

Relief of PLB Inhibition of SERCA

Another proposed avenue to activate SERCA in the failing heart is to target PLB to relieve its inhibition of Ca^{2+} transport. An advantage of this approach is, unlike SERCA, PLB expression is specific to the heart, so theoretically PLB-targeted therapies would be inherently cardio-specific (37, 186). Researchers have identified several

potential means of achieving this including gene delivery of PLB-competitors (37), siRNA knockdown of PLB expression (187), and small molecules that disrupt the PLB-SERCA regulatory complex (171, 188). However, few of these approaches have translated to a safe and effective therapy to treat patients. The insights provided by this study inform the pros and cons of these approaches.

In Chapter Six, we discovered the intrinsic mechanism of PLB inhibition of SERCA is mediated through reversing an allosteric activation of transporter's Ca^{2+} affinity by ATP (Fig. 19). This insight into the function of PLB provides a direct means of testing the impact of PLB-targeted therapies on inhibition. Rather than attempting to find compounds that disrupt the PLB-SERCA complex, future small molecule screens may be used to directly test for relief of the effect of PLB on Ca^{2+} binding to the ATP-bound Ca^{2+} pump. By mapping the allosteric network that PLB interacts with to regulate SERCA, we may identify potential cryptic sites that can be targeted with small molecules to modulate PLB inhibition.

Relieving PLB inhibition through PLB phosphorylation is an important mechanism for activating cardiac reserve in response to adrenergic signaling (70). In Chapter Four, we found that PLB pentamers serve an additionally important role in sequestering inhibitory PLB monomers away from SERCA to lower inhibition in response to accelerated cardiac pacing (Fig. 13). We also found this mechanism is tunable by PLB phosphorylation which stabilizes pentamers and slows the release of monomers (Fig. 12), enhancing the relief of inhibition in response to pacing. Interestingly, a recent study found that PLB pentamers are important for myocardial adaptation to sustained pressure overload (189). Specifically, the authors found that PLB KO mice performed

better in response to transaortic constriction induced cardiomyopathy when transduced with WT-PLB than with the less pentameric AFA-PLB mutant. Future experiments will show that PLB pentamers are required for PLB to contribute to the heart's positive force-frequency relationship and tolerating both physiological and pathological forms of cardiac stress.

The discovery that the dynamic exchange of PLB from pentamers is important for responding to exercising heart rates presents important insight into how heart failure therapies may interplay with the SERCA regulatory network during rest and exercise. While siRNA knockdown of PLB has found some early success in iPSC cardiomyocytes (187), our results indicate that decreasing PLB expression may reduce PLB bound to SERCA at rest and decrease exercise tolerance. Since our results suggest PLB pentamer stability is tunable by phosphorylation (Fig. 12) or interactions with mutant PLB (Fig. 15,16), it is possible that in the future PLB pentamers may serve as a novel drug target. Ideally, SERCA-targeted therapies will attempt to preserve the exchange of PLB pentamers and the PLB-SERCA interaction in order to help maintain exercise tolerance in patients.

Limitations of SERCA Activation

One important consideration for therapeutic SERCA activation, either by direct stimulation or relief of inhibition, is the metabolic demand that increasing SERCA activity will have on cellular supplies of ATP. The increased metabolic demand of SERCA on the heart may deplete cellular antioxidants and result in a net increase in reactive oxidant species (ROS). Increased ROS could potentially lead to cardiac remodeling and heart failure (190, 191). Therefore, excess activation of SERCA is not necessarily a

positive for healthy cardiac function. Perhaps it would be preferable to find therapies that only mildly activate SERCA to treat heart failure and work with its endogenous regulatory mechanisms. These considerations make the insights we provide into how SERCA activity is dynamically tuned in the heart all the more important.

Based on these considerations, DWORF gene therapy may be a favorable route for SERCA activation. In addition to activating SERCA at baseline, our results indicate that DWORF binding to SERCA increases dynamically in response to cellular Ca^{2+} elevations (Fig. 10). This means that a proportion of the SERCA-activating potential of DWORF is reserved for cardiac systole. This would conserve ATP resources by only transiently activating SERCA when cytosolic Ca^{2+} is high and Ca^{2+} transport is most needed.

Potential Preventative Approaches for PLB-associated Cardiomyopathy

In Chapter Five, we found that two PLB mutations associated with dilated cardiomyopathy, R14del and R9C, decrease PLB regulatory binding to SERCA by chronically stabilizing of PLB pentamers (Fig. 15). This loss of SERCA regulation by PLB leads to the expected negative consequences of over-activation of SERCA: excess ATP consumption, increased ROS production, and maladaptive remodeling of the heart to cause heart failure in human carriers (190, 191). Interestingly, a recent study found that ROS inhibition with N-acetyl-L-cysteine was able to prevent cardiac remodeling in a zebrafish model of R9C-PLB-associated heart failure (139). Since our results indicate that R9C and R14del share a similar pathogenic mechanism (reducing PLB inhibitory function), these preclinical successes may suggest that ROS inhibition may be an appealing strategy to treat these PLB-associated forms of heart failure. This is

especially critical for the R14del-associated cardiomyopathy which does not respond to conventional therapies (153) and is incredibly prevalent in the Netherlands, accounting account for up to 15% of dilated cardiomyopathy among Dutch patients (138). If future therapies could prevent maladaptive remodeling to heart failure, this could be life changing for the families that genetically inherit these mutations.

Final Thoughts

In this study, we investigated how the regulation of cardiac SERCA by endogenous membrane micropeptides is adjusted to meet changing physiological demands. Particularly, our results indicate that dynamic fraction of these regulatory interactions dynamically shift in response to cellular Ca^{2+} signaling (Fig. 10). This adjusts SERCA regulation between phases of the cardiac cycle and as heart rates accelerate between rest and exercise (Fig. 13). Additionally, pathogenic mutations, like R14del-PLB, that impact the rates of exchange can blunt the responsiveness of Ca^{2+} handling to changing demands (Fig. 17). Through studying how SERCA conformation changes impact the energetics of PLB-SERCA complex binding, we also uncovered the intrinsic mechanism by which PLB regulates SERCA (Fig. 19). Overall, these insights reveal a dynamic SERCA regulatory network that can be physiologically and pharmacologically tuned. The wide variety of mechanisms revealed by this investigation provide many favorable avenues that researchers and clinicians may pursue to use SERCA as a therapeutic target to treat heart failure.

APPENDIX A
INTRODUCTION TO THE APPENDICES

These appendices provide supplementary information and data in support of the projects described within the main chapters of this dissertation, as well as data acquired in support of other published collaborator manuscripts that were not directly related to the main chapters of this work. At the beginning of each appendix, the manuscript title and authors will be listed (with a citation if published), and either an abstract or a summary of the work will be provided. If the data here are associated with a published manuscript and the data provided did not make it into the published work, it will be listed in the addendum at the end of the appendix.

APPENDIX B

SUPPLEMENTARY INFORMATION FOR CHAPTER FOUR

Title and Authors of Associated Work:INHIBITORY AND STIMULATORY MICROPEPTIDES PREFERENTIALLY BIND TO
DIFFERENT CONFORMATIONS OF THE CARDIAC CALCIUM PUMP

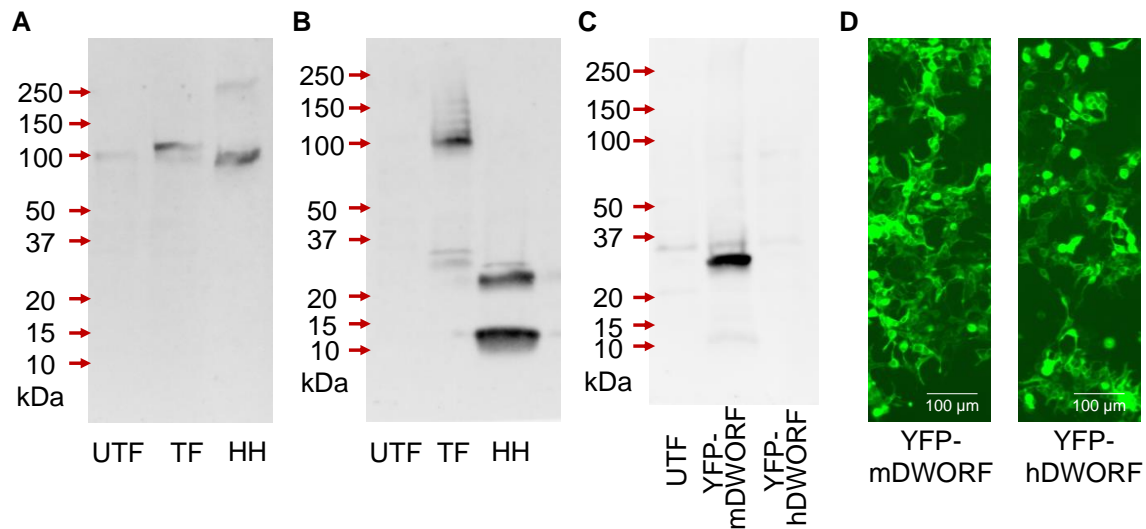
Sean R. Cleary, Xuan Fang, Ellen E. Cho, Marsha P. Pribadi, Jaroslava Seflova,
Jordan R. Beach, Peter M. Kekenes-Huskey, and Seth L. Robia
Department of Cell and Molecular Physiology, Loyola University Chicago, Maywood, IL

Inhibitory and stimulatory micropeptides preferentially bind to different conformations of the cardiac calcium pump. *J Biol Chem* 298, 102060 (2022).

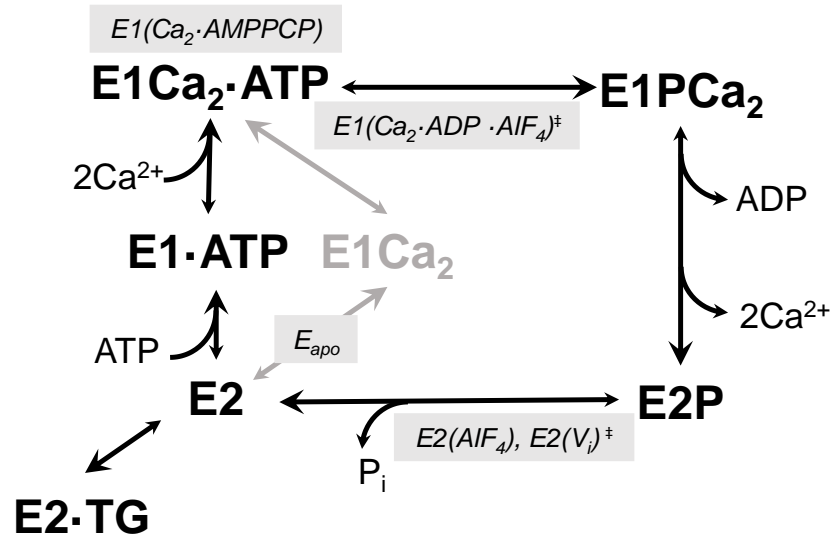
Appendix B: Abstract

The ATP-dependent ion pump SERCA sequesters Ca^{2+} in the endoplasmic reticulum to establish a reservoir for cell signaling. Because of its central importance in physiology, the activity of this transporter is tightly controlled via direct interactions with tissue-specific regulatory micropeptides that tune SERCA function to match changing physiological conditions. In the heart, the micropeptide phospholamban (PLB) inhibits SERCA, while dwarf open reading frame (DWORF) stimulates SERCA. These competing interactions determine cardiac performance by modulating the amplitude of Ca^{2+} signals that drive the contraction/relaxation cycle. We hypothesized the functions of these peptides may relate to their reciprocal preferences for SERCA binding; SERCA binds PLB more avidly at low cytoplasmic $[\text{Ca}^{2+}]$ but binds DWORF better when $[\text{Ca}^{2+}]$ is high. In the present study, we demonstrated this opposing Ca^{2+} sensitivity is due to preferential binding of DWORF and PLB to different intermediate states that SERCA samples during the Ca^{2+} transport cycle. We show PLB binds best to the SERCA E1-ATP state, which prevails at low $[\text{Ca}^{2+}]$. In contrast, DWORF binds most avidly to E1P and E2P states that are more populated when Ca^{2+} is elevated. Moreover, FRET microscopy revealed dynamic shifts in SERCA-micropeptide binding equilibria during

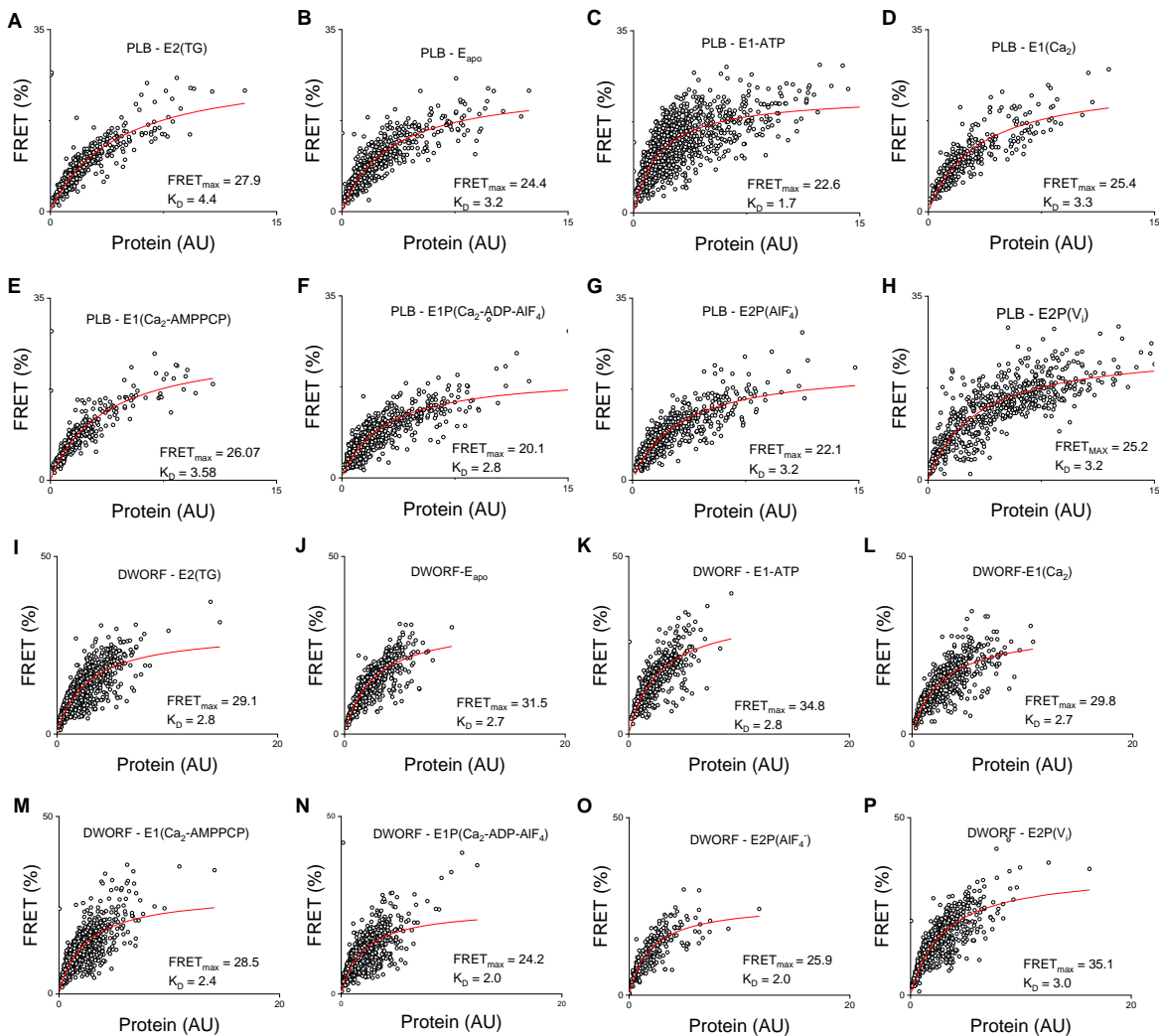
cellular Ca^{2+} elevations. In a computational model of these regulatory interactions under different heart rates, we found DWORF exaggerates changes in PLB-SERCA binding during the cardiac cycle. These results suggest a mechanistic basis for inhibitory versus stimulatory micropeptide function, as well as a new role for DWORF as a modulator of dynamic oscillations of PLB-SERCA regulatory interactions.



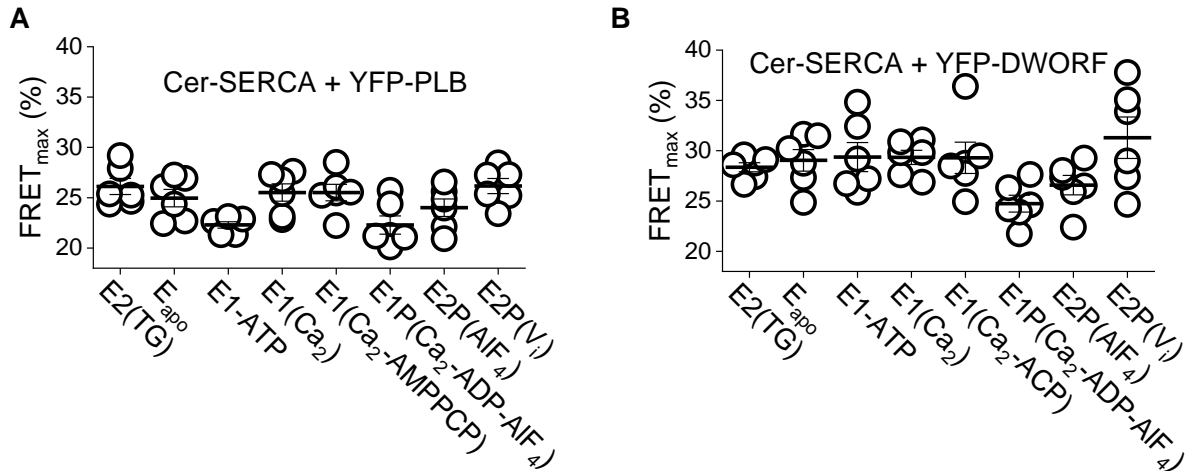
Appendix Figure B.1. Western blot analysis **A**, Anti-SERCA antibody revealed endogenous SERCA2b in untransfected cells (UTF), Cer-SERCA2a in transfected cells (TF), and SERCA2a in human heart (HH) samples. **B**, Anti-PLB antibody did not detect endogenous PLB in untransfected (UTF) cells, but showed the expected mobilities of YFP-PLB in transfected cells (TF) and PLB in the human heart (HH) sample. **C**, Anti-mouse DWORF antibody was only reactive to the mouse sequence (YFP-mDWORF), and did not bind to the human protein (YFP-hDWORF). **D**, Fluorescence microscopy showed that both mouse and human DWORF expressed well.



Appendix Figure B.2. Post-Albers cycle with biochemically stabilized states of SERCA. Ligand-free SERCA (pH 7) is in the E_{apo} state – a state in pH-dependent dynamic equilibrium between E2 and E1 states where substrate binding sites face the ER lumen or the cytosol respectively (6). The SERCA inhibitor, thapsigargin (TG), stabilizes a dead-end E2 conformation (1IWO) (8). Saturating concentrations of ATP or Ca²⁺ stabilize E1 conformations of the pump (9, 10). The structural analog of E1Ca₂-ATP where both substrates are bound is stabilized with Ca²⁺ and a non-hydrolysable ATP-analog, AMPPCP (PDB: 1T5S) (12). The ADP-bound transition state following ATP-hydrolysis is stabilized with saturating concentrations of Ca²⁺, ADP, and the phosphate analog, AIF₄ (PDB: 2ZBD) (13). A low Ca²⁺ buffer containing either AIF₄ or the SERCA inhibitor orthovanadate (V_i) stabilize a transitional analog of the dephosphorylating E2P state (PDB: 3N5K, 5A3Q) (14, 15). ‡ indicates transition states.



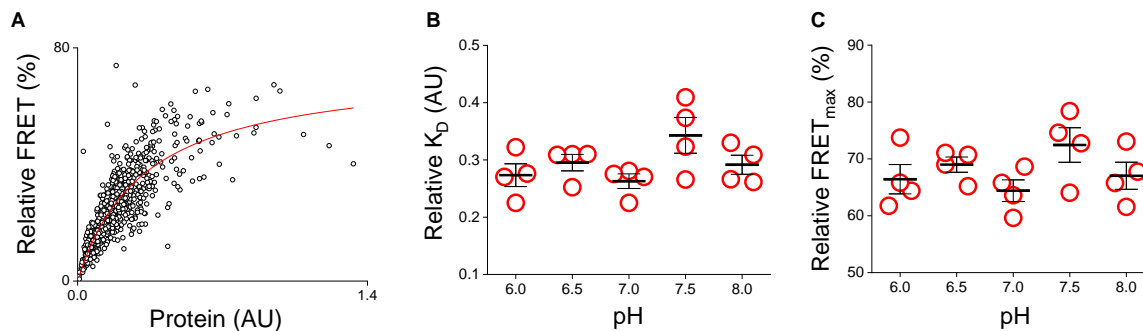
Appendix Figure B.3. Representative FRET-based binding curves for PLB and DWORF interactions with ligand-stabilized enzymatic states of SERCA. **A-H**, Representative binding curves based on FRET measurements between Cer-SERCA and YFP-PLB FRET pairs. **I-P**, Representative binding curves based on FRET measurements between Cer-SERCA and YFP-DWORF FRET pairs.



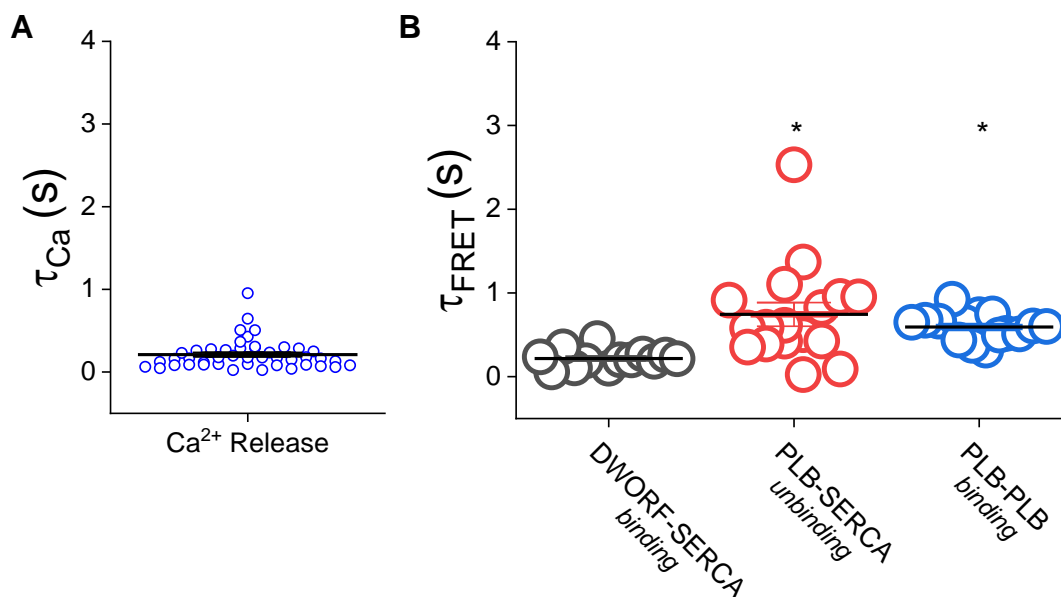
Appendix Figure B.4. FRET_{max} values for PLB and DWORF regulatory complexes with ligand-stabilized enzymatic states of SERCA with lines representing mean \pm SEM ($n=6$). Data are derived from hyperbolic fits of FRET data plotted over a range of YFP-tagged micropeptide protein concentration (See representative curves in Appendix Fig. B.2).

Appendix Table B.1. P values comparing differential PLB (above) and DWORF (below) dissociation constants for binding SERCA conformation states. Data were analyzed by 1-way ANOVA with Tukey's *post-hoc* test ($p < 0.05 = *$).

PLB-SERCA Conformation K_D 1-way ANOVA with Tukey's post-hoc							
	E2(TG)	E _{apo}	E1-ATP	E1(Ca ₂)	E1(Ca ₂ -AMPPCP)	E1P(Ca ₂ -ADP-AIF ₄)	E2P(AIF ₄)
E2P(V _i)	5.14×10^{-2}	1	$7.07 \times 10^{-6*}$	1	1	1	0.67
E2P(AIF ₄)	$1.86 \times 10^{-2*}$	1	$2.54 \times 10^{-5*}$	1	1	1	0.89
E1P(Ca ₂ -ADP-AIF ₄)	$3.93 \times 10^{-4*}$	0.97	$1.57 \times 10^{-3*}$	0.59	0.52		
E1(Ca ₂ -ACP)	9.13×10^{-2}	0.98	$3.33 \times 10^{-6*}$	1			
E1(Ca ₂)	6.90×10^{-2}	0.99	$4.76 \times 10^{-6*}$				
E1-ATP	$1.96 \times 10^{-8*}$	$6.63 \times 10^{-5*}$					
E _{apo}	$8.14 \times 10^{-3*}$						
DWORF-SERCA Conformation K_D 1-way ANOVA with Tukey's post-hoc							
	E2(TG)	E _{apo}	E1-ATP	E1(Ca ₂)	E1(Ca ₂ -AMPPCP)	E1P(Ca ₂ -ADP-AIF ₄)	E2P(AIF ₄)
E2P(V _i)	1	1	1	1	1	1	0.39
E2P(AIF ₄)	0.73	0.95	0.95	0.88	0.86	1	0.71
E1P(Ca ₂ -ADP-AIF ₄)	0.41	0.73	0.73	0.59	0.56		
E1(Ca ₂ -ACP)	1	1	1	1			
E1(Ca ₂)	1	1	1				
E1-ATP	1	1					
E _{apo}	1						



Appendix Figure B.5. PLB binding preference for E2-ATP and E1-ATP substates of the ATP bound state of SERCA was assessed by measuring Cer-SERCA – TagRFP-PLB FRET in a buffer containing ATP (3 mM) at a range of pH from 6-8 (See *Chapter 3*). Increasingly acidic conditions protonate SERCA substrate binding sites, stabilizing E2 conformations, whereas E1 is favored at alkaline pH (6). **A**, Representative FRET-based binding curve for TagRFP-PLB interacting with ATP-bound Cer-SERCA at pH 7.0. **B**, Relative K_D values of the PLB-SERCA regulatory complex measured at a range of pH from 6-8, with lines representing mean \pm SEM ($n=4$). We saw no change in PLB-SERCA K_D in this range, indicating no discernible preference of PLB for E2-ATP or E1-ATP states. **C**, Relative FRET_{max} values of the PLB-SERCA regulatory complex measured at a range of pH from 6-8, with lines representing mean \pm SEM ($n=4$).



Appendix Figure B.6. PLB pentamer formation during Ca²⁺ elevations is delayed by the time course of PLB-SERCA unbinding. **A**, Raw time constant (τ) values for Ca²⁺ release derived from single exponential decay fits of increases in X-rhod-1 fluorescence. **B**, Raw τ values for SERCA and micropeptide binding processes derived from single exponential decay fits of FRET ratio changes associated with Ca²⁺ release with lines representing mean \pm SEM. Differences determined by one-way ANOVA with Dunn's *post-hoc* test (* = $p < 0.05$, see Table B.3 for complete statistical analysis). Data are shown in Fig. 11F as the FRET latency quantified by the difference between the τ of FRET ratio changes and the τ of their corresponding Ca²⁺ uptake event.

Appendix Table B.2. Time constants (τ) quantified for regulatory binding processes associated with Ca^{2+} release. Time constant values are reported as mean \pm SEM.

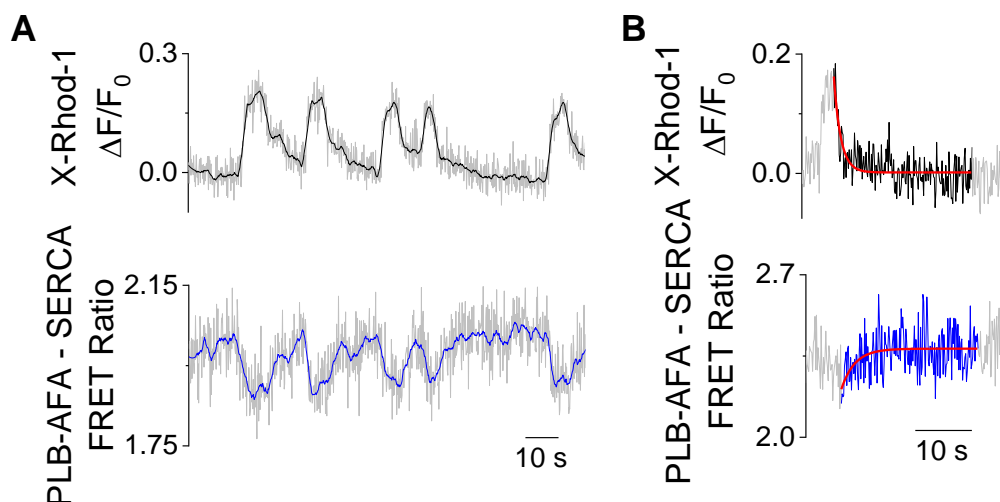
Apparent τ (Mean \pm SEM)	
Process	τ (s)
DWOLF – SERCA (<i>binding</i>)	0.22 \pm 0.03
PLB – SERCA (<i>unbinding</i>)	0.74 \pm 0.14
PLB – PLB (<i>binding</i>)	0.59 \pm 0.04
Ca^{2+} Release	0.21 \pm 0.03

Appendix Table B.3. *P* values comparing differences in time constants (τ) for SERCA/micropeptide binding/unbinding processes associated with Ca^{2+} release analyzed by 1-way ANOVA with Dunn's *post-hoc* test ($p < 0.05 = *$). See Fig. B.6 and Table B.2 for corresponding summary data.

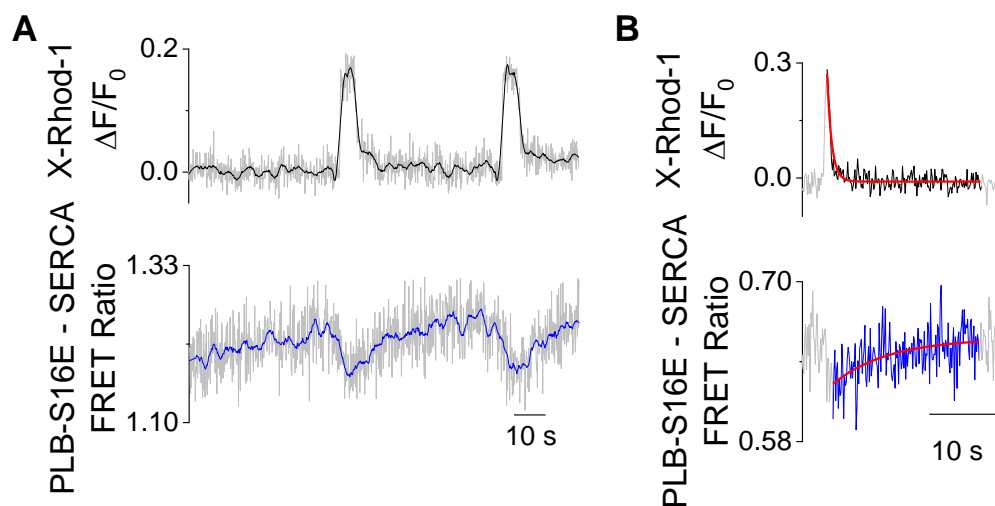
SERCA/micropeptide binding/unbinding processes analyzed by 1-way ANOVA with Dunn's post-hoc			
	DWOLF-SERCA (<i>binding</i>)	PLB-SERCA (<i>unbinding</i>)	PLB-PLB (<i>binding</i>)
Ca^{2+} Release		1	$3.84 \times 10^{-8*}$
PLB-PLB (<i>binding</i>)	$5.79 \times 10^{-3*}$		0.62
PLB-SERCA (<i>unbinding</i>)	$2.45 \times 10^{-5*}$		$1.74 \times 10^{-4*}$

Appendix Table B.4. *P* values comparing FRET latency $\Delta\tau$ ($\tau_{\text{FRET}} - \tau_{\text{Ca Release}}$) differences between groups analyzed by 1-way ANOVA with Dunn's *post-hoc* test ($p < 0.05 = *$). See Fig. 11F for corresponding summary data.

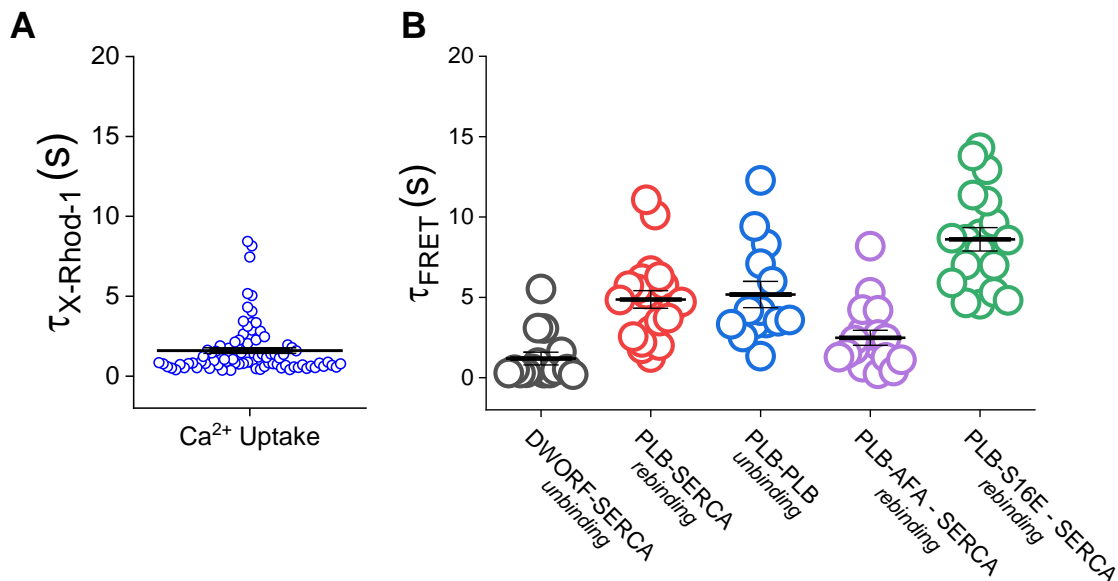
FRET Latency $\Delta\tau$ ($\tau_{\text{FRET}} - \tau_{\text{Ca Release}}$) 1-way ANOVA with Dunn's post-hoc test		
	PLB-SERCA (<i>unbinding</i>)	PLB-PLB (<i>binding</i>)
DWOLF-SERCA (<i>binding</i>)	$4.06 \times 10^{-3*}$	$1.08 \times 10^{-3*}$
PLB-PLB (<i>binding</i>)		0.92



Appendix Figure B.7. Representative data for PLB-AFA - SERCA FRET ratio changes measured in response to intracellular Ca^{2+} elevations. **A**, Confocal microscopy quantification of cytosolic Ca^{2+} measured by X-Rhod-1 (*grey + black smoothed trendline*) with simultaneous measurement of changes in PLB-AFA - SERCA FRET (*grey + blue smoothed trendline*). **B**, Representative single exponential decay fit of PLB-AFA – SERCA rebinding during Ca^{2+} uptake.



Appendix Figure B.8. Representative data for PLB-S16E - SERCA FRET ratio changes measured in response to intracellular Ca^{2+} elevations. **A**, Confocal microscopy quantification of cytosolic Ca^{2+} measured by X-Rhod-1 (*grey + black smoothed trendline*) with simultaneous measurement of changes in PLB-S16E - SERCA FRET (*grey + blue smoothed trendline*). **B**, Representative single exponential decay fit of PLB-S16E – SERCA rebinding during Ca^{2+} uptake.



Appendix Figure B.9. Time constants (τ) quantified for regulatory binding processes associated with Ca²⁺ uptake with lines representing mean \pm SEM. **A**, Time constant values for Ca²⁺ uptake derived from single exponential decay fits of decreases in X-rhod-1 fluorescence. **B**, Raw time constant values for SERCA and micropeptide binding processes derived from single exponential decay fits of FRET ratio changes associated with Ca²⁺ uptake measured by X-Rhod-1 fluorescence. Data are shown in Fig. 12E as the FRET latency quantified by the difference between the τ of FRET ratio changes and the τ of their corresponding Ca²⁺ uptake event. See Table B6 for complete statistical analysis.

Appendix Table B.5. Time constants (τ) of binding processes associated with Ca^{2+} uptake measured by X-Rhod-1 fluorescence. Time constant values are reported as mean \pm SEM.

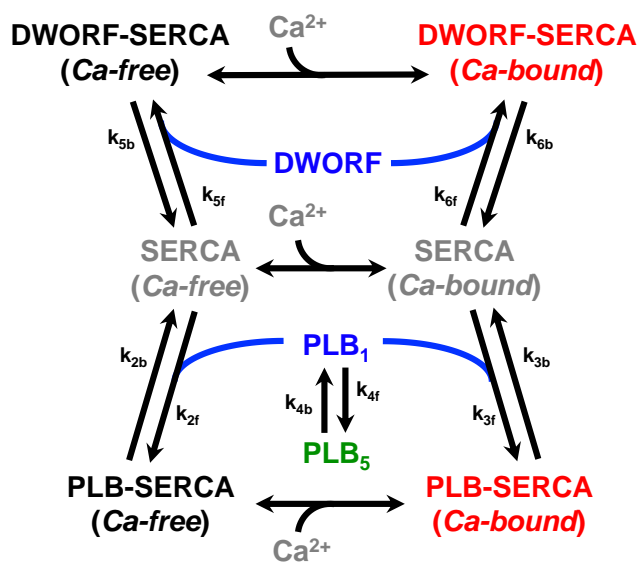
Apparent τ (Mean \pm SEM)	
Process	τ (s)
DWOLF – SERCA (<i>unbinding</i>)	1.2 \pm 0.4
PLB – SERCA (<i>rebinding</i>)	4.9 \pm 0.6
PLB – PLB (<i>unbinding</i>)	5.2 \pm 0.8
PLB-AFA – SERCA (<i>rebinding</i>)	2.5 \pm 0.5
PLB-S16E – SERCA (<i>rebinding</i>)	8.6 \pm 0.7
Ca^{2+} Uptake	1.6 \pm 0.2

Appendix Table B.6. *P* values comparing differences in time constants (τ) for SERCA-micropeptide binding/unbinding processes analyzed by 1-way ANOVA with Dunn's *post-hoc* test ($p < 0.05 = *$). See Fig. B.9 and Table B.5 for corresponding summary data.

SERCA/Micropeptide binding/unbinding τ 1-way ANOVA with Dunn's post-hoc					
	DWOLF-SERCA (<i>unbinding</i>)	PLB-SERCA (<i>rebinding</i>)	PLB-PLB (<i>unbinding</i>)	PLB-S16E - SERCA (<i>rebinding</i>)	PLB-AFA – SERCA (<i>rebinding</i>)
Ca^{2+} Uptake	1	2.38 x 10 ^{-8*}	2.81 x 10 ^{-7*}	<1 x 10 ^{-10*}	0.81
PLB-AFA - SERCA (<i>rebinding</i>)	0.72	7.95 x 10 ^{-3*}	6.30 x 10 ^{-3*}	<1 x 10 ^{-10*}	
PLB-S16E - SERCA (<i>rebinding</i>)	<1 x 10 ^{-10*}	1.64 x 10 ^{-6*}	1.30 x 10 ^{-4*}		
PLB - PLB (<i>unbinding</i>)	1.35 x 10 ^{-5*}	1			
PLB - SERCA (<i>rebinding</i>)	9.79 x 10 ^{-6*}				

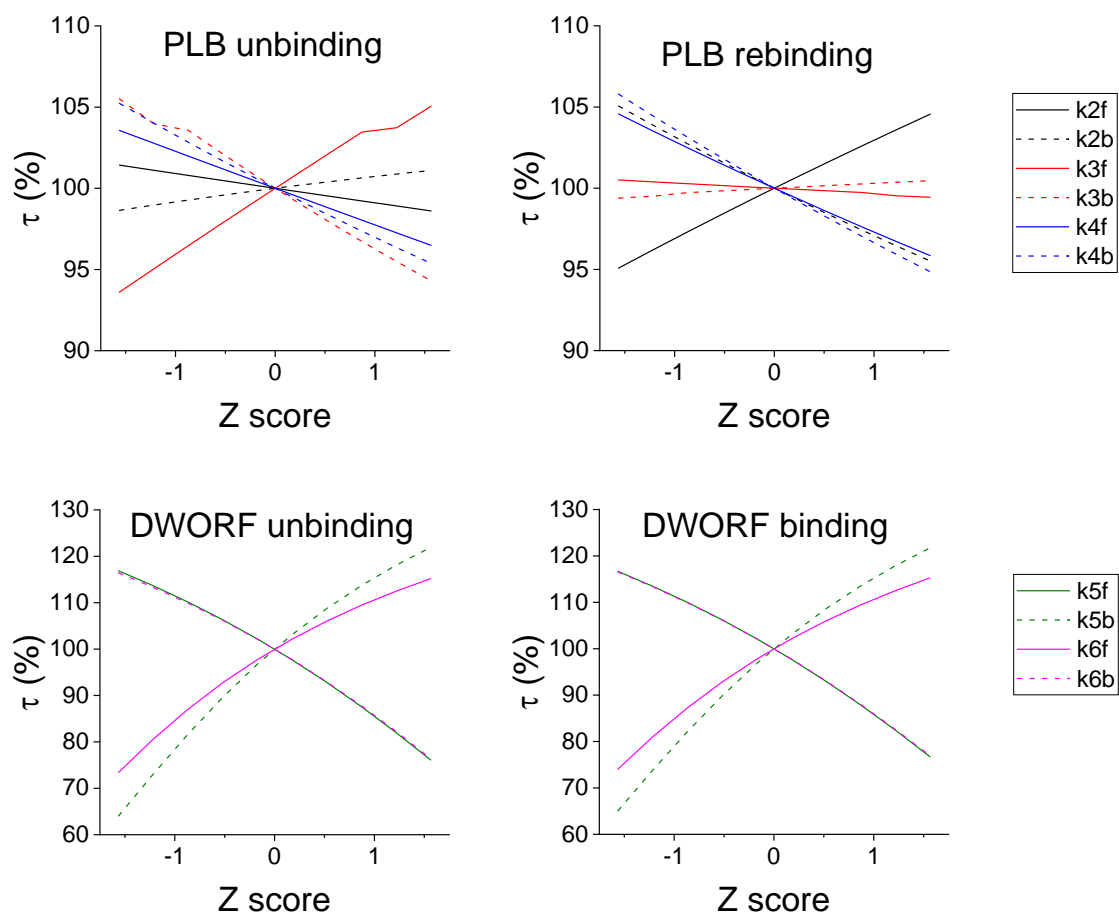
Appendix Table B.7. *P* values comparing FRET latency $\Delta\tau$ ($\tau_{\text{FRET}} - \tau_{\text{Ca Uptake}}$) differences between groups analyzed by 1-way ANOVA with Dunn's *post-hoc* test ($p < 0.05 = *$). See Fig. 12E for corresponding summary data.

FRET Latency $\Delta\tau$ ($\tau_{\text{FRET}} - \tau_{\text{Ca Uptake}}$) 1-way ANOVA with Dunn's post-hoc test				
	DWOLF-SERCA (<i>unbinding</i>)	PLB-SERCA (<i>rebinding</i>)	PLB-PLB (<i>unbinding</i>)	PLB-S16E - SERCA (<i>rebinding</i>)
PLB-AFA - SERCA (<i>rebinding</i>)	0.85	2.24 x 10 ^{-2*}	1.73 x 10 ^{-3*}	3.48 x 10 ^{-8*}
PLB-S16E - SERCA (<i>rebinding</i>)	2.96 x 10 ^{-10*}	3.59 x 10 ^{-3*}	0.23	
PLB-PLB (<i>unbinding</i>)	2.45 x 10 ^{-5*}		0.95	
PLB-SERCA (<i>rebinding</i>)	3.03 x 10 ^{-4*}			



Parameter	Value (s ⁻¹)	SEM (s ⁻¹)
k_{2f}	8.1×10^3	5.8×10^2
k_{2b}	1.1×10^2	3.3×10^0
k_{3f}	5.6×10^3	6.7×10^2
k_{3b}	1.7×10^2	3.2×10^1
k_{4f}	1.0×10^1	9.0×10^{-1}
k_{4b}	7.9×10^{-2}	1.8×10^{-2}
k_{5f}	3.5×10^1	7.5×10^0
k_{5b}	1.9×10^1	8.5×10^0
k_{6f}	1.3×10^4	1.4×10^3
k_{6b}	4.8×10^3	1.8×10^3

Appendix Figure B.10. A reaction diagram indicating the kinetic parameters derived from experimental measurements. Mean kinetic parameters of PLB -SERCA and -pentamer (PLB₅) binding dynamics were fit from PLB-SERCA FRET experiments, and mean kinetic parameters of DWORF-SERCA binding dynamics were fit from DWORF-SERCA FRET experiments (see Chapter 3).



Appendix Figure B.11. Parameter sensitivity analysis describing how simulated PLB-SERCA and DWORF-SERCA binding dynamics are sensitive to changes in experimentally obtained parameters.

Supplementary Methods

To simulate the Ca^{2+} transient, we used the following equations:

$$\text{Ca}(t) = \begin{cases} 0 & t < t_{init} \\ \frac{(t-t_{init})^n}{K+(t-t_{init})^n} & t_{init} < t < t_{init} + t_{setpoint} \\ \frac{K}{K+(t-t_{init})^n} & t > t_{init} + t_{setpoint} \end{cases} \quad \text{eq. B1}$$

where t_{init} is the time duration of basal Ca^{2+} , $t_{setpoint}$ is the time duration of peak Ca^{2+} , and K and n are Ca^{2+} transient shape parameters.

As a simplification, we assume that SERCA exists in two ensembles: diastolic and systolic. Furthermore, these two ensembles distribute following the Ca^{2+} transient, which can be described by the following equations:

$$SERCA_{dia,tot} = SERCA_{tot} * \frac{Ca(t)}{Ca_{max}} \quad \text{eq. B2}$$

$$SERCA_{sys,tot} = SERCA_{tot} - SERCA_{sys} \quad \text{eq. B3}$$

where $SERCA_{dia,tot}$ is the diastolic SERCA ensemble, $SERCA_{sys,tot}$ is the systolic SERCA ensemble, and $SERCA_{tot}$ is the total amount of SERCA.

The following ordinary differential equations were used to describe the models of PLB-SERCA and DWORF-SERCA binding.

PLB-SERCA

$$\frac{dPLB \cdot SERCA_{dia}}{dt} = k_{2f} * PLB_1 * SERCA_{dia} - k_{2b} * PLB \cdot SERCA_{dia} \quad \text{eq. B4}$$

$$\frac{dPLB \cdot SERCA_{sys}}{dt} = k_{3f} * PLB_1 * SERCA_{sys} - k_{3b} * PLB \cdot SERCA_{sys} \quad \text{eq. B5}$$

$$\frac{dPLB_5}{dt} = k_{4f} * PLB_1 - k_{4b} * PLB_5 \quad \text{eq. B6}$$

DWORF-SERCA

$$\frac{dDWORF \cdot SERCA_{dia}}{dt} = k_{5f} * DWORF * SERCA_{dia} - k_{5b} * DWORF \cdot SERCA_{dia} \quad \text{eq. B7}$$

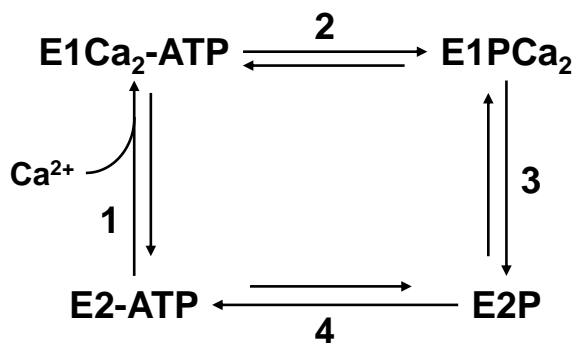
$$\frac{dDWORF \cdot SERCA_{sys}}{dt} = k_{6f} * DWORF * SERCA_{sys} - k_{6b} * DWORF \cdot SERCA_{sys} \quad \text{eq. B8}$$

where $SERCA_{dia}$ and $SERCA_{sys}$ are free diastolic and systolic SERCA, $PLB \cdot SERCA_{dia}$ and $PLB \cdot SERCA_{sys}$ are diastolic and systolic PLB-SERCA complexes, $DWORF \cdot SERCA_{dia}$ and $DWORF \cdot SERCA_{sys}$ are diastolic and systolic DWORF-SERCA complexes, PLB_1 is monomeric PLB, PLB_5 is pentameric PLB, and $DWORF$ is free DWORF.

Appendix B: Addendum

The following were not published together with the associated manuscript but provide information and data in support of the main arguments of the paper.

Modeling SERCA Cycle Kinetics



Appendix Figure B.12. A Schematic Diagram of the 4-State Kinetic Model Designed to Simulate SERCA Conformation Cycling During Intracellular Ca^{2+} Elevations

Because SERCA is a Ca^{2+} transporter, its conformational poise changes as a function of cytosolic Ca^{2+} concentration. When cytosolic $[\text{Ca}^{2+}]$ is low during diastole, SERCA predominantly resides in the ATP-bound state, E1-ATP, waiting for Ca^{2+} to bind. During intracellular Ca^{2+} elevations, SERCA samples all the intermediate states of its catalytic cycle, but these states are not equally populated. Rather, SERCA accumulates in intermediate states preceding steps that rate-limit the overall turnover rate of the cycle. In order to visualize which states of SERCA predominate during enzymatic cycling, we created a kinetic model to simulate the major transitions of the cycle. We considered the kinetics of transitions between 4 major states of the Post-Albers cycle (47): E2, E1, E1P and E2P (labeled as E2-ATP, E1Ca₂-ATP, E1PCa₂, and E2P, respectively, in the schematic diagram in Fig. B.12). The model describes the

transitions between these states with the set of ordinary differential equations (Table B.8).

Appendix Table B.8. Ordinary Differential Equations for the SERCA State Model

Intermediate State	Ordinary Differential Equation ($\frac{dy}{dt}$)
E2-ATP	$\frac{dE2-ATP}{dt} = -k_1(E2-ATP)^*(1+(0.85/2)^2)^{-1} - k_{-4}(E2-ATP) + k_4(E2P) + k_{-1}(E1Ca_2-ATP)$
E1Ca ₂ -ATP	$\frac{dE1Ca_2-ATP}{dt} = -k_2(E1Ca_2-ATP) - k_{-1}(E1Ca_2-ATP) + k_1(E2-ATP)^*(1+(0.85/2)^2)^{-1} + k_2(E1PCa_2)$
E1PCa ₂	$\frac{dE1PCa_2}{dt} = -k_3(E1PCa_2) - k_2(E1PCa_2) + k_2(E1Ca_2-ATP) + k_3(E2P)$
E2P	$\frac{dE2P}{dt} = -k_4(E2P) - k_3(E2P) + k_3(E1PCa_2) + k_{-4}(E2-ATP)$

In order to simplify the reaction scheme, some steps are assumed to be in rapid-equilibrium. For example, the binding of ATP to E2-SERCA is often considered to be rapid under physiological conditions because it is always present at very high, saturating concentrations in the cytoplasm (57). The rate constants used in this model were based on stopped-flow measurements of SERCA1a purified from rabbit skeletal muscle (Table B.9) (55-57, 60-63). The values for the forward rate constants k_1 , k_2 , and k_3 were taken from a by Sorenson and colleagues where the kinetics of these transitions were measured at room temperature (60). The value of the forward rate constant for k_4 was estimated under similar conditions at room temperature in a separate study (55). The reverse rates were assigned very small values in consideration of the virtually irreversible nature of these reactions under the simulated conditions, where Ca^{2+} is high and Mg^{2+} , ATP, and K^+ are saturating, ~pH 7.0 (61, 63). The forward rate constant, k_1 , was assigned a pseudo second order rate that was dependent on the addition of Ca^{2+} to the model. The results of a simulation of SERCA cycling in response to an increase in Ca^{2+} is shown in Chapter 2 (Fig. 3B).

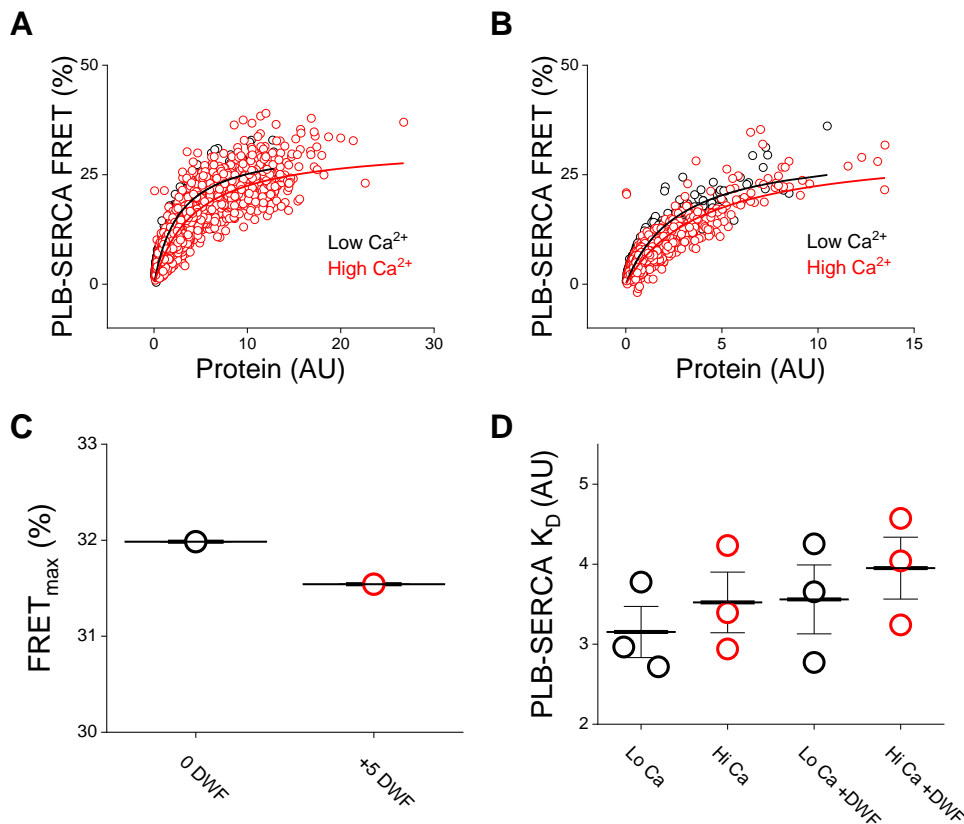
Table B.9. Kinetic Parameters Used to Simulate SERCA cycle kinetics.

Partial reaction	Rate constant (s ⁻¹ or mol/liter/s)
k_1 / k_{-1}	25 / 1E-3
k_2 / k_{-2}	35 / 1E-3
k_3 / k_{-3}	5 / 1E-3
k_4 / k_{-4}	60 / 1E-3

PLB Binding Affinity is Additively Reduced By Ca²⁺ and DWORF Competition

Taken together, the data provided in Chapter 4: Figures 8 and 9 suggest that PLB prefers to bind to SERCA conformations that predominate in low Ca²⁺ and DWORF prefers Ca²⁺ pump conformations that prevail in high Ca²⁺. To demonstrate the impact of this Ca²⁺-dependent competition between PLB and DWORF on PLB-SERCA binding, we measured the impact of co-expressing unlabeled DWORF on the Ca²⁺-dependent shift in PLB-SERCA affinity measured by FRET-based binding curves. PLB-SERCA binding affinity was reduced in elevated Ca²⁺, indicated by the right shifts of the binding curves in Figure B.13A and B between low (*black*) and high Ca²⁺ (*red*), regardless of whether DWORF was present or not. Hyperbolic fits of the data revealed the FRET_{max} (inversely related to the relative distance of the donor and acceptor fluorescent tags when PLB and SERCA are bound in complex) and K_D (inversely related to the relative affinity of PLB-SERCA binding) for these conditions. Expressing unlabeled DWORF 1:1 had no effect on the maximum FRET efficiency (Fig B.13C), indicating no change in the distance of the PLB-SERCA complex. Interestingly, DWORF co-expression did reduce the affinity of PLB-SERCA binding on its own and in an additive manor with elevated

Ca²⁺, indicated the incremental increases in the K_D values with high Ca²⁺ and DWORF co-expression shown in Figure B.13D.



Appendix Figure B.13. Elevated Ca²⁺ and DWORF Co-expression Additively Reduce PLB Affinity for SERCA. **A**, Representative binding curves showing that PLB-SERCA binding affinity is reduced in elevated Ca²⁺ with no co-expression of DWORF. **B**, Representative binding curves showing that PLB-SERCA binding affinity is reduced in elevated Ca²⁺ with DWORF co-expressed 1:1 with PLB. **C-D**, FRET_{max} and K_D values fit from global-fitting the data from 3 independent experiments sharing FRET max.

APPENDIX C

PLB AND DWORF COMPETE TO BIND A COMMON REGULATORY SITE ON SERCA

Title and Authors of Associated Work:**MICROPEPTIDE HETERO-OLIGOMERIZATION ADDS COMPLEXITY TO THE
CALCIUM PUMP REGULATORY NETWORK**

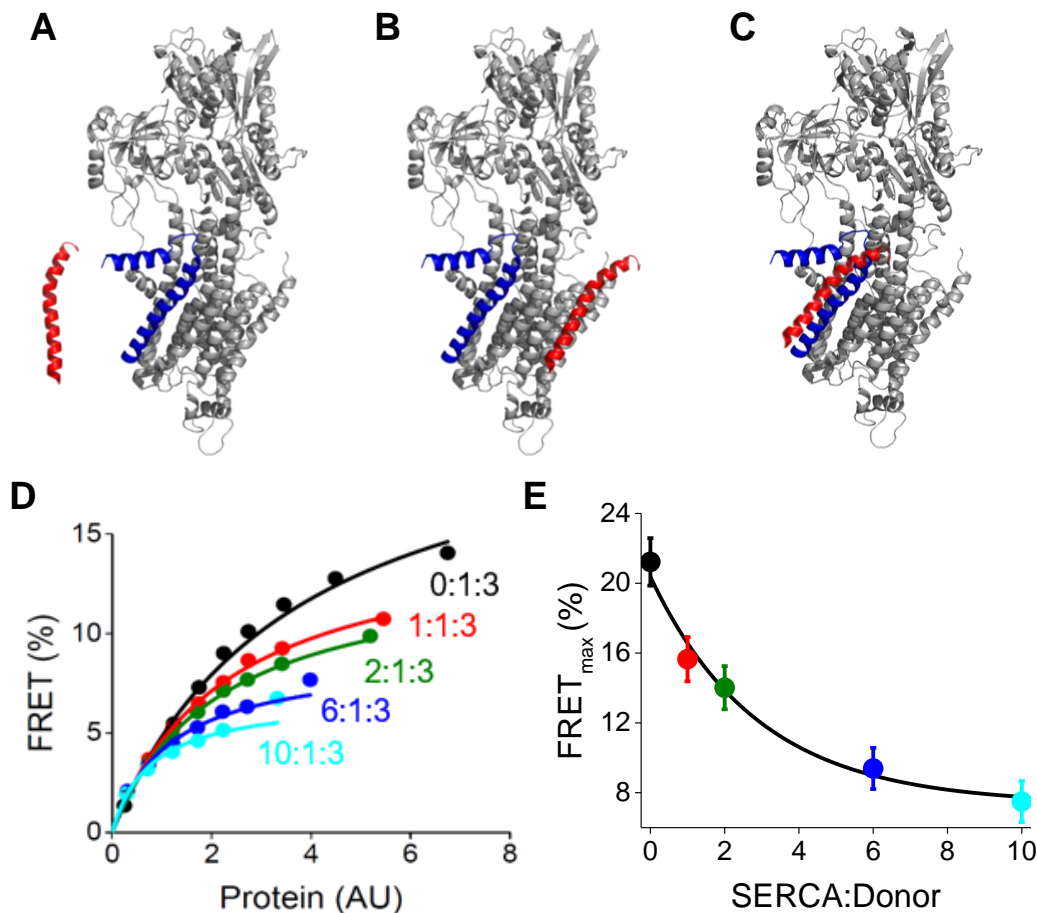
Taylor A. Phillips, Garrett T. Hauck, Marsha P. Pribadi, Ellen E. Cho, **Sean R. Cleary**,
and Seth L. Robia

Department of Cell and Molecular Physiology, Loyola University Chicago, Maywood, IL

Micropeptide hetero-oligomerization adds complexity to the calcium pump regulatory network. *Biophys J* 75(3):434-42, (2023).

Appendix C: Summary

When unbound from the Ca²⁺ pump, SERCA regulatory micropeptides can interact with themselves in homo-oligomeric complexes. For example, PLB monomers freed from their interaction with SERCA assemble into highly stable homo-pentamers. Here, we evaluated whether different micropeptides, such as PLB or DWORF, can interact with each other. These hetero-oligomeric interactions may further limit the bioavailability of micropeptides free to bind and regulate SERCA. Specifically, PLB and DWORF interacted in a heterodimer with each other with good affinity, albeit lower than the homo-oligomeric affinity of PLB pentamers. Increasing expression of SERCA decreased PLB-DWORF hetero-oligomerization, indicating that SERCA-micropeptide interactions compete with micropeptide-micropeptide interactions.



Appendix Figure C.1. PLB and DWORF Compete to Bind a Common Regulatory Cleft on SERCA. **A**, SERCA binds to PLB (*blue*) or DWORF (*red*) but not both simultaneously. **B**, SERCA binds PLB and DWORF at distinct binding sites. **C**, SERCA binds a PLB-DWORF hetero-oligomer. **D**, FRET from Cer-DWORF to YFP-PLB with increasing coexpression of SERCA. Labels indicate the ratio of competitor:donor:acceptor. Data represent the mean. The average Y SE for each point is 0.04%. **E**, FRET_{max} decreased with increasing expression of SERCA, consistent with depolymerization of the PLB-DWORF hetero-oligomeric complex. Data are presented as mean \pm SE.

We have previously shown that PLB and DWORF individually interact with SERCA as monomers (92) and it has been proposed that they compete for a common site within SERCA (98) (Fig. C.1A). Still, the possibility remains that PLB and DWORF bind to distinct sites on SERCA (Fig. C.1B). In the associated manuscript, we also observed that PLB and DWORF can interact with each other in a heterodimer.

Therefore, it is also possible the PLB-DWORF heterodimer may interact with SERCA (Fig. C.1C). To determine how the micropeptide-micropeptide and SERCA-micropeptide binding equilibria impact one another, we measured how FRET between Cer(donor)-DWORF and YFP(acceptor)-PLB is impacted by expression of unlabeled SERCA. If SERCA interacts with PLB or DWORF monomers individually, one would expect SERCA to compete with the interactions of the PLB-DWORF heterodimer and decrease DWORF-PLB FRET. On the other hand, if multiple micropeptides can simultaneously interact with SERCA, we would predict increasing SERCA expression would bring PLB and DWORF into closer proximity and increase DWORF-PLB FRET. Figure C.1D and E show that increasing expression of unlabeled SERCA caused a decrease in the FRET_{max} of the DWORF-PLB interaction, indicating that SERCA-micropeptide binding competes with the interaction of the PLB-DWORF heterodimer. Thus, we conclude that SERCA binds monomeric PLB or DWORF individually but not both at the same time.

APPENDIX D
SUPPLEMENTARY INFORMATION FOR CHAPTER FIVE

Title and Authors of Associated Work:

A DILATED CARDIOMYOPATHY MUTATION IN PHOSPHOLAMBAN, ARGININE 14
DELETION, INCREASES PHOSPHOLAMBAN PENTAMER STABILITY

Sean R. Cleary¹, Allen C.T. Teng², Audrey Deyawe Kongmeneck¹, Xuan Fang¹, Taylor A. Phillips¹, Ellen E. Cho¹, Peter M. Kekenos-Huskey¹, Anthony O. Gramolini², and Seth L. Robia¹

¹Department of Cell and Molecular Physiology, Loyola University Chicago, Maywood, IL, USA

²Department of Physiology, University of Toronto, Toronto, Ontario, Canada

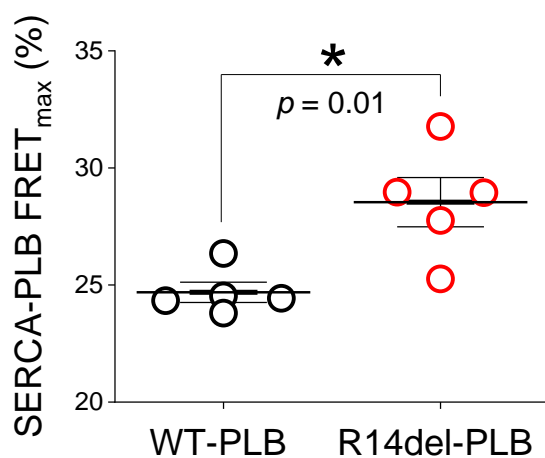
Appendix D: Abstract

The sarco(endo)plasmic reticulum Ca²⁺ ATPase (SERCA) is a membrane transporter that creates and maintains intracellular Ca²⁺ stores. In the heart, SERCA is regulated by an inhibitory interaction with the monomeric form of the transmembrane micropeptide phospholamban (PLB). PLB also forms avid homo-pentamers, and dynamic exchange of PLB between pentamers and the regulatory complex with SERCA is an important determinant of cardiac responsiveness to exercise. Here, we investigated two naturally occurring pathogenic mutations of PLB, a cysteine substitution of arginine 9 (R9C) and an in-frame deletion of arginine 14 (R14del). Both mutations are associated with dilated cardiomyopathy. We previously showed that the R9C mutation causes disulfide crosslinking and hyperstabilization of pentamers. While the pathogenic mechanism of R14del is unclear, we hypothesized that this mutation may also alter PLB homo-oligomerization and disrupt the PLB-SERCA regulatory interaction. SDS-PAGE revealed a significantly increased pentamer:monomer ratio for R14del-PLB (87.2 ± 3.2% pentamers) when compared to WT-PLB (79.5±0.8% pentamers). In addition, we quantified homo-oligomerization and SERCA-binding in live cells using fluorescence resonance energy transfer (FRET) microscopy. R14del-PLB

showed an increased affinity for homo-oligomerization and decreased binding affinity for SERCA compared to WT, suggesting that, like R9C, the R14del mutation traps PLB in its pentameric form, decreasing its ability to regulate SERCA. Moreover, the R14del mutation reduces the rate of PLB unbinding from the pentamer after a transient Ca^{2+} elevation, limiting the rate of re-binding to SERCA. A computational model predicted that hyperstabilization of PLB pentamers by R14del impairs the ability of cardiac Ca^{2+} handling to respond to changing heart rates between rest and exercise. We postulate that impaired responsiveness to physiological stress contributes to arrhythmogenesis in human carriers of the R14del mutation.

Appendix Table D.1. *P* values comparing the differential dissociation constants (K_{DS}) of PLB-PLB binding for wild-type- and mutant- PLB pentamer oligomerization. For each pair, the first binding partner is the FRET-donor, and the second is the acceptor. Data were analyzed by 1-way ANOVA with Tukey's *post-hoc* test ($p < 0.05 = *$).

PLB-PLB K_D analyzed by 1-way ANOVA with Tukey's post-hoc				
	WT-WT	R9C-R9C	WT-R9C	R14del-R14del
WT-R14del	9.85×10^{-7}	$2.50 \times 10^{-3*}$	$3.27 \times 10^{-5*}$	$8.51 \times 10^{-4*}$
R14del-R14del	$1.48 \times 10^{-8*}$	$1.30 \times 10^{-7*}$	$2.66 \times 10^{-8*}$	
WT-R9C	0.44	0.32		
R9C-R9C	0.01^*			



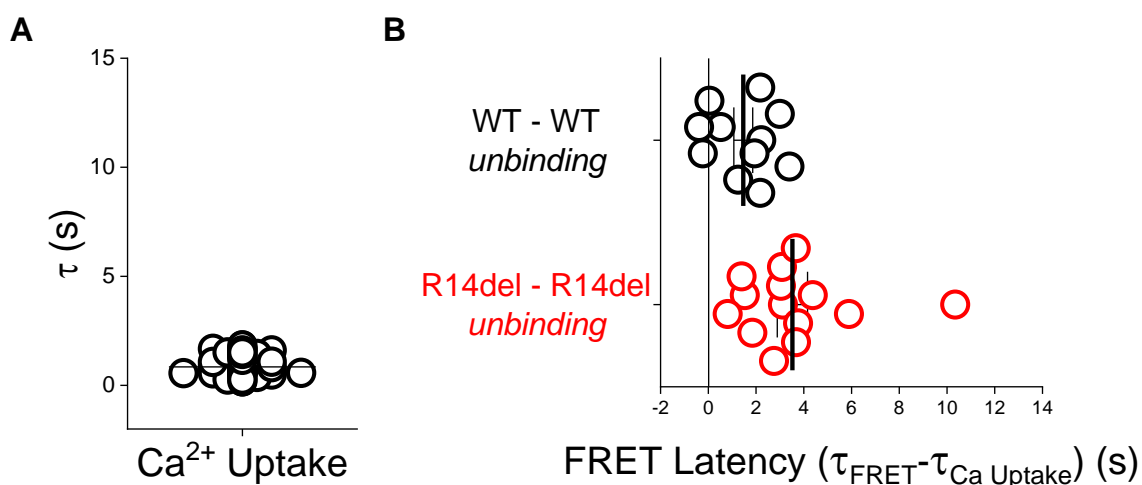
Appendix Figure D.1. FRET_{max} values for SERCA- WT-PLB and R14del-PLB determined from FRET-based binding curves. Differences were determined by student's t-test ($p < 0.05 = *$).

Appendix Table D.2. Time constants (τ) quantified for the rate of WT- and R14del-PLB-PLB unbinding associated with Ca^{2+} uptake. Time constant values are reported as mean \pm SEM.

Apparent τ (Mean \pm SEM)	
Process	τ (s)
WT – WT (unbinding)	2.6 \pm 0.4
R14del – R14del (unbinding)	4.4 \pm 0.7
Ca^{2+} Uptake	1.0 \pm 0.1

Appendix Table D.3. *P* values comparing the differences in the time constant (τ)s for of PLB oligomer unbinding for WT- and R14del-PLB pentamers in response to Ca^{2+} uptake. Data were analyzed by 1-way ANOVA with Dunn's *post-hoc* test ($p < 0.05 = *$).

PLB-PLB unbinding analyzed by 1-way ANOVA with Dunn's <i>post-hoc</i>		
	WT-WT (unbinding)	R14del-R14del (unbinding)
Ca^{2+} Uptake	0.01*	4.87 x 10 ^{-8*}
R14del-R14del (unbinding)	0.01*	



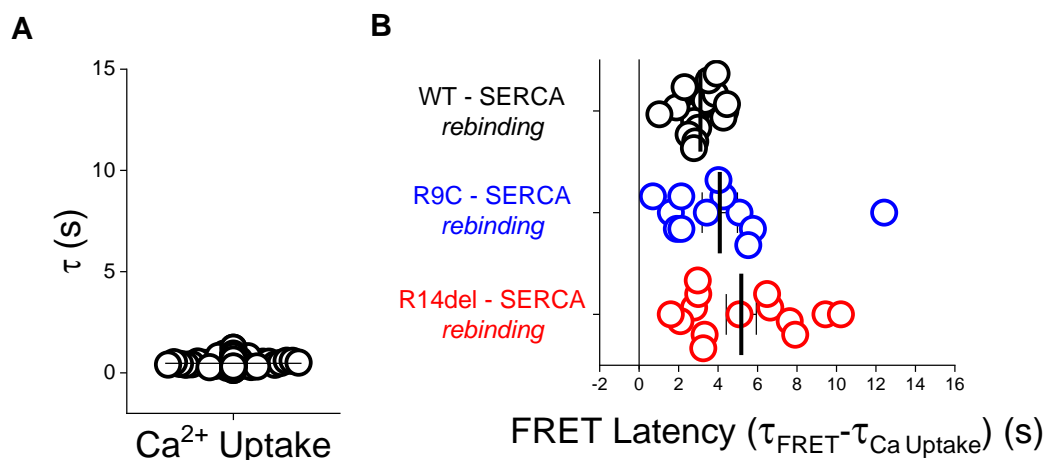
Appendix Figure D.2. **A**, Time constants for Ca^{2+} Uptake quantified for experiments measuring PLB-PLB binding dynamics in response to Ca^{2+} signaling. **B**, The latency of PLB-PLB FRET ratio changes compared to Ca^{2+} Uptake ($\tau_{\text{FRET}} - \tau_{\text{Ca Uptake}}$) with lines representing mean \pm SEM.

Appendix Table D.4. Time constants (τ) quantified for the rate of WT- and R14del-rebinding associated with Ca^{2+} uptake. Time constant values are reported as mean \pm SEM.

Apparent τ (Mean \pm SEM)	
Process	τ (s)
WT – SERCA (rebinding)	3.5 ± 0.2
R9C – SERCA (rebinding)	4.8 ± 0.9
R14del – SERCA (rebinding)	5.7 ± 0.8
Ca^{2+} Uptake	0.5 ± 0.03

Appendix Table D.5. *P* values comparing the differences in the time constant (τ)s for of PLB-SERCA rebinding for WT-, R9C-, and R14del-PLB in response to Ca^{2+} uptake. Data were analyzed by 1-way ANOVA with Dunn's *post-hoc* test ($p < 0.05 = *$).

PLB-SERCA rebinding analyzed by 1-way ANOVA with Dunn's post-hoc			
	WT-SERCA (rebinding)	R9C-SERCA (rebinding)	R14del-SERCA (rebinding)
Ca^{2+} Uptake	$7.73 \times 10^{-8*}$	$1.02 \times 10^{-10*}$	$2.67 \times 10^{-15*}$
R14del-SERCA (rebinding)	$0.003*$	0.63	
R9C-SERCA (rebinding)	0.28		



Appendix Figure D.3. **A)** Time constants for Ca^{2+} Uptake quantified for experiments measuring SERCA-PLB binding dynamics in response to Ca^{2+} signaling. **B)** The latency of SERCA-PLB FRET ratio changes compared to Ca^{2+} Uptake ($\tau_{\text{FRET}} - \tau_{\text{Ca Uptake}}$) with lines representing mean \pm SEM.

APPENDIX E
SUPPLEMENTARY INFORMATION FOR CHAPTER SIX

Title and Authors of Associated Work:

PHOSPHOLAMBAN INHIBITS THE CARDIAC CALCIUM PUMP THROUGH
REVERSING THE ALLOSTERIC ENHANCEMENT OF CALCIUM AFFINITY BY ATP

Sean R. Cleary¹, Jaroslava Seflova¹, Ellen E. Cho¹, Konark Bisht², Himanshu Khandelia², L Michel Espinoza-Fonseca³, and Seth L. Robia¹

¹Department of Cell and Molecular Physiology, Loyola University Chicago, Maywood, IL, USA

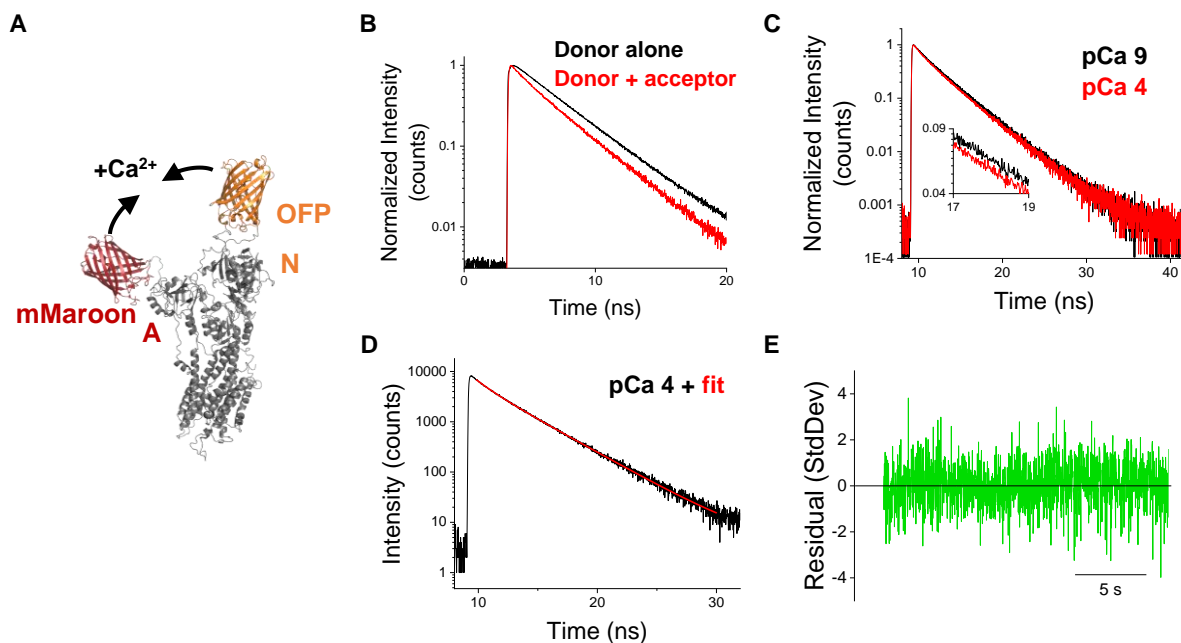
²Department of Physics, Chemistry, and Pharmacy, University of Southern Denmark, Odense, Denmark

³Division of Cardiovascular Medicine, Department of Internal Medicine, Center for Arrhythmia Research, University of Michigan, Ann Arbor, MI, USA

Appendix E: Abstract

Phospholamban (PLB) is a transmembrane micropeptide that regulates the sarcoplasmic reticulum Ca²⁺ ATPase (SERCA) in cardiac muscle, but the physical mechanism of this regulation is still poorly understood. PLB reduces the Ca²⁺ sensitivity of SERCA, increasing the Ca²⁺ concentration required for pump cycling, as measured in ATPase assays. However, PLB does not decrease ⁴⁵Ca²⁺ binding to SERCA when ATP is absent, suggesting that PLB does not alter SERCA Ca²⁺ affinity. The prevailing explanation for these seemingly conflicting results is that PLB slows the Ca²⁺ binding step in the SERCA enzymatic cycle, altering the Ca²⁺ dependence of cycling without affecting the *true* affinity of the Ca²⁺-binding sites. Here, we consider an alternative hypothesis, that equilibrium measurements of Ca²⁺ binding in the absence of ATP may overlook important allosteric effects of the bound nucleotide, which are distinct from the function of ATP as a catalytic substrate. In particular, when ATP binds it increases the affinity of SERCA for Ca²⁺. We speculated that PLB may inhibit SERCA by reversing this Ca²⁺-sensitizing effect of ATP binding. To test this hypothesis, we used a 2-color SERCA biosensor to report Ca²⁺ binding by changes in fluorescence resonance energy

transfer. We quantified the Ca^{2+} affinity of non-cycling SERCA in the absence of ATP, and in the presence of non-hydrolyzable ATP-analog AMPPCP. Interestingly, nucleotide activation by AMPPCP increased the Ca^{2+} affinity of 2-color SERCA, but this effect was reversed by co-expression of PLB. PLB had no effect on Ca^{2+} affinity in the absence of nucleotide. These results may reconcile the conflicting effects of PLB seen in SERCA ATPase assays versus Ca^{2+} binding assays. We propose that PLB reduces the true Ca^{2+} affinity of SERCA by reversing allosteric activation of the pump by ATP.



Appendix Figure E.1. **A**, 2-color SERCA biosensor labeled on the A and N domains undergoes headpiece closure during Ca^{2+} binding by intramolecular FRET. **B**, TCSPC measures how the fluorescence lifetime of the OFF donor tag on the N domain of SERCA decreases due to FRET in the presence of an mMaroon acceptor (*red*) on the A domain compared to the lifetime of SERCA tagged with OFF alone (*black*). **C**, The fluorescence lifetime of the OFF donor in 2-color SERCA is further decreased when Ca^{2+} is increased from pCa 9 to pCa 4, due closure of the labeled headpieces (as in panel A). The inset data are zoomed in to make the difference in these fluorescent decays more appreciable. **D**, A representative fit (*red*) of the OFF donor lifetime (*black*) using a two exponential decay function. **E**, A residual of a two-exponential decay fit of the OFF donor lifetime of 2-color SERCA shows that the data are well described by this two species model.

Apparent K_{Ca} in the Absence of Nucleotide (Mean \pm SEM)	
Condition	K_{Ca} (μ M)
SERCA alone	1.77 \pm 0.11
PLB	1.68 \pm 0.16
S16E	1.84 \pm 0.20

Appendix Table E.1. Apparent Ca^{2+} binding constants derived from intramolecular FRET measurements of 2-color SERCA alone and with WT- or S16E-PLB in the absence of nucleotide.

	Apparent K_{Ca} in the Absence of Nucleotide <i>p</i> values from 1-way ANOVA with Tukey's post-hoc	
	SERCA alone	PLB
S16E	0.959	0.762
PLB	0.903	

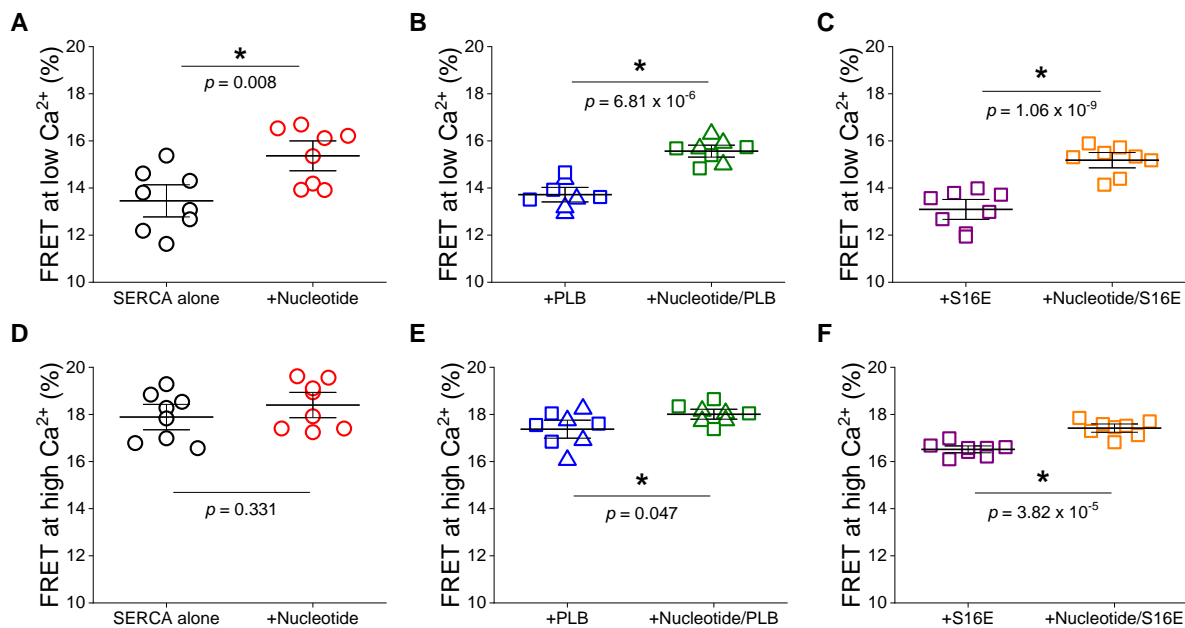
Appendix Table E.2. *P* values comparing differences in apparent Ca^{2+} binding constants of SERCA alone and with WT- or S16E-PLB in the absence of nucleotide. These values were determined by one-way ANOVA with Tukey's *post-hoc* test (* = $p < 0.05$).

Apparent K_{Ca} +Nucleotide (Mean \pm SEM)	
Condition	K_{Ca} (μ M)
SERCA alone	0.33 \pm 0.03
PLB	0.78 \pm 0.14
S16E	0.34 \pm 0.04

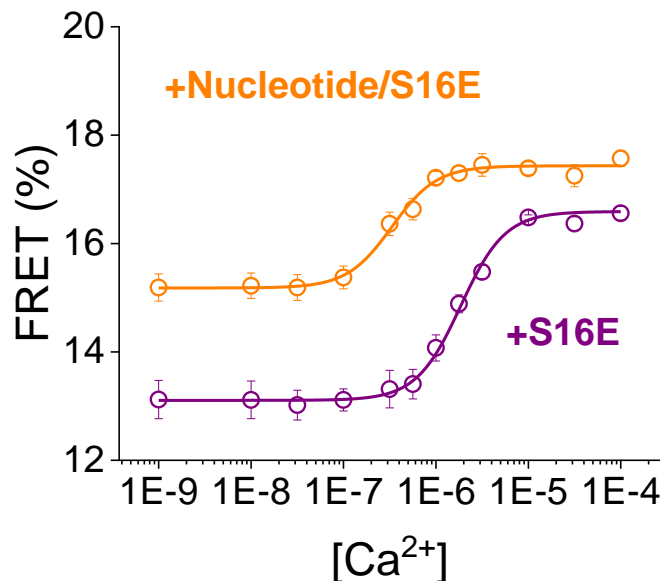
Appendix Table E.3. Apparent Ca^{2+} binding constants derived from intramolecular FRET measurements of 2-color SERCA alone and with WT- or S16E-PLB in the presence of AMPPCP.

	Apparent K_{Ca} +Nucleotide <i>p</i> values from 1-way ANOVA with Tukey's post-hoc	
	SERCA alone	PLB
S16E	0.999	0.001*
PLB	9.78 x 10⁻⁴*	

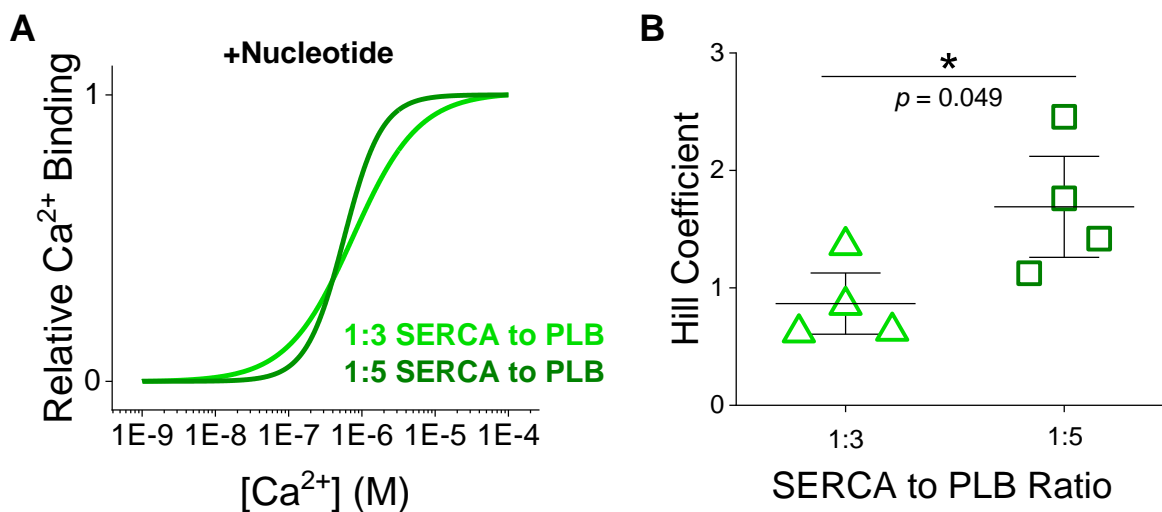
Appendix Table E.4. *P* values comparing differences in apparent Ca^{2+} binding constants of SERCA alone and with WT- or S16E-PLB in the presence of AMPPCP. These values were determined by one-way ANOVA with Tukey's *post-hoc* test (* = $p < 0.05$).



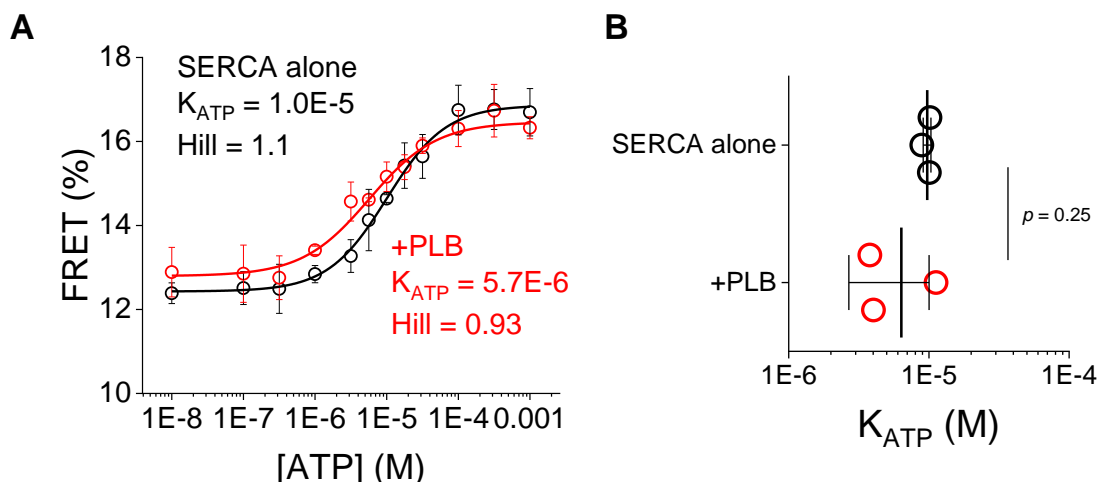
Appendix Figure E.2. The FRET efficiency of 2-color SERCA under low and high Ca^{2+} conditions as determined by fitting the average FRET of the biosensor in a range of Ca^{2+} concentrations with a Hill equation. **A-C**, FRET efficiency of 2-color SERCA at low Ca^{2+} was significantly increased by nucleotide activation in all samples. **D-F**, FRET efficiency of 2-color SERCA at high Ca^{2+} was significantly increased only in samples coexpressing WT- or S16E-PLB. SERCA to PLB transfection ratio indicated by Δ (1:3) or \square (1:5). Differences determined by student's t-test ($* = p < 0.05$).



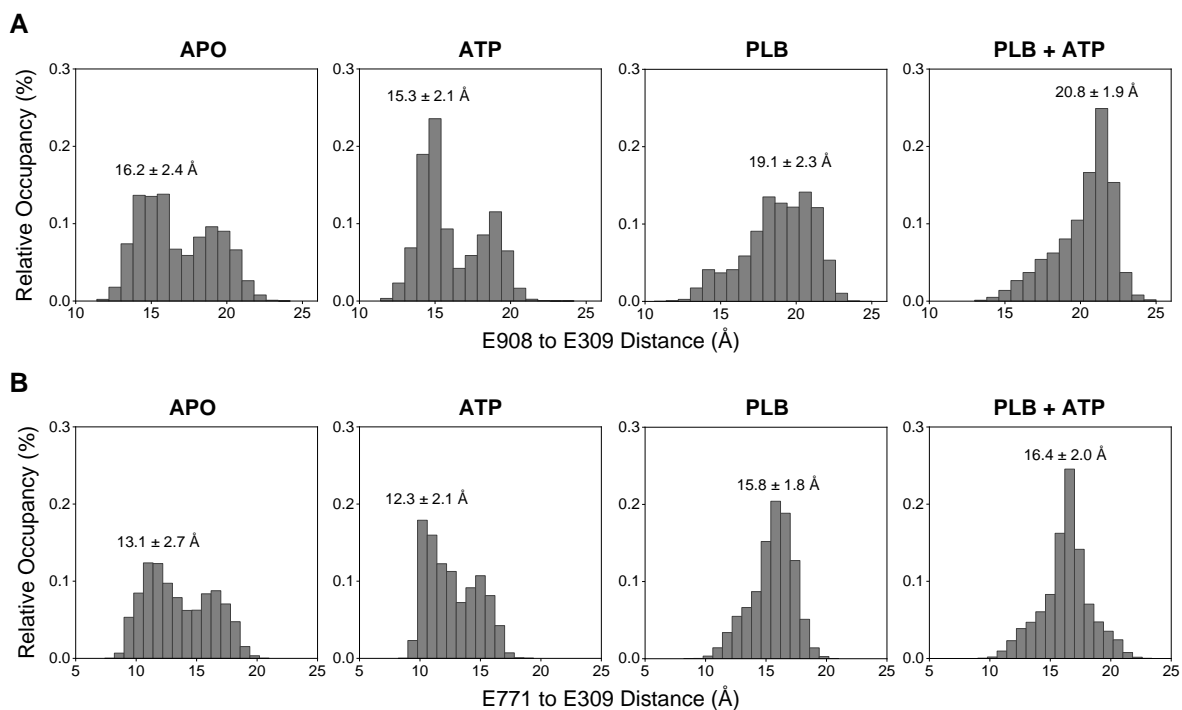
Appendix Figure E.3. 2-color SERCA FRET changes during Ca^{2+} binding measured in samples coexpressing SERCA and S16E-PLB (1:5 SERCA to PLB ratio) in the presence (*orange*) and absence of AMPPCP (*purple*). Data are the mean and SE ($n=8$).



Appendix Figure E.4. A, Normalized fitted curves for 2-color SERCA FRET changes during Ca^{2+} binding in the presence of AMPPCP for samples coexpressing WT-PLB at a 1:3 (*light green*) or a 1:5 (*dark green*) SERCA to PLB ratio. Data are based on fitting the mean and SE of 4 independent measurements. **B,** Hill coefficient values for changes in 2-color SERCA FRET during Ca^{2+} binding for samples coexpressing WT-PLB at a 1:3 (*light green*) or a 1:5 (*dark green*) SERCA to PLB ratio. Hill coefficient values were determined by global fitting the data from 4 independent experiments to share a common K_{Ca} value. SERCA to PLB transfection ratio indicated by Δ (1:3) or \square (1:5). Differences determined by student's t-test ($*=p<0.05$).



Appendix Figure E.5. A, 2-color SERCA FRET changes during ATP binding measured in samples expressing SERCA alone (*black*) or coexpressing WT-PLB at a 1:5 SERCA to PLB ratio (*red*). **B**, Values for the apparent ATP binding constant (K_{ATP}) of 2-color SERCA determined from 3 independent experiments. Differences determined by student's t-test (*= $p < 0.05$).



Appendix Figure E.6. A, Relative occupancy of the distances between SERCA Ca^{2+} binding residues E908 and E309 based on 3 independent trajectories. **B**, Relative occupancy of the distances between SERCA Ca^{2+} binding residues E771 and E309 based on 3 independent trajectories.

APPENDIX F
DIMERIZATION OF SERCA2A

Title and Authors of Associated Work:**DIMERIZATION OF SERCA2A ENHANCES TRANSPORT RATE AND IMPROVES
ENERGETIC EFFICIENCY IN LIVING CELLS**

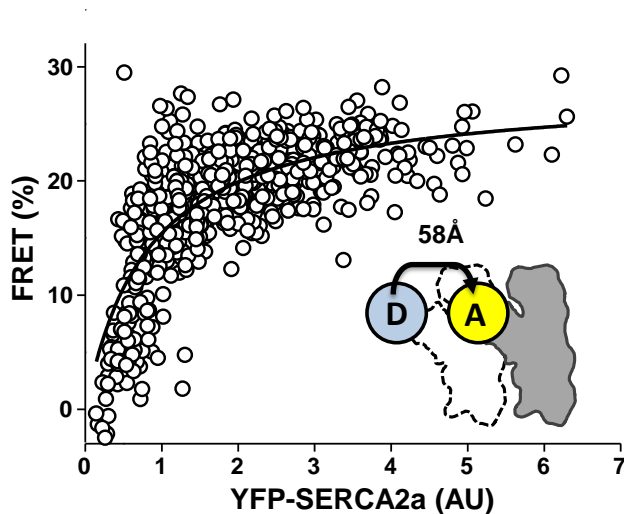
Elisa Bovo, Roman Nikolaienko, **Sean R. Cleary**, Jaroslava Seflova, Daniel Kahn, Seth L. Robia, and Aleksey V. Zima

Department of Cell and Molecular Physiology, Loyola University Chicago, Maywood, IL

Dimerization of SERCA2a Enhances Transport Rate and Energetic Efficiency in Living Cells. *Biophys J* 119(7):1456-1465, (2020).

Appendix F: Summary

We have previously shown evidence that the cardiac Ca^{2+} pump, SERCA2a, interacts with itself to form stable, homodimers in cells. However, the functional impact of SERCA dimers remains unclear. The present study shows that the concentration-dependent increase in SERCA dimer formation is associated with an exponential increase in the rate of ER Ca^{2+} uptake, suggesting that SERCA dimer formation enhances the rate of SERCA Ca^{2+} transport. Inhibition of half the population of SERCA with thapsigargin resulted in a decrease to both the rate of ER Ca^{2+} uptake and the maximum ER Ca^{2+} load, indicating that dimerization may also impact the energetic efficiency of Ca^{2+} transport. Functional results from cells coexpressing wildtype SERCA2a and SERCA2a with mutations that reduced catalytic function suggest that catalytic turnover of SERCA is required for the functional increase in Ca^{2+} transport with dimerization. The results of this study suggest that SERCA2a dimers functionally couple the catalytic cycles of two protomers to increase the overall turnover rate of the SERCA enzymatic cycle.

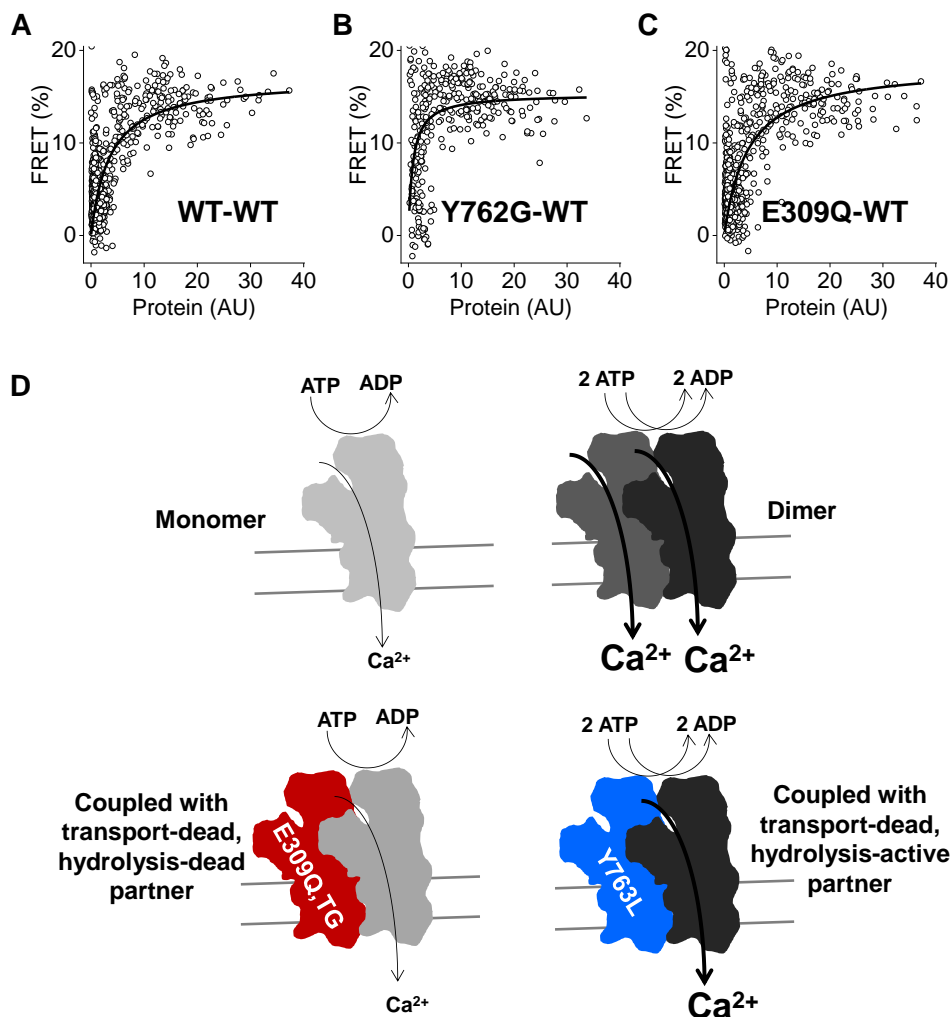


Appendix Figure F.1. Dimerization of SERCA2a in Live Cells. A FRET-based binding curves reveal a concentration dependent formation of SERCA dimers between mCer- and YFP-labeled canine SERCA2a protomers in live cells.

SERCA Dimerization in Live Cells

In the present study we used FRET acceptor sensitization measurements to detect SERCA dimer interactions within membranes of live HEK-293 cells. Figure F.1 shows that FRET was low in cells expressing low levels of YFP-SERCA2a and FRET increased with increasing protein expression. This FRET-based binding curve of SERCA-SERCA interactions was well described by a hyperbolic fit, yielding a maximum FRET efficiency (FRET_{max}) of 32%. At high protein concentrations, SERCA dimer interactions are saturated. Thus, this FRET_{max} value corresponds to the FRET efficiency of two SERCA bound in complex. According to a MATLAB model of intraoligomeric FRET (95), a FRET_{max} of 32% corresponds to a distance of 58.3 Å between donor and acceptor tags. Since saponin detergent was used to selectively permeabilize the plasma membrane of HEK293 cells for functional measurements of SERCA Ca^{2+} transport, we measured the impact of cell permeabilization on SERCA dimer FRET. We detected a

modest decrease in FRET_{max} from 32 to 28%. This decrease is likely due to an effect of the permeabilization solution on the fluorescent tags.

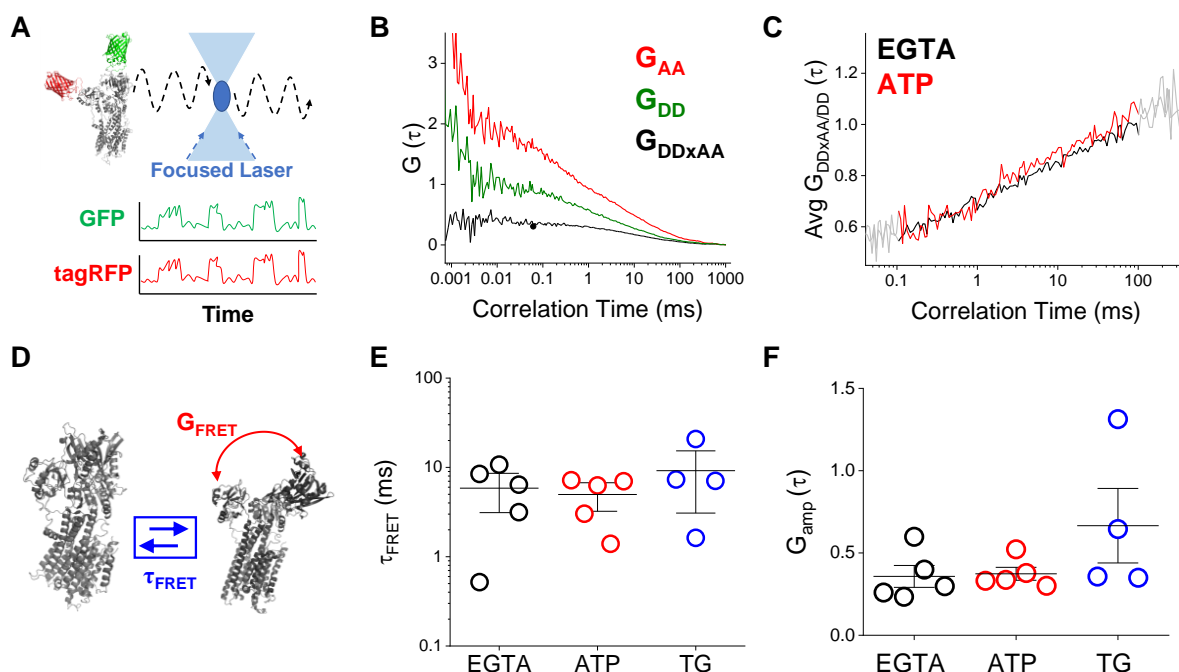


Appendix Figure F.2. ATP hydrolysis is required for functional coupling of SERCA2a dimers. FRET-based binding curves reveal a similar concentration dependence of SERCA dimers consisting of human mCer-labeled WT- (**A**), Y762G- (**B**), and E309Q-SERCA2a (**C**), binding to YFP-labeled human WT-SERCA2a. **D**, A schematic diagram designed by Dr. Aleksey V. Zima summarizes the impact of SERCA mutations or inhibition by thapsigargin (TG) on the functional coupling of SERCA2a dimers.

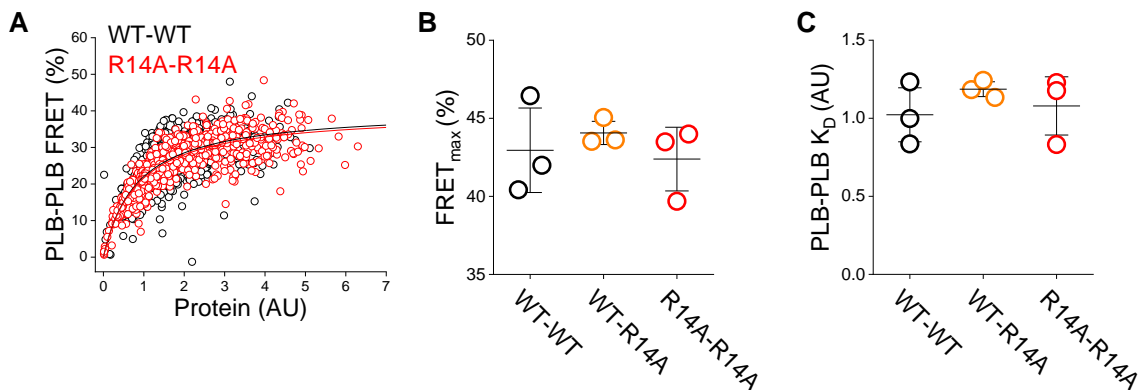
Catalytic ATP-hydrolysis is required for Functional Coupling of SERCA Dimers

The present study found that the concentration dependent increase in SERCA dimers detected by FRET measurements was associated with a non-linear increase in maximal ER Ca^{2+} uptake rate. This suggests that dimerization of SERCA enhances the overall turnover rate of the SERCA catalytic cycle. To determine the requirements of Ca^{2+} transport and ATP-hydrolysis on the functional coupling of SERCA dimers, we measured the impact of two SERCA mutations which impair these aspects of SERCA function on SERCA dimerization. The first mutation, Y762G, impairs SERCA Ca^{2+} transport without decreasing the ability of the cytoplasmic headpieces to hydrolyze ATP (175). The second mutation, E309Q, impairs both Ca^{2+} transport and ATP hydrolysis (172). FRET-acceptor sensitization shows that the formation of SERCA dimers was preserved between WT- and mutant-SERCA (Fig. F.2A-C). Interestingly, functional measurements of SERCA Ca^{2+} uptake revealed that Ca^{2+} transport was more greatly impaired in cells co-expressing WT- with E309Q-SERCA2a than in cells co-expressing WT-SERCA with the mutant that preserves ATP-hydrolysis, Y762G. This suggests that Ca^{2+} transport by the WT-SERCA2a is enhanced by dimerization with a partner that is able hydrolyze ATP, even if the other protomer in the dimer cannot transport Ca^{2+} . These functional results are summarized by the schematic diagram in Figure F.2D. Overall, the results suggest that SERCA dimers cause an increase in the overall turnover rate of the SERCA enzymatic cycle.

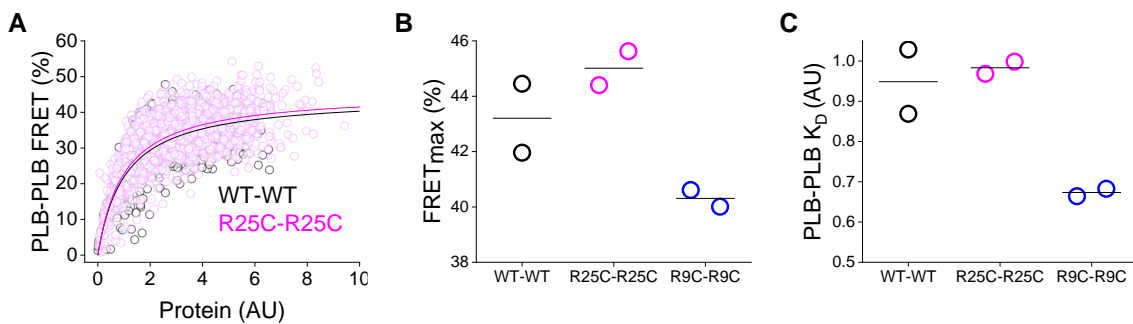
APPENDIX G
ADDITIONAL DATA



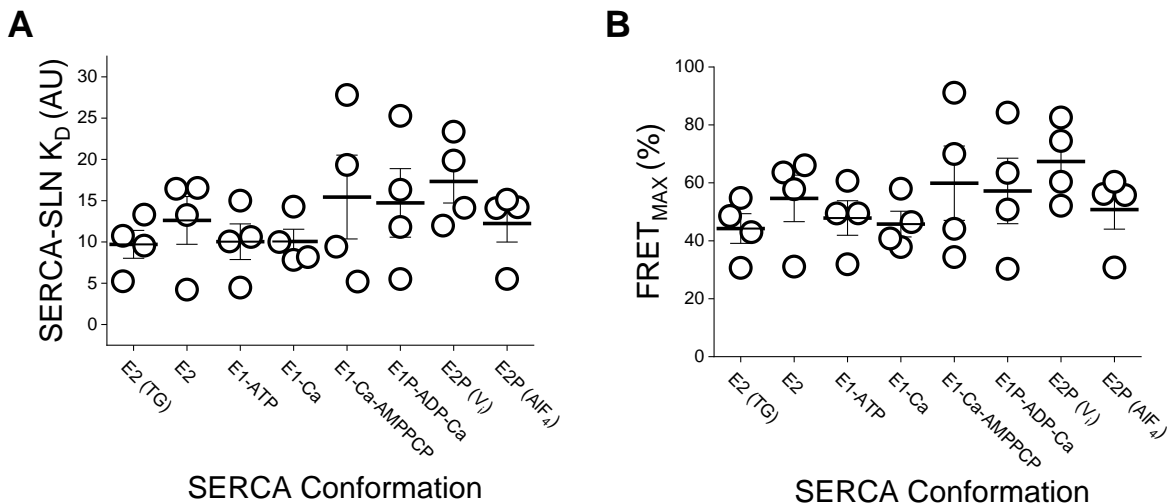
Appendix G.1. FCCS measures the dynamic motions of the SERCA headpiece domain. **A**, FCS measures the Brownian diffusion of GFP and tagRFP tags on the A and N domains of SERCA. **B**, Autocorrelation curves measure the diffusion of the TagRFP acceptor (G_{AA} , red) and GFP donor (G_{DD} , green). A cross-correlation curve of the donor and acceptor signals is also displayed ($G_{DD \times AA}$, black). **C**, FCCS curves were generated by dividing the cross correlation curve ($G_{DD \times AA}$) by the autocorrelation curve for the GFP donor (G_{DD}). Data represent the average $G_{DD \times AA/DD}$ of 5 independent experiments measuring SERCA headpiece motions in a low Ca^{2+} solution (EGTA, black) and in a solution with 3 mM ATP added (ATP, red). **D**, Single-exponential decay fits of FCCS curves reveals the τ_{FRET} (how fast are SERCA headpiece motions) and G_{amp} (how big are SERCA headpiece motions). **E**, τ_{FRET} values measured for 2-Color SERCA in EGTA (black), +3mM ATP (red), +100 μ M TG (blue). **F**, G_{amp} values measured for 2-Color SERCA in EGTA (black), +3mM ATP (red), +100 μ M TG (blue). Lines represent mean and SE ($n=5$ for EGTA and ATP, $n=4$ for TG). We did not detect any significant differences in the data when analyzed by 1-way ANOVA with Dunn's *post hoc*.



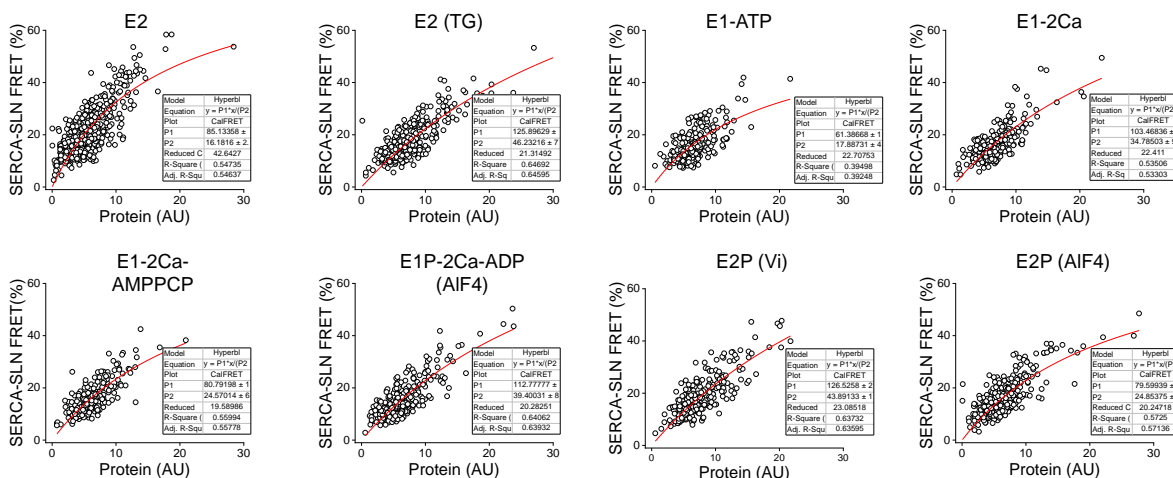
Appendix Figure G.2. R14A Mutation does not Alter PLB Oligomerization. A, Representative binding curves for WT-PLB (*black*) and R14A (*red*) homo-oligomerization. **B,** FRET_{max} values derived from binding curves measuring WT-WT, WT-R14A, and R14A-R14A oligomerization. **C,** Dissociation constant values derived from binding curves measuring WT-WT, WT-R14A, and R14A-R14A oligomerization. The first of the pair was tagged with mCer fluorescent donor and the second was tagged with YFP fluorescent acceptor. Constructs were expressed at a 1:5 donor to acceptor ratio.



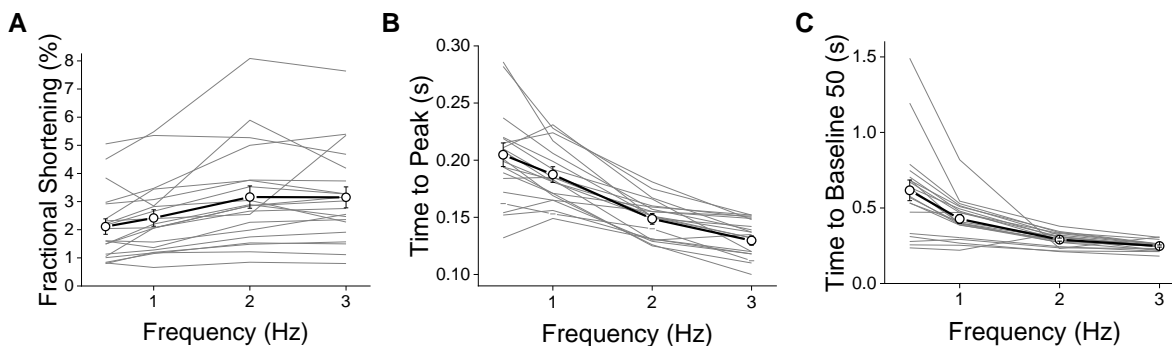
Appendix Figure G.3. R25C Mutation does not Alter PLB Oligomerization. A, Representative binding curves for WT-PLB (*black*) and R25C (*magenta*) homo-oligomerization. **B,** FRET_{max} values derived from binding curves measuring WT-WT, R25C-R25C, and R9C-R9C oligomerization. **C,** Dissociation constant values derived from binding curves measuring WT-WT, R25C-R25C, and R9C-R9C oligomerization.



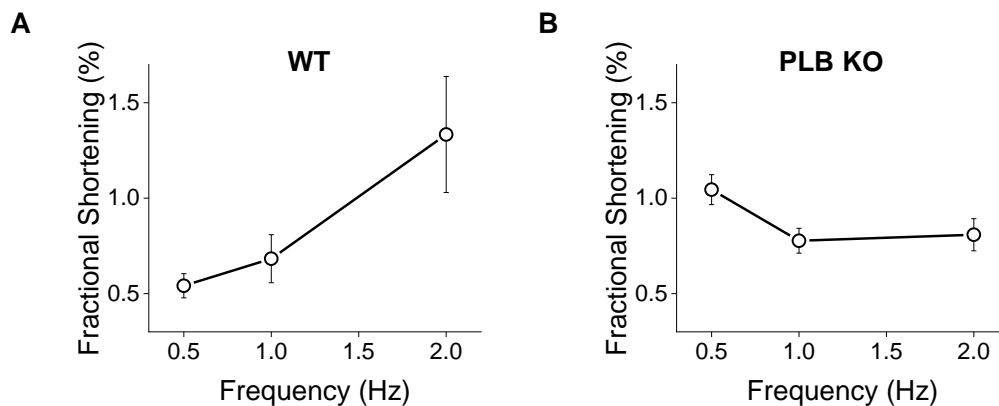
Appendix Figure G.4. Characterization of SLN interactions with different biochemical states of SERCA. **A**, Apparent K_D values for SLN binding to different conformations of SERCA. **B**, FRET_{max} values for SLN binding to different conformations of SERCA. Cells expressing mCer-SERCA and YFP-SLN at a donor to acceptor ratio of 1:5 were used to acquire the above data. Due to poor saturation of binding curves, FRET_{max} values ranged from 30% to nearly 100% barring interpretation of changes in apparent K_D .



Appendix Figure G.5. SLN-SERCA Binding Curves. FRET-based binding curves acquired from cells expressing mCer-SERCA and YFP-SLN at a 1:20 donor to acceptor ratio seem to show improved consistency in saturation of FRET efficiency at high protein expression, but FRET_{max} values still varied broadly. There is an apparent left shift of the data for SLN binding E2 SERCA (achieved with a low Ca^{2+} permeabilization solution). However, this apparent change in affinity was not reflected by the K_D derived from a hyperbolic fit of the data. Therefore, it is unclear if SLN prefers to bind the E2 state over other SERCA conformations.



Appendix Figure G.6. The Positive Force-Frequency Relationship of Cardiac Muscle Measured in Mouse Cardiomyocytes. **A**, The fractional shortening of cardiomyocyte contractions increases at faster pacing frequency. The time of contraction (**B**), and relaxation (**C**), also become shorter as the kinetics of these processes accelerate at faster pacing frequency. Data represent IonOptix measurements of changes in sarcomere length from 20 cells from 4 male wildtype C57BL/6 mice. Ages ranged from 3 weeks to 6 months. Mean and SE values (*white circles, black line*) are overlaid over the data for individual cells (*light grey lines*).



Appendix Figure G.7. PLB Knock-Out Abolishes the Positive Force-Frequency Relationship in Mice. **A**, Fractional shortening measurements of cardiomyocytes isolated from WT-C57BL/6 mice ($n = 3$). **B**, Fractional shortening measurements of cardiomyocytes isolated from PLB-KO (PLN^{-/-}) C57BL/6 mice ($n = 21$). The data were collected on a separate IonOptix system from the data in Fig. G.6. Specifically, these measurements were made in collaboration with Dr. Catherine Makarewich at Cincinnati Children's Hospital.

REFERENCE LIST

1. R. Verardi, L. Shi, N. J. Traaseth, N. Walsh, G. Veglia, Structural topology of phospholamban pentamer in lipid bilayers by a hybrid solution and solid-state NMR method. *Proc Natl Acad Sci U S A* **108**, 9101-9106 (2011).
2. C. Toyoshima *et al.*, Crystal structures of the calcium pump and sarcolipin in the Mg²⁺-bound E1 state. *Nature* **495**, 260-264 (2013).
3. G. Hughes, A. P. Starling, R. P. Sharma, J. M. East, A. G. Lee, An investigation of the mechanism of inhibition of the Ca(2+)-ATPase by phospholamban. *Biochem J* **318 (Pt 3)**, 973-979 (1996).
4. S. Lamberth *et al.*, NMR solution structure of phospholamban. *Helv Chim Acta* **83**, 2141-2152 (2000).
5. E. Fernandez-de Gortari, L. M. Espinoza-Fonseca, Structural basis for relief of phospholamban-mediated inhibition of the sarcoplasmic reticulum Ca(2+)-ATPase at saturating Ca(2+) conditions. *J Biol Chem* **293**, 12405-12414 (2018).
6. M. E. Fisher *et al.*, Dwarf open reading frame (DWORF) is a direct activator of the sarcoplasmic reticulum calcium pump SERCA. *Elife* **10**, (2021).
7. U. V. Reddy *et al.*, A kink in DWORF helical structure controls the activation of the sarcoplasmic reticulum Ca(2+)-ATPase. *Structure* **30**, 360-370 e366 (2022).
8. C. Toyoshima, H. Nomura, Structural changes in the calcium pump accompanying the dissociation of calcium. *Nature* **418**, 605-611 (2002).
9. O. N. Raguimova *et al.*, Redistribution of SERCA calcium pump conformers during intracellular calcium signaling. *Journal of Biological Chemistry* **293**, 10843-10856 (2018).
10. C. Toyoshima, M. Nakasako, H. Nomura, H. Ogawa, Crystal structure of the calcium pump of sarcoplasmic reticulum at 2.6 Å resolution. *Nature* **405**, 647-655 (2000).
11. T. L. Sorensen, J. V. Moller, P. Nissen, Phosphoryl transfer and calcium ion occlusion in the calcium pump. *Science* **304**, 1672-1675 (2004).
12. C. Toyoshima, H. Nomura, T. Tsuda, Lumenal gating mechanism revealed in calcium pump crystal structures with phosphate analogues. *Nature* **432**, 361-368 (2004).
13. J. D. Clausen *et al.*, Crystal Structure of the Vanadate-Inhibited Ca(2+)-ATPase. *Structure* **24**, 617-623 (2016).
14. M. Bublitz *et al.*, Ion pathways in the sarcoplasmic reticulum Ca²⁺-ATPase. *J Biol Chem* **288**, 10759-10765 (2013).

15. T. Cantilina, Y. Sagara, G. Inesi, L. R. Jones, Comparative studies of cardiac and skeletal sarcoplasmic reticulum ATPases. Effect of a phospholamban antibody on enzyme activation by Ca^{2+} . *J Biol Chem* **268**, 17018-17025 (1993).
16. W. W. Kielley, O. Meyerhof, A new magnesium-activated adenosinetriphosphatase from muscle. *J Biol Chem* **174**, 387 (1948).
17. S. Ebashi, Calcium binding activity of vesicular relaxing factor. *J Chir (Paris)* **82**, 236-244 (1961).
18. M. G. Palmgren, P. Nissen, P-type ATPases. *Annu Rev Biophys* **40**, 243-266 (2011).
19. G. Inesi, Mechanism of calcium transport. *Annu Rev Physiol* **47**, 573-601 (1985).
20. D. H. MacLennan, W. J. Rice, N. M. Green, The mechanism of Ca^{2+} transport by sarco(endo)plasmic reticulum Ca^{2+} -ATPases. *J Biol Chem* **272**, 28815-28818 (1997).
21. R. Aguayo-Ortiz, L. M. Espinoza-Fonseca, Linking Biochemical and Structural States of SERCA: Achievements, Challenges, and New Opportunities. *Int J Mol Sci* **21**, (2020).
22. D. M. Bers, *Excitation-Contraction Coupling and Cardiac Contractile Force*. (Kluwer Academic Publisher, ed. Second Edition, 2001).
23. A. Fabiato, F. Fabiato, Calcium-induced release of calcium from the sarcoplasmic reticulum of skinned cells from adult human, dog, cat, rabbit, rat, and frog hearts and from fetal and new-born rat ventricles. *Ann N Y Acad Sci* **307**, 491-522 (1978).
24. D. R. Scriven, P. Dan, E. D. Moore, Distribution of proteins implicated in excitation-contraction coupling in rat ventricular myocytes. *Biophys J* **79**, 2682-2691 (2000).
25. D. M. Bers, Cardiac excitation-contraction coupling. *Nature* **415**, 198-205 (2002).
26. E. Bovo, S. R. Mazurek, L. A. Blatter, A. V. Zima, Regulation of sarcoplasmic reticulum Ca^{2+} leak by cytosolic Ca^{2+} in rabbit ventricular myocytes. *J Physiol* **589**, 6039-6050 (2011).
27. A. B. Mason, J. C. Tardiff, S. D. Schwartz, Free-Energy Surfaces of Two Cardiac Thin Filament Conformational Changes during Muscle Contraction. *J Phys Chem B* **126**, 3844-3851 (2022).
28. M. J. Previs, A. J. Michalek, D. M. Warshaw, Molecular modulation of actomyosin function by cardiac myosin-binding protein C. *Pflugers Arch* **466**, 439-444 (2014).
29. E. Bovo *et al.*, Dimerization of SERCA2a Enhances Transport Rate and Improves Energetic Efficiency in Living Cells. *Biophys J* **119**, 1456-1465 (2020).
30. N. C. f. H. S. Centers for Disease Control and Prevention. (Atlanta, GA: Centers for Disease Control and Prevention, CDC WONDER Online Database website, 2022), vol. 2022.
31. S. S. Virani *et al.*, Heart Disease and Stroke Statistics-2020 Update: A Report From the American Heart Association. *Circulation* **141**, e139-e596 (2020).

32. J. E. Ho *et al.*, Predicting Heart Failure With Preserved and Reduced Ejection Fraction: The International Collaboration on Heart Failure Subtypes. *Circ Heart Fail* **9**, (2016).
33. S. R. Houser, V. Piacentino, 3rd, J. Weisser, Abnormalities of calcium cycling in the hypertrophied and failing heart. *J Mol Cell Cardiol* **32**, 1595-1607 (2000).
34. G. Hasenfuss *et al.*, Relation between myocardial function and expression of sarcoplasmic reticulum Ca(2+)-ATPase in failing and nonfailing human myocardium. *Circ Res* **75**, 434-442 (1994).
35. M. A. Shareef, L. A. Anwer, C. Poizat, Cardiac SERCA2A/B: therapeutic targets for heart failure. *Eur J Pharmacol* **724**, 1-8 (2014).
36. M. J. Byrne *et al.*, Recirculating cardiac delivery of AAV2/1SERCA2a improves myocardial function in an experimental model of heart failure in large animals. *Gene Ther* **15**, 1550-1557 (2008).
37. D. R. Stroik *et al.*, Viral expression of a SERCA2a-activating PLB mutant improves calcium cycling and synchronicity in dilated cardiomyopathic hiPSC-CMs. *J Mol Cell Cardiol* **138**, 59-65 (2020).
38. C. A. Makarewich, S. Bezprozvannaya, A. M. Gibson, R. Bassel-Duby, E. N. Olson, Gene Therapy With the DWORF Micropeptide Attenuates Cardiomyopathy in Mice. *Circ Res* **127**, 1340-1342 (2020).
39. R. J. Hajjar *et al.*, Design of a phase 1/2 trial of intracoronary administration of AAV1/SERCA2a in patients with heart failure. *J Card Fail* **14**, 355-367 (2008).
40. M. Jessup *et al.*, Calcium Upregulation by Percutaneous Administration of Gene Therapy in Cardiac Disease (CUPID): a phase 2 trial of intracoronary gene therapy of sarcoplasmic reticulum Ca²⁺-ATPase in patients with advanced heart failure. *Circulation* **124**, 304-313 (2011).
41. B. Greenberg *et al.*, Calcium upregulation by percutaneous administration of gene therapy in patients with cardiac disease (CUPID 2): a randomised, multinational, double-blind, placebo-controlled, phase 2b trial. *Lancet* **387**, 1178-1186 (2016).
42. R. L. Cornea *et al.*, High-throughput FRET assay yields allosteric SERCA activators. *J Biomol Screen* **18**, 97-107 (2013).
43. T. M. Schaaf *et al.*, High-Throughput Spectral and Lifetime-Based FRET Screening in Living Cells to Identify Small-Molecule Effectors of SERCA. *SLAS Discov* **22**, 262-273 (2017).
44. S. J. Gruber *et al.*, Discovery of enzyme modulators via high-throughput time-resolved FRET in living cells. *J Biomol Screen* **19**, 215-222 (2014).
45. P. A. Bidwell *et al.*, A Large-Scale High-Throughput Screen for Modulators of SERCA Activity. *Biomolecules* **12**, (2022).

46. V. Niggli, E. Sigel, Anticipating antiport in P-type ATPases. *Trends Biochem Sci* **33**, 156-160 (2008).
47. R. W. Albers, Biochemical aspects of active transport. *Annu Rev Biochem* **36**, 727-756 (1967).
48. X. Yu, S. Carroll, J. L. Rigaud, G. Inesi, H⁺ countertransport and electrogenicity of the sarcoplasmic reticulum Ca²⁺ pump in reconstituted proteoliposomes. *Biophys J* **64**, 1232-1242 (1993).
49. J. D. Clausen, I. Vandecaetsbeek, F. Wuytack, P. Vangheluwe, J. P. Andersen, Distinct roles of the C-terminal 11th transmembrane helix and luminal extension in the partial reactions determining the high Ca²⁺ affinity of sarco(endo)plasmic reticulum Ca²⁺-ATPase isoform 2b (SERCA2b). *J Biol Chem* **287**, 39460-39469 (2012).
50. D. H. MacLennan, C. J. Brandl, B. Korczak, N. M. Green, Amino-acid sequence of a Ca²⁺ + Mg²⁺-dependent ATPase from rabbit muscle sarcoplasmic reticulum, deduced from its complementary DNA sequence. *Nature* **316**, 696-700 (1985).
51. C. J. Brandl, N. M. Green, B. Korczak, D. H. MacLennan, Two Ca²⁺ ATPase genes: homologies and mechanistic implications of deduced amino acid sequences. *Cell* **44**, 597-607 (1986).
52. C. Tanford, J. A. Reynolds, E. A. Johnson, Sarcoplasmic reticulum calcium pump: a model for Ca²⁺ binding and Ca²⁺-coupled phosphorylation. *Proc Natl Acad Sci U S A* **84**, 7094-7098 (1987).
53. Y. Kabashima, H. Ogawa, R. Nakajima, C. Toyoshima, What ATP binding does to the Ca(2+) pump and how nonproductive phosphoryl transfer is prevented in the absence of Ca(2). *Proc Natl Acad Sci U S A* **117**, 18448-18458 (2020).
54. K. Hauser, A. Barth, Side-chain protonation and mobility in the sarcoplasmic reticulum Ca²⁺-ATPase: implications for proton countertransport and Ca²⁺ release. *Biophys J* **93**, 3259-3270 (2007).
55. G. Inesi *et al.*, Equilibrium and kinetic studies of calcium transport and ATPase activity in sarcoplasmic reticulum. *Z Naturforsch C Biosci* **37**, 685-691 (1982).
56. G. Inesi, D. Lewis, H. Ma, A. Prasad, C. Toyoshima, Concerted conformational effects of Ca²⁺ and ATP are required for activation of sequential reactions in the Ca²⁺ ATPase (SERCA) catalytic cycle. *Biochemistry* **45**, 13769-13778 (2006).
57. K. Tran, N. P. Smith, D. S. Loiselle, E. J. Crampin, A thermodynamic model of the cardiac sarcoplasmic/endoplasmic Ca(2+) (SERCA) pump. *Biophys J* **96**, 2029-2042 (2009).
58. D. E. Befroy, T. Powell, G. K. Radda, K. Clarke, Osmotic shock: modulation of contractile function, pHi, and ischemic damage in perfused guinea pig heart. *Am J Physiol* **276**, H1236-1244 (1999).

59. J. M. Autry, J. E. Rubin, B. Svensson, J. Li, D. D. Thomas, Nucleotide activation of the Ca-ATPase. *J Biol Chem* **287**, 39070-39082 (2012).
60. T. L. Sorensen, Y. Dupont, B. Vilsen, J. P. Andersen, Fast kinetic analysis of conformational changes in mutants of the Ca(2+)-ATPase of sarcoplasmic reticulum. *J Biol Chem* **275**, 5400-5408 (2000).
61. J. P. Andersen, T. L. Sorensen, K. Povlsen, B. Vilsen, Importance of transmembrane segment M3 of the sarcoplasmic reticulum Ca²⁺-ATPase for control of the gateway to the Ca²⁺ sites. *J Biol Chem* **276**, 23312-23321 (2001).
62. L. Dode *et al.*, Dissection of the functional differences between sarco(endo)plasmic reticulum Ca²⁺-ATPase (SERCA) 1 and 2 isoforms and characterization of Darier disease (SERCA2) mutants by steady-state and transient kinetic analyses. *J Biol Chem* **278**, 47877-47889 (2003).
63. J. D. Clausen *et al.*, ATP-binding modes and functionally important interdomain bonds of sarcoplasmic reticulum Ca²⁺-ATPase revealed by mutation of glycine 438, glutamate 439, and arginine 678. *J Biol Chem* **282**, 20686-20697 (2007).
64. N. Stahl, W. P. Jencks, Adenosine 5'-triphosphate at the active site accelerates binding of calcium to calcium adenosinetriphosphatase. *Biochemistry* **23**, 5389-5392 (1984).
65. Z. Hou *et al.*, 2-Color calcium pump reveals closure of the cytoplasmic headpiece with calcium binding. *PLoS One* **7**, e40369 (2012).
66. A. Sakuntabhai *et al.*, Mutations in ATP2A2, encoding a Ca²⁺ pump, cause Darier disease. *Nat Genet* **21**, 271-277 (1999).
67. K. Haghighi *et al.*, Human phospholamban null results in lethal dilated cardiomyopathy revealing a critical difference between mouse and human. *J Clin Invest* **111**, 869-876 (2003).
68. D. Eisner, J. Caldwell, A. Trafford, Sarcoplasmic reticulum Ca-ATPase and heart failure 20 years later. *Circ Res* **113**, 958-961 (2013).
69. C. Kho, A. Lee, R. J. Hajjar, Altered sarcoplasmic reticulum calcium cycling--targets for heart failure therapy. *Nat Rev Cardiol* **9**, 717-733 (2012).
70. M. Tada, M. A. Kirchberger, A. M. Katz, Phosphorylation of a 22,000-dalton component of the cardiac sarcoplasmic reticulum by adenosine 3':5'-monophosphate-dependent protein kinase. *J Biol Chem* **250**, 2640-2647 (1975).
71. D. M. Anderson *et al.*, Widespread control of calcium signaling by a family of SERCA-inhibiting micropeptides. *Sci Signal* **9**, ra119 (2016).
72. R. F. Alford, N. Smolin, H. S. Young, J. J. Gray, S. L. Robia, Protein docking and steered molecular dynamics suggest alternative phospholamban-binding sites on the SERCA calcium transporter. *J Biol Chem* **295**, 11262-11274 (2020).

73. D. H. MacLennan, E. G. Kranias, Phospholamban: a crucial regulator of cardiac contractility. *Nat Rev Mol Cell Biol* **4**, 566-577 (2003).
74. B. A. Davis *et al.*, The role of phospholamban in the regulation of calcium transport by cardiac sarcoplasmic reticulum. *Mol Cell Biochem* **99**, 83-88 (1990).
75. G. Hughes, A. P. Starling, R. P. Sharma, J. M. East, A. G. Lee, An investigation of the mechanism of inhibition of the Ca(2+)-ATPase by phospholamban. *Biochem J* **318 (Pt 3)**, 973-979 (1996).
76. O. N. Raguimova, R. Aguayo-Ortiz, S. L. Robia, L. M. Espinoza-Fonseca, Dynamics-Driven Allostery Underlies Ca(2+)-Mediated Release of SERCA Inhibition by Phospholamban. *Biophys J* **119**, 1917-1926 (2020).
77. Y. Wang *et al.*, Intracellular beta(1)-Adrenergic Receptors and Organic Cation Transporter 3 Mediate Phospholamban Phosphorylation to Enhance Cardiac Contractility. *Circ Res* **128**, 246-261 (2021).
78. M. Asahi, E. McKenna, K. Kurzydowski, M. Tada, D. H. MacLennan, Physical interactions between phospholamban and sarco(endoplasmic reticulum Ca²⁺-ATPases are dissociated by elevated Ca²⁺, but not by phospholamban phosphorylation, vanadate, or thapsigargin, and are enhanced by ATP. *J Biol Chem* **275**, 15034-15038 (2000).
79. P. James, M. Inui, M. Tada, M. Chiesi, E. Carafoli, Nature and site of phospholamban regulation of the Ca²⁺ pump of sarcoplasmic reticulum. *Nature* **342**, 90-92 (1989).
80. C. Toyoshima *et al.*, Modeling of the inhibitory interaction of phospholamban with the Ca²⁺ ATPase. *Proc Natl Acad Sci U S A* **100**, 467-472 (2003).
81. Z. Chen, B. L. Akin, L. R. Jones, Ca²⁺ binding to site I of the cardiac Ca²⁺ pump is sufficient to dissociate phospholamban. *J Biol Chem* **285**, 3253-3260 (2010).
82. L. R. Jones, R. L. Cornea, Z. Chen, Close proximity between residue 30 of phospholamban and cysteine 318 of the cardiac Ca²⁺ pump revealed by intermolecular thiol cross-linking. *J Biol Chem* **277**, 28319-28329 (2002).
83. C. B. Karim, Z. Zhang, E. C. Howard, K. D. Torgersen, D. D. Thomas, Phosphorylation-dependent conformational switch in spin-labeled phospholamban bound to SERCA. *J Mol Biol* **358**, 1032-1040 (2006).
84. P. Bidwell, D. J. Blackwell, Z. Hou, A. V. Zima, S. L. Robia, Phospholamban binds with differential affinity to calcium pump conformers. *J Biol Chem* **286**, 35044-35050 (2011).
85. M. Gustavsson *et al.*, Allosteric regulation of SERCA by phosphorylation-mediated conformational shift of phospholamban. *Proc Natl Acad Sci U S A* **110**, 17338-17343 (2013).
86. H. P. Bowditch, Über die Eigenthümlichkeiten der Reizbarkeit, welche die Muskelfasern des Herzens zeigen. *Arbeiten aus der Physiologischen Anstalt zu Leipzig.*, (1871).

87. M. Meyer *et al.*, Phospholamban-to-SERCA2 ratio controls the force-frequency relationship. *Am J Physiol* **276**, H779-785 (1999).
88. W. F. Bluhm, E. G. Kranias, W. H. Dillmann, M. Meyer, Phospholamban: a major determinant of the cardiac force-frequency relationship. *Am J Physiol Heart Circ Physiol* **278**, H249-255 (2000).
89. Y. Wu *et al.*, CaMKII effects on inotropic but not lusitropic force frequency responses require phospholamban. *J Mol Cell Cardiol* **53**, 429-436 (2012).
90. D. Balcazar *et al.*, SERCA is critical to control the Bowditch effect in the heart. *Sci Rep* **8**, 12447 (2018).
91. K. S. Lee, Potentiation of the calcium-channel currents of internally perfused mammalian heart cells by repetitive depolarization. *Proc Natl Acad Sci U S A* **84**, 3941-3945 (1987).
92. D. R. Singh *et al.*, Newly Discovered Micropeptide Regulators of SERCA Form Oligomers but Bind to the Pump as Monomers. *J Mol Biol* **431**, 4429-4443 (2019).
93. Y. Kimura, K. Kurzydowski, M. Tada, D. H. MacLennan, Phospholamban inhibitory function is activated by depolymerization. *J Biol Chem* **272**, 15061-15064 (1997).
94. R. L. Cornea, L. R. Jones, J. M. Autry, D. D. Thomas, Mutation and phosphorylation change the oligomeric structure of phospholamban in lipid bilayers. *Biochemistry* **36**, 2960-2967 (1997).
95. Z. Hou, E. M. Kelly, S. L. Robia, Phosphomimetic mutations increase phospholamban oligomerization and alter the structure of its regulatory complex. *J Biol Chem* **283**, 28996-29003 (2008).
96. S. L. Robia *et al.*, Forster transfer recovery reveals that phospholamban exchanges slowly from pentamers but rapidly from the SERCA regulatory complex. *Circ Res* **101**, 1123-1129 (2007).
97. D. Koch *et al.*, Molecular noise filtering in the beta-adrenergic signaling network by phospholamban pentamers. *Cell Rep* **36**, 109448 (2021).
98. B. R. Nelson *et al.*, A peptide encoded by a transcript annotated as long noncoding RNA enhances SERCA activity in muscle. *Science* **351**, 271-275 (2016).
99. C. A. Makarewich, E. N. Olson, Mining for Micropeptides. *Trends Cell Biol* **27**, 685-696 (2017).
100. C. A. Makarewich *et al.*, The DWORF micropeptide enhances contractility and prevents heart failure in a mouse model of dilated cardiomyopathy. *Elife* **7**, (2018).
101. P. Mbikou, M. T. Rademaker, C. J. Charles, M. A. Richards, C. J. Pemberton, Cardiovascular effects of DWORF (dwarf open reading frame) peptide in normal and ischaemia/reperfused isolated rat hearts. *Peptides* **124**, 170192 (2020).

102. E. D. Morales *et al.*, Dwarf Open Reading Frame (DWORF) Gene Therapy Ameliorated Duchenne Muscular Dystrophy Cardiomyopathy in Aged mdx Mice. *J Am Heart Assoc* **12**, e027480 (2023).
103. O. N. Raguimova *et al.*, Redistribution of SERCA calcium pump conformers during intracellular calcium signaling. *J Biol Chem* **293**, 10843-10856 (2018).
104. G. W. Gordon, G. Berry, X. H. Liang, B. Levine, B. Herman, Quantitative fluorescence resonance energy transfer measurements using fluorescence microscopy. *Biophys J* **74**, 2702-2713 (1998).
105. T. Zal, N. R. Gascoigne, Photobleaching-corrected FRET efficiency imaging of live cells. *Biophys J* **86**, 3923-3939 (2004).
106. E. M. Kelly, Z. Hou, J. Bossuyt, D. M. Bers, S. L. Robia, Phospholamban oligomerization, quaternary structure, and sarco(endo)plasmic reticulum calcium ATPase binding measured by fluorescence resonance energy transfer in living cells. *J Biol Chem* **283**, 12202-12211 (2008).
107. T. J. Schoenmakers, G. J. Visser, G. Flik, A. P. Theuvenet, CHELATOR: an improved method for computing metal ion concentrations in physiological solutions. *Biotechniques* **12**, 870-874, 876-879 (1992).
108. T. J. Lambert, FPbase: a community-editable fluorescent protein database. *Nat Methods* **16**, 277-278 (2019).
109. B. Sun, B. D. Stewart, A. N. Kucharski, P. M. Kekenos-Huskey, Thermodynamics of Cation Binding to the Sarcoendoplasmic Reticulum Calcium ATPase Pump and Impacts on Enzyme Function. *J Chem Theory Comput* **15**, 2692-2705 (2019).
110. B. D. Stewart *et al.*, Computational modeling of amylin-induced calcium dysregulation in rat ventricular cardiomyocytes. *Cell Calcium* **71**, 65-74 (2018).
111. J. R. Lakowicz, in *Principles of Fluorescence Spectroscopy*. (Springer, 2006), chap. Chapter 4: Time-Domain Lifetime Measurements.
112. J. R. Lakowicz, in *Principles of Fluorescence Spectroscopy*. (Springer, 2006).
113. B. K. Muller, E. Zaychikov, C. Brauchle, D. C. Lamb, Pulsed interleaved excitation. *Biophys J* **89**, 3508-3522 (2005).
114. J. R. Lakowicz, in *Principles of Fluorescence Spectroscopy*. (Springer, 2006), chap. Chapter 24: Fluorescence Correlation Spectroscopy.
115. T. Torres, M. Levitus, Measuring conformational dynamics: a new FCS-FRET approach. *J Phys Chem B* **111**, 7392-7400 (2007).
116. L. M. Espinoza-Fonseca, J. M. Autry, G. L. Ramirez-Salinas, D. D. Thomas, Atomic-level mechanisms for phospholamban regulation of the calcium pump. *Biophys J* **108**, 1697-1708 (2015).

117. D. R. Singh *et al.*, Newly Discovered Micropeptide Regulators of SERCA Form Oligomers but Bind to the Pump as Monomers. *Journal of Molecular Biology* **431**, 4429-4443 (2019).
118. Z. Hou, E. M. Kelly, S. L. Robia, Phosphomimetic Mutations Increase Phospholamban Oligomerization and Alter the Structure of Its Regulatory Complex. *Journal of Biological Chemistry* **283**, 28996-28997-29003 (2008).
119. P. Bidwell, D. J. Blackwell, Z. Hou, A. V. Zima, S. L. Robia, Phospholamban Binds With Differential Affinity to Calcium Pump Conformers. *Journal of Biological Chemistry* **286**, 35044-35050 (2011).
120. E. Mintz, A. M. Mata, V. Forge, M. Passafiume, F. Guillain, The modulation of Ca²⁺ binding to sarcoplasmic reticulum ATPase by ATP analogues is pH-dependent. *J Biol Chem* **270**, 27160-27164 (1995).
121. E. Bovo, J. L. Martin, J. Tyryfter, P. P. de Tombe, A. V. Zima, R-CEPIA1er as a new tool to directly measure sarcoplasmic reticulum [Ca] in ventricular myocytes. *Am J Physiol Heart Circ Physiol* **311**, H268-275 (2016).
122. K. N. Ha *et al.*, Lethal Arg9Cys phospholamban mutation hinders Ca²⁺-ATPase regulation and phosphorylation by protein kinase A. *Proc Natl Acad Sci U S A* **108**, 2735-2740 (2011).
123. Q. Song, S. Pallikkuth, J. Bossuyt, D. M. Bers, S. L. Robia, Phosphomimetic mutations enhance oligomerization of phospholamban and modulate its interaction with the Na/K-ATPase. *J Biol Chem* **286**, 9120-9126 (2011).
124. B. Mueller, C. B. Karim, I. V. Negrashov, H. Kutchai, D. D. Thomas, Direct detection of phospholamban and sarcoplasmic reticulum Ca-ATPase interaction in membranes using fluorescence resonance energy transfer. *Biochemistry* **43**, 8754-8765 (2004).
125. A. Fukuzawa, D. Koch, S. Grover, M. Rees, M. Gautel, When is an obscurin variant pathogenic? The impact of Arg4344Gln and Arg4444Trp variants on protein-protein interactions and protein stability. *Hum Mol Genet*, (2021).
126. A. Li *et al.*, The transmembrane peptide DWORF activates SERCA2a via dual mechanisms. *J Biol Chem*, 100412 (2021).
127. U. V. Reddy *et al.*, A Kink in DWORF Helical Structure Controls the Activation of the Sarco-plasmic Reticulum Ca²⁺-ATPase. *bioRxiv*, 2021.2005.2005.442831 (2021).
128. B. R. Nelson *et al.*, A peptide encoded by a transcript annotated as long noncoding RNA enhances SERCA activity in muscle. *Science* **351**, 271-275 (2016).
129. H. P. Bowditch, Über die Eigenthümlichkeiten der Reizbarkeit, welche die Muskelfasern des Herzens zeigen. *Arbeiten aus der Physiologischen Anstalt zu Leipzig*, (1871).
130. L. A. Mulieri, G. Hasenfuss, B. Leavitt, P. D. Allen, N. R. Alpert, Altered myocardial force-frequency relation in human heart failure. *Circulation* **85**, 1743-1750 (1992).

131. E. M. McNally, L. Mestroni, Dilated Cardiomyopathy: Genetic Determinants and Mechanisms. *Circ Res* **121**, 731-748 (2017).
132. P. Elliott *et al.*, Classification of the cardiomyopathies: a position statement from the European Society Of Cardiology Working Group on Myocardial and Pericardial Diseases. *Eur Heart J* **29**, 270-276 (2008).
133. D. S. Herman *et al.*, Truncations of titin causing dilated cardiomyopathy. *N Engl J Med* **366**, 619-628 (2012).
134. J. P. van Tintelen *et al.*, High yield of LMNA mutations in patients with dilated cardiomyopathy and/or conduction disease referred to cardiogenetics outpatient clinics. *Am Heart J* **154**, 1130-1139 (2007).
135. K. Haghighi *et al.*, A mutation in the human phospholamban gene, deleting arginine 14, results in lethal, hereditary cardiomyopathy. *Proc Natl Acad Sci U S A* **103**, 1388-1393 (2006).
136. J. P. Schmitt *et al.*, Dilated cardiomyopathy and heart failure caused by a mutation in phospholamban. *Science* **299**, 1410-1413 (2003).
137. G. S. Liu *et al.*, A novel human R25C-phospholamban mutation is associated with super-inhibition of calcium cycling and ventricular arrhythmia. *Cardiovasc Res* **107**, 164-174 (2015).
138. P. A. van der Zwaag *et al.*, Phospholamban R14del mutation in patients diagnosed with dilated cardiomyopathy or arrhythmogenic right ventricular cardiomyopathy: evidence supporting the concept of arrhythmogenic cardiomyopathy. *Eur J Heart Fail* **14**, 1199-1207 (2012).
139. M. Vicente *et al.*, Early calcium and cardiac contraction defects in a model of phospholamban R9C mutation in zebrafish. *J Mol Cell Cardiol* **173**, 127-140 (2022).
140. N. Abrol, P. P. de Tombe, S. L. Robia, Acute inotropic and lusitropic effects of cardiomyopathic R9C mutation of phospholamban. *J Biol Chem* **290**, 7130-7140 (2015).
141. S. R. Cleary *et al.*, Inhibitory and stimulatory micropeptides preferentially bind to different conformations of the cardiac calcium pump. *J Biol Chem* **298**, 102060 (2022).
142. D. K. Ceholski, C. A. Trieber, C. F. Holmes, H. S. Young, Lethal, hereditary mutants of phospholamban elude phosphorylation by protein kinase A. *J Biol Chem* **287**, 26596-26605 (2012).
143. D. K. Ceholski, C. A. Trieber, H. S. Young, Hydrophobic imbalance in the cytoplasmic domain of phospholamban is a determinant for lethal dilated cardiomyopathy. *J Biol Chem* **287**, 16521-16529 (2012).
144. E. Hughes, D. A. Middleton, Comparison of the structure and function of phospholamban and the arginine-14 deficient mutant associated with dilated cardiomyopathy. *PLoS One* **9**, e106746 (2014).

145. B. Badone *et al.*, Characterization of the PLN p.Arg14del Mutation in Human Induced Pluripotent Stem Cell-Derived Cardiomyocytes. *Int J Mol Sci* **22**, (2021).
146. C. Maniezzi *et al.*, Early consequences of the phospholamban mutation PLN-R14del+/- in a transgenic mouse model. *bioRxiv*, 2023.2004.2005.535536 (2023).
147. J. Qin *et al.*, Structures of PKA-phospholamban complexes reveal a mechanism of familial dilated cardiomyopathy. *Elife* **11**, (2022).
148. F. Cuello *et al.*, Impairment of the ER/mitochondria compartment in human cardiomyocytes with PLN p.Arg14del mutation. *EMBO Mol Med* **13**, e13074 (2021).
149. A. D. Wegener, H. K. Simmerman, J. P. Lindemann, L. R. Jones, Phospholamban phosphorylation in intact ventricles. Phosphorylation of serine 16 and threonine 17 in response to beta-adrenergic stimulation. *J Biol Chem* **264**, 11468-11474 (1989).
150. V. V. Vostrikov, K. J. Soller, K. N. Ha, T. Gopinath, G. Veglia, Effects of naturally occurring arginine 14 deletion on phospholamban conformational dynamics and membrane interactions. *Biochim Biophys Acta* **1848**, 315-322 (2015).
151. M. Kumar *et al.*, Myofilament Alterations Associated with Human R14del-Phospholamban Cardiomyopathy. *Int J Mol Sci* **24**, (2023).
152. K. Haghghi *et al.*, Impaired Right Ventricular Calcium Cycling Is an Early Risk Factor in R14del-Phospholamban Arrhythmias. *J Pers Med* **11**, (2021).
153. T. R. Eijgenraam *et al.*, The phospholamban p.(Arg14del) pathogenic variant leads to cardiomyopathy with heart failure and is unresponsive to standard heart failure therapy. *Sci Rep* **10**, 9819 (2020).
154. K. Haghghi *et al.*, The human phospholamban Arg14-deletion mutant localizes to plasma membrane and interacts with the Na/K-ATPase. *J Mol Cell Cardiol* **52**, 773-782 (2012).
155. J. P. Schmitt *et al.*, Alterations of phospholamban function can exhibit cardiotoxic effects independent of excessive sarcoplasmic reticulum Ca²⁺-ATPase inhibition. *Circulation* **119**, 436-444 (2009).
156. J. A. Groeneweg *et al.*, Clinical Presentation, Long-Term Follow-Up, and Outcomes of 1001 Arrhythmogenic Right Ventricular Dysplasia/Cardiomyopathy Patients and Family Members. *Circ Cardiovasc Genet* **8**, 437-446 (2015).
157. D. Corrado, M. S. Link, H. Calkins, Arrhythmogenic Right Ventricular Cardiomyopathy. *N Engl J Med* **376**, 61-72 (2017).
158. J. P. van Tintelen *et al.*, Plakophilin-2 mutations are the major determinant of familial arrhythmogenic right ventricular dysplasia/cardiomyopathy. *Circulation* **113**, 1650-1658 (2006).

159. C. J. van Opbergen, M. Delmar, T. A. van Veen, Potential new mechanisms of pro-arrhythmia in arrhythmogenic cardiomyopathy: focus on calcium sensitive pathways. *Neth Heart J* **25**, 157-169 (2017).
160. C. J. M. van Opbergen *et al.*, Exercise Causes Arrhythmogenic Remodeling of Intracellular Calcium Dynamics in Plakophilin-2-Deficient Hearts. *Circulation* **145**, 1480-1496 (2022).
161. G. Inesi, M. Kurzmack, C. Coan, D. E. Lewis, Cooperative calcium binding and ATPase activation in sarcoplasmic reticulum vesicles. *J Biol Chem* **255**, 3025-3031 (1980).
162. A. M. Jensen, T. L. Sorensen, C. Olesen, J. V. Moller, P. Nissen, Modulatory and catalytic modes of ATP binding by the calcium pump. *EMBO J* **25**, 2305-2314 (2006).
163. M. Tada, M. A. Kirchberger, D. I. Repke, A. M. Katz, The stimulation of calcium transport in cardiac sarcoplasmic reticulum by adenosine 3':5'-monophosphate-dependent protein kinase. *J Biol Chem* **249**, 6174-6180 (1974).
164. M. Hoshijima *et al.*, Chronic suppression of heart-failure progression by a pseudophosphorylated mutant of phospholamban via in vivo cardiac rAAV gene delivery. *Nat Med* **8**, 864-871 (2002).
165. C. A. Trieber, M. Afara, H. S. Young, Effects of phospholamban transmembrane mutants on the calcium affinity, maximal activity, and cooperativity of the sarcoplasmic reticulum calcium pump. *Biochemistry* **48**, 9287-9296 (2009).
166. D. M. Clarke, T. W. Loo, G. Inesi, D. H. MacLennan, Location of high affinity Ca²⁺-binding sites within the predicted transmembrane domain of the sarcoplasmic reticulum Ca²⁺-ATPase. *Nature* **339**, 476-478 (1989).
167. G. Inesi, H. Ma, D. Lewis, C. Xu, Ca²⁺ occlusion and gating function of Glu309 in the ADP-fluoroaluminate analog of the Ca²⁺-ATPase phosphoenzyme intermediate. *J Biol Chem* **279**, 31629-31637 (2004).
168. S. R. Cleary *et al.*, Inhibitory and Stimulatory Micropeptides Preferentially Bind to Different Conformations of the Cardiac Calcium Pump. *J Biol Chem*, 102060 (2022).
169. L. M. Espinoza-Fonseca, J. M. Autry, D. D. Thomas, Sarcolipin and phospholamban inhibit the calcium pump by populating a similar metal ion-free intermediate state. *Biochem Biophys Res Commun* **463**, 37-41 (2015).
170. B. L. Akin, T. D. Hurley, Z. Chen, L. R. Jones, The structural basis for phospholamban inhibition of the calcium pump in sarcoplasmic reticulum. *J Biol Chem* **288**, 30181-30191 (2013).
171. K. E. Coll, R. G. Johnson, Jr., E. McKenna, Relationship between phospholamban and nucleotide activation of cardiac sarcoplasmic reticulum Ca²⁺ adenosinetriphosphatase. *Biochemistry* **38**, 2444-2451 (1999).
172. J. D. Clausen *et al.*, SERCA mutant E309Q binds two Ca(2+) ions but adopts a catalytically incompetent conformation. *EMBO J* **32**, 3231-3243 (2013).

173. N. Tsunekawa, H. Ogawa, J. Tsueda, T. Akiba, C. Toyoshima, Mechanism of the E2 to E1 transition in Ca(2+) pump revealed by crystal structures of gating residue mutants. *Proc Natl Acad Sci U S A* **115**, 12722-12727 (2018).
174. Z. Chen, D. L. Stokes, L. R. Jones, Role of leucine 31 of phospholamban in structural and functional interactions with the Ca²⁺ pump of cardiac sarcoplasmic reticulum. *J Biol Chem* **280**, 10530-10539 (2005).
175. S. Currie, G. L. Smith, Enhanced phosphorylation of phospholamban and downregulation of sarco/endoplasmic reticulum Ca²⁺ ATPase type 2 (SERCA 2) in cardiac sarcoplasmic reticulum from rabbits with heart failure. *Cardiovasc Res* **41**, 135-146 (1999).
176. C. Hayward, N. R. Banner, A. Morley-Smith, A. R. Lyon, S. E. Harding, The Current and Future Landscape of SERCA Gene Therapy for Heart Failure: A Clinical Perspective. *Hum Gene Ther* **26**, 293-304 (2015).
177. F. del Monte *et al.*, Restoration of contractile function in isolated cardiomyocytes from failing human hearts by gene transfer of SERCA2a. *Circulation* **100**, 2308-2311 (1999).
178. Y. F. Mi *et al.*, Improvement in cardiac function after sarcoplasmic reticulum Ca²⁺-ATPase gene transfer in a beagle heart failure model. *Chin Med J (Engl)* **122**, 1423-1428 (2009).
179. R. Aguayo-Ortiz *et al.*, A multiscale approach for bridging the gap between potency, efficacy, and safety of small molecules directed at membrane proteins. *Sci Rep* **11**, 16580 (2021).
180. H. K. Hammond *et al.*, Intracoronary Gene Transfer of Adenylyl Cyclase 6 in Patients With Heart Failure: A Randomized Clinical Trial. *JAMA Cardiol* **1**, 163-171 (2016).
181. S. Kang *et al.*, Small Molecular Allosteric Activator of the Sarco/Endoplasmic Reticulum Ca²⁺-ATPase (SERCA) Attenuates Diabetes and Metabolic Disorders. *J Biol Chem* **291**, 5185-5198 (2016).
182. M. Arici *et al.*, Istaroxime Metabolite PST3093 Selectively Stimulates SERCA2a and Reverses Disease-Induced Changes in Cardiac Function. *J Pharmacol Exp Ther* **384**, 231-244 (2023).
183. M. Rocchetti *et al.*, Modulation of sarcoplasmic reticulum function by PST2744 [istaroxime; (E,Z)-3-((2-aminoethoxy)imino) androstane-6,17-dione hydrochloride]] in a pressure-overload heart failure model. *J Pharmacol Exp Ther* **326**, 957-965 (2008).
184. H. Ravishankar *et al.*, Tracking Ca(2+) ATPase intermediates in real time by x-ray solution scattering. *Sci Adv* **6**, eaaz0981 (2020).
185. V. Dubey, B. Bozorg, D. Wustner, H. Khandelua, Cholesterol binding to the sterol-sensing region of Niemann Pick C1 protein confines dynamics of its N-terminal domain. *PLoS Comput Biol* **16**, e1007554 (2020).

186. D. R. Stroik *et al.*, Targeting protein-protein interactions for therapeutic discovery via FRET-based high-throughput screening in living cells. *Sci Rep* **8**, 12560 (2018).
187. I. Karakikes *et al.*, Correction of human phospholamban R14del mutation associated with cardiomyopathy using targeted nucleases and combination therapy. *Nat Commun* **6**, 6955 (2015).
188. E. McKenna *et al.*, Dissociation of phospholamban regulation of cardiac sarcoplasmic reticulum Ca²⁺-ATPase by quercetin. *J Biol Chem* **271**, 24517-24525 (1996).
189. F. Funk *et al.*, Phospholamban pentamerization increases sensitivity and dynamic range of cardiac relaxation. *Cardiovasc Res*, (2023).
190. E. Bertero, C. Maack, Calcium Signaling and Reactive Oxygen Species in Mitochondria. *Circ Res* **122**, 1460-1478 (2018).
191. D. Yucel *et al.*, Increased oxidative stress in dilated cardiomyopathic heart failure. *Clin Chem* **44**, 148-154 (1998).
192. J. P. Andersen, Functional consequences of alterations to amino acids at the M5S5 boundary of the Ca(2+)-ATPase of sarcoplasmic reticulum. Mutation Tyr763-->Gly uncouples ATP hydrolysis from Ca²⁺ transport. *J Biol Chem* **270**, 908-914 (1995).

VITA

The author, Sean Cleary, was born in Palos Heights, IL to Kevin and Diane Cleary on September 10, 1992. He attended Lewis University in Romeoville, IL, where he earned a Bachelor of Science in Biology in 2015. After graduation, Sean worked for 3 years in industry, primarily in the Micro and Molecular Immunology department of a contract research organization at the Illinois Institute of Technology (IIT), IIT Research Institute. Sean matriculated into the Integrated Program in Biomedical Science at Loyola University Chicago in 2018, where he conducted his graduate studies in the Cell and Molecular Physiology program under the mentorship of Dr. Seth Robia.

Sean's graduate research focuses on understanding the regulatory mechanisms that control the sarcoplasmic reticulum Ca^{2+} transporter, SERCA, in cardiac muscle. Specifically, Sean's work aims to understand how the regulation of SERCA dynamically adjusts Ca^{2+} handling to match the ever-changing physiological demands of the heart. His work was supported in part by a predoctoral National Research Service Award (NRSA) from the National Heart, Lung, and Blood Institute (NHLBI) at the National Institutes of Health (NIH). After completing his graduate work, Sean will continue to study ion transport in cells as a post-doctoral research fellow in Dr. Miguel Holmgren's lab at the National Institute of Neurological Disorders and Stroke (NINDS) at the NIH in Bethesda, MD.

